Systematic Improvement of Quantification and Formulation of Synthetic Protein Nanoparticles for Gene Delivery

by

Laura E. Saunders

A dissertation submitted in partial fulfillment
of the requirements for the degree of
Doctor of Philosophy
(Macromolecular Science and Engineering)
in the University of Michigan
2022

Doctoral Committee:

Professor Joerg Lahann, Chair
Professor Sharon Glotzer
Dr. Jodi Kennedy, Intergalactic Therapeutics
Professor David Kohn

Laura E. Saunders

laurasau@umich.edu

ORCID iD: 0000-0002-3612-4967

Dedication

This thesis is dedicated to my family and friends, without whom I would never have gotten through my Ph.D. study. First, I would like to thank my parents for their constant support and for acting as my own personal cheering section, no matter the circumstances. My mom and dad have at times supported, motivated, encouraged, and comforted me during my graduate school journey, and I cannot thank them enough. I would like to thank my Aunt Kathy and Uncle Mike for making Ann Arbor feel like home and for their constant and enthusiastic encouragement. I would also like to thank my sisters, Madelaine and Catherine for much-needed distractions and motivation especially in the past few months.

I have also been extremely fortunate with the friends that I have made in my life. I would like to thank Jen (Ketcham) Hagen who has been like a sister to me for over 15 years. Throughout my adult life she has been an unrelenting source of optimism and a close confidant. I am grateful for the friendship I share with Dan Matera, who is constantly pushing my boundaries from camping to cooking and has been a source support for some of the most trying times in my life. I am also grateful for the friends I made in graduate school: Ava, Sang, Kelly, Nick, Ravi, Scott, Tim, Erin, and Pieter have all been instrumental to my personal growth and happiness during the past five years and each is special to me in many ways.

Finally, I want to thank Chris Tossas for his help keeping everything in perspective, and for making even the most mundane or painful experiences bearable. Chris gave me relentless support, optimism, and motivation and spent hours helping me edit this thesis, supporting me in this as he does all my goals. He was also often instrumental in keeping me highly caffeinated and well-fed, as well as giving me something to look forward to coming home to each day. I look forward to many more shared laughs, adventures, and Christmas trees.

Acknowledgements

The work presented in this thesis and conducted during my graduate study would not have been possible without the mentorship and support of Professor Joerg Lahann. I would like to extend my sincerest thank you to him for adopting me into his research group and for his support along the way to this milestone. At each step, he challenged my abilities, from writing to research to presentation. By overcoming ever higher standards, I improved more than I thought was possible. My Ph.D. has been a period of tremendous learning, and I have often joked that I feel I learned and grew more in my thought process and curiosity after 6 months in Professor Lahann's lab than in the previous 3 years combined. I still think this is true, and I would like to thank him for the opportunity as well as the example that he set for excellence in scholarship, scientific rigor, and integrity. I am honored to have learned from him and proud to be graduating from his research group.

I would also like to thank my committee members, Professor Sharon Glotzer, Professor David Kohn, and Dr. Jodi Kennedy for their guidance and support. The insightful conversations that I have shared with each of them have been formative to the content of this thesis. I greatly appreciate the support and guidance of Professor Glotzer over the past two years and I am honored to have someone with her expertise, sharp insight, and humanity to help guide my academic pursuits. I appreciate the many conversations Professor Kohn and I have shared from the hallways of the Dental Building to the class he taught in tissue engineering and the questions he has asked for every grant proposal and data meeting update that I sent him. It has been a pleasure to work with Jodi and share her endless curiosity and many great discussions outside of research and work. Truly, this thesis would not be as strong, or myself as competent of a researcher without the significant contributions made by my committee members.

Also of great importance to my graduate study was Dr. Jeffery Raymond, who acted as a mentor and advisor to me for matters both academic and professional. The work presented in this thesis would not be the same, and in some cases would not have been possible without his insight and guidance. His mentorship has helped me grow faster and achieve more than I knew I could.

I would not be the person and researcher that I am today without the benefit of working with the tremendous coworkers I have had over the past five years. I would like to extend a sincere thank you to the lab mates who have been part of a community of support and encouragement. Thank you to Dr. Kunal Rambhia, for acting as a mentor and friend during our time working together. I greatly appreciate your continued advice and friendship. I would like to thank Dr. Jason Gregory and Dr. Nahal Habibi for their mentorship and friendship. Their companionship, scientific advice and help in all aspects of the lab, from equipment troubles to research proposals has always been appreciated. My work would never have gone as smoothly as it did if not for their advice and input. A very special thank you to Ava Mauser for her constant companionship and support in the lab as well as the many profound scientific and personal discussions that we had in the hours of sharing bench space for the past two or more years.

I would also like to thank each lab member that I have had the pleasure of working with and learning from during my graduate study. Even those who did not have a direct impact on the work presented here were instrumental to myself or the functioning of the lab as a whole and for that I am thankful. I'd like to especially thank Dylan Neale for his kindness and compassion and for establishing a weekly check-in during which time the two of us could pick each other's brains, vent, or just work. Dylan made dissertating less lonely and much more enjoyable. I would like to thank Dr. Kemao Xiu, Dr. Ruonan Dong, Dr. Luan Wen, and all my previous lab mates for helping me start my graduate school career. I would also like to thank my current lab mates, including Anthony Berardi, Albert Chang, Chris Kim, John Kim, Arit Patra, Fjorela Xhyliu, Yao Yao, and Xiaoyang Zhong. I am also grateful for the opportunity to mentor the undergraduate students that I worked with, especially Nathan Li and Eva Wang.

Finally, I would like to thank all the staff members in the Biointerfaces Institute, Macromolecular Science and Engineering, and Chemical Engineering for making a lot of this work possible and keeping everything running smoothly. In particular, I would like to thank Lisa Moran, Dr. Nadine Wong, Laura Charlick, Mary Beth Westin, and Dr. Sarah Spanninga for all their help and guidance over the years.

Table of Contents

List of Tables

List of Equations

List of Figures

List of Appendices

Abstract

Gene therapy is a promising field for the generation of new and more effective therapies, but its application is stymied by the lack of safe and efficient delivery vehicles. Furthermore, gene delivery system optimization is hindered by inadequate methods for payload quantification within nanoparticles.

The work presented in this thesis establishes methods to formulate and quantify plasmid DNA (pDNA) loading in protein carriers that drive maximal gene expression towards two aims: **Aim 1:** Engineering and characterization of plasmid DNA payloads in synthetic protein nanoparticles and **Aim 2:** Structure function relationships related to protein nanoparticle composition and reporter gene expression. The pDNA loading of synthetic proteins nanoparticles (SPNPs) has been fully characterized, and a method for probing the effect of composition on biological outputs has been established. With clinical translation as the ultimate goal, the fundamental discoveries presented herein enable the further development and *in vivo* application of SPNP vectors.

Here, the characterization and formulation of SPNPs are studied and optimized for their effect on reporter gene expression in a model cell line. The efficiency of SPNP production is important to systems with precious or difficult to manufacture payloads. This thesis also examines processing methods for SPNPs, and the mass loss and repeatability of the current centrifugal filtration method is compared to a new syringe filtration method.

In Chapter 2, we developed a strategy for fluorescent plasmid backbone labeling (PBL) that enables the characterization of SPNPs loaded with pDNA with lower measurement bias than the conventional methods tested. This allowed us to determine the loading percentage as well as model the maximum loading of pDNA in SPNPs. We next combined pDNA and particle size quantifications to determine the distribution of pDNA within a SPNP population; this allowed us to examine SPNP loading with a granularity not widely reported in literature. An in-depth protocol for the PBL strategy is presented in Chapter 3 to assist future researchers in adapting the PBL strategy for various systems and nucleotides.

In Chapter 4, the structure function relationship between SPNP composition and reporter gene expression was investigated by varying three key parameters: polyethylenimine (PEI) amount, SV40 content, and pDNA loading percentage. A rational design strategy was developed to interrogate the effect of changing PEI, SV40 and pDNA on reporter gene expression (GFP %). We found that PEI content positively correlated with GFP % (correlation coefficient = 0.91), while no other SPNP component (SV40) or biological output (viability, uptake) did.

The work presented here establishes strategies for quantifying and formulating SPNPs *in vitro* for eventual application in organismal studies and human health. This thesis presents a platform for quantification and design of gene delivery vectors that can be extended to various nucleotides, genes, and target applications.

Chapter 1

Introduction

1.1 Background on Gene Therapy

Gene therapy is the modification of genetic material within a cell for a therapeutic effect and has the ability to provide treatment or a cure for diseases that have few or no treatment options.[1] The promise of such therapy has garnered immense interest and support in the past decade, with huge investments made in the private and academic sectors.[2–4] Countless companies and startups aimed at delivering on this promise have been established.[5–7] To have the intended effect, gene delivery aims to transport genetic payloads to target cells and induce the desired change, where methods to deliver these payloads range from physical to biologic delivery.[8] Physical delivery includes methods such as electroporation and microinjection, however, these methods must be utilized *ex vivo*, then implanted back into the host, limiting their efficacy in treating disease states within the human body.[9,10] Conversely, biologic delivery of gene therapies aims to deliver payloads into host cells and has therefore received the majority of research and commercialization interest and will be the focus of this thesis.[3]

1.2 Gene Delivery Methods

A key engineering challenge facing the field of gene delivery is the development of safe and effective delivery vehicles.[11] Biologic delivery of genetic material can be broadly classified into carriers based on viral and non-viral engineered vehicles.[12,13] Of the two, virus-based gene therapy is more effective, but it can cause safety and immunogenicity issues that limit its application and scope.[14,15] Host immune response can result in lowered efficacy and difficulty re-dosing viral components due to an effective immune response to previously perceived infection with the viral vehicle.[16–19] Indeed, approximately 70% of gene therapy clinical trials have utilized viral vectors but have had limited success given the numerous attempts at translation.[11] The safety issues associated with viral vehicles have been severe enough to halt clinical trials due to the virus-based vehicles resulting in the emergence of cancer and death.[20] To avoid concerns about safety and immunogenicity, the field of gene therapy has pivoted to non-viral gene delivery.

Non-viral gene delivery vehicles have the potential to address several of the limitations facing viral vehicles and offer benefits unique to engineered systems. Importantly, non-viral gene delivery vehicles do not suffer from the same short-term and long-term safety concerns as their viral counterparts. They also offer benefits compared to their viral counterparts, including higher loading capacities, ease of synthesis, and the ability to re-dose.[21,22] Whereas viruses have the evolutionary benefit of highly efficient genetic transfer to target cells, engineered delivery systems still suffer from much lower therapeutic efficacies.[23] To meet this challenge, the fields of polymer science, nanotechnology, and polymer chemistry have made great strides towards development of new materials, but work remains to be done.[24]

Non-viral gene delivery vehicles can further be classified into four broad categories, inorganic, lipid, polymeric, and protein nanoparticles (NPs).[25,26] While inorganic, lipid, and polymeric NPs are commonly used in the field, the work discussed in this thesis has been carried out using synthetic protein nanoparticles (SPNPs), a unique class of protein NPs and discussion will therefore revolve around SPNPs and their properties.[27–32] SPNPs exhibit superior drug and gene delivery for siRNA while maintaining high biocompatibility and low toxicity in organismal studies, but their use has not been extended to pDNA delivery, the focus of this thesis.[32–34]

1.3 Synthetic Protein Nanoparticles as Gene Delivery Vehicles

SPNPs have multiple beneficial properties for drug and gene delivery to mammalian cells as they combine benefits from their constituent protein content and advantageous properties of NPs[26]. SPNPs are prepared using electrohydrodynamic (EHD) jetting, which offers a lot of modularity in NP preparation (**Figure 1-1**). [33–35]

The experimental setup for EHD jetting is comprised of a syringe loaded with protein solution components pumped at a constant rate from a syringe. A high voltage (10-12kV) is applied to the syringe tip, and the solution is atomized and pulled towards a grounded collection plate. As the solution travels to the collection surface SPNPs are formed and can be visualized using scanning electron microscopy (**Figure 1-1**).

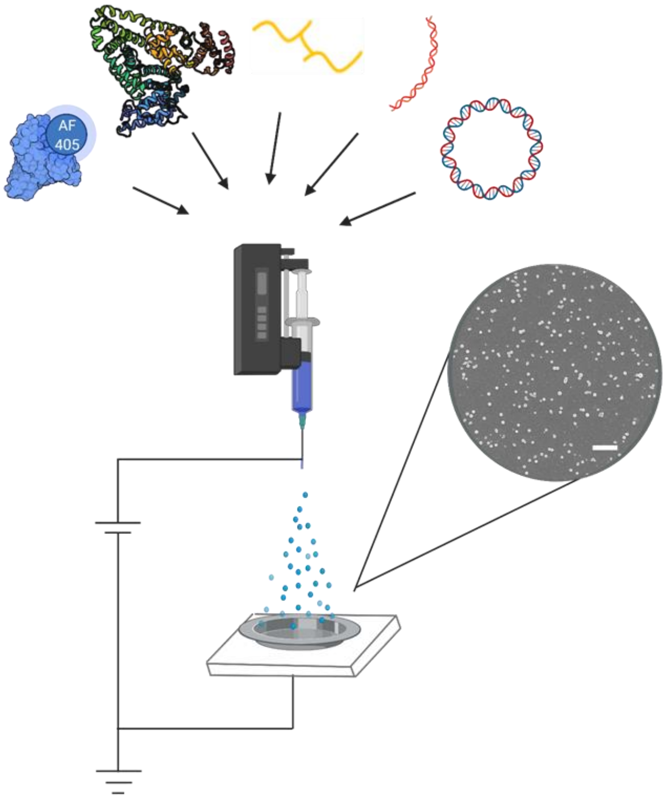

Figure 1-1 Electrohydrodynamic (EHD) jetting setup for synthetic protein nanoparticle preparation. Inset: scanning electron microscopy image of SPNPs, scale bar 2 µm. Schematic created with Biorender.com.

EHD combines the modularity associated with the jetting parameters with the ability to swap proteins and macromer units for a plug and play preparation of SPNPs, enabling many different applications. SPNPs prepared via EHD jetting have numerous beneficial properties including high uniformity (polydispersity indices less than 0.2), high circularity (greater than 0.85), favorable sizes for cellular uptake, and low cytotoxicity in target cells.

The protein used to form the SPNPs reported here is Human Serum Albumin (HSA) an endogenous protein that is derived from the serum portion of human blood.[36] HSA exhibits high stability and solubility in aqueous solutions as well as good biocompatibility in mammalian cells and biodegradability in animal models. For these reasons, HSA and other albumins are widely used in many gene delivery applications in combination with cationic moieties such as polyethyleneimine (PEI) that are chosen to exploit the biology of the pDNA delivery route and drive maximal gene expression.[32,37–40]

1.4 Intracellular Barriers to pDNA Delivery

Regardless of the method, all gene delivery vehicles have the common goal of delivering their genetic payload efficiently and safely to target cells, requiring careful design of their formulation. Since efficient delivery of DNA requires an understanding of its intracellular route and the barriers that it faces, the delivery vehicle must be designed to overcome these obstacles. While gene delivery faces extracellular hurdles that need to be cleared, and should not be ignored, this work focuses primarily on design of SPNPs for overcoming intracellular barriers. Therefore, this topic will be discussed in detail here to provide context on the design choices made in the discussed work to tackle intracellular barriers affecting gene delivery.

Here, the path of pDNA as it journeys through the transfected cell from entry to expression is detailed (**Figure 1-2**). First, the NP carrying the pDNA payload must be taken up into the cell, typically through endocytosis. Second, the NP, which is now trapped in the endosome, must escape to be released intracellularly. Following this, pDNA then must gain entry to the nucleus where it can induce genetic changes to express a reporter gene or a have a therapeutic effect. Finally, biological outputs of the transfected cells are considered, from toxicity associated with the NP to efficacy of the pDNA expression. All these steps are described in detail with materials considerations and strategies for addressing stumbling blocks explained. Finally, considerations for the biological outputs and overall NP design strategy are discussed and the objectives of this work are presented.

1.4.1 Cellular Entry of Nanoparticles

The cell membrane presents the first biological barrier that decreases the efficacy of available therapeutics (**Figure 1-2**). Cellular entry is required to achieve the desired effects. There are several design strategies that are used to increase cellular uptake through a variety of pathways.[28] Firstly, the architecture of the NP is important, with branched, comb, or brush-like architecture increasing uptake when compared to linear counterparts.[41,42] Secondly, the size of NPs has a huge effect on cellular uptake, with different entry routes having different size restrictions.[43] In general, for DNA delivery systems, the highest uptake is seen for NPs with diameters of less than 200 nm.[44] Charge is also an important consideration, with surface charge affecting both the viability of target cells, (e.g., highly positive NPs are toxic), and the uptake mechanism (cationic and anionic NPs can enter through different mechanisms). Finally, targeting ligands such as RGD, folate, and GalNAc are often used to increase uptake in a certain organ system.[45–47] All these considerations need to be accounted for when designing for a cellular uptake mechanism that is desirable for a specific NP system.

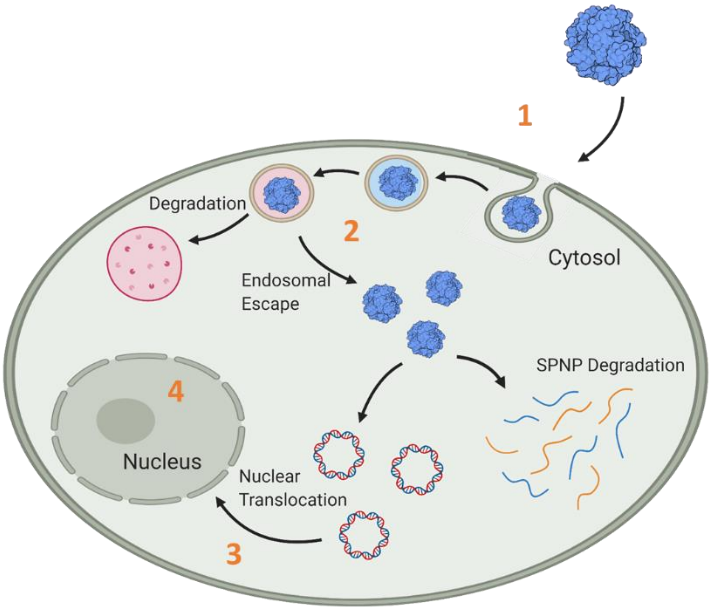

Figure 1-2. Schematic of the DNA delivery route and intracellular barriers facing effective transfection. First, the SPNP must successfully (1) enter the cell then (2) escape the endosome to be released intracellularly and then gain (3) entry to the nucleus. Following transfection, the (4) biological outputs can be examined. Schematic created with Biorender.com.

1.4.2 Endosomal Escape Mechanisms

Endocytosis is by far the most common route for cellular uptake of NPs and can be split into two categories: phagocytosis and pinocytosis. Phagocytosis is most effective in a nanoparticle size range greater than 400 nm and phagocytes, such as macrophages, are responsible for host defense and clearing dead cells.[44,48] Pinocytosis can be further split into four categories: clathrin-mediated endocytosis (CME), caveolae-dependent endocytosis (CDE), clathrin/ caveolae independent endocytosis, and macropinocytosis.[49] CME governs uptake for positively charged NPs, while CDE is responsible for cellular entry of negatively charged NPs.[50,51] CDE is also responsible for uptake of albumin via a receptor in endothelial cells. It has been shown that Abraxane®, an FDA approved NP chemotherapy agent consisting of albumin bound paclitaxel is endocytosed through

CDE.[52] Based on these observations, it is likely that the SPNPs presented here are endocytosed through the CDE mechanism.

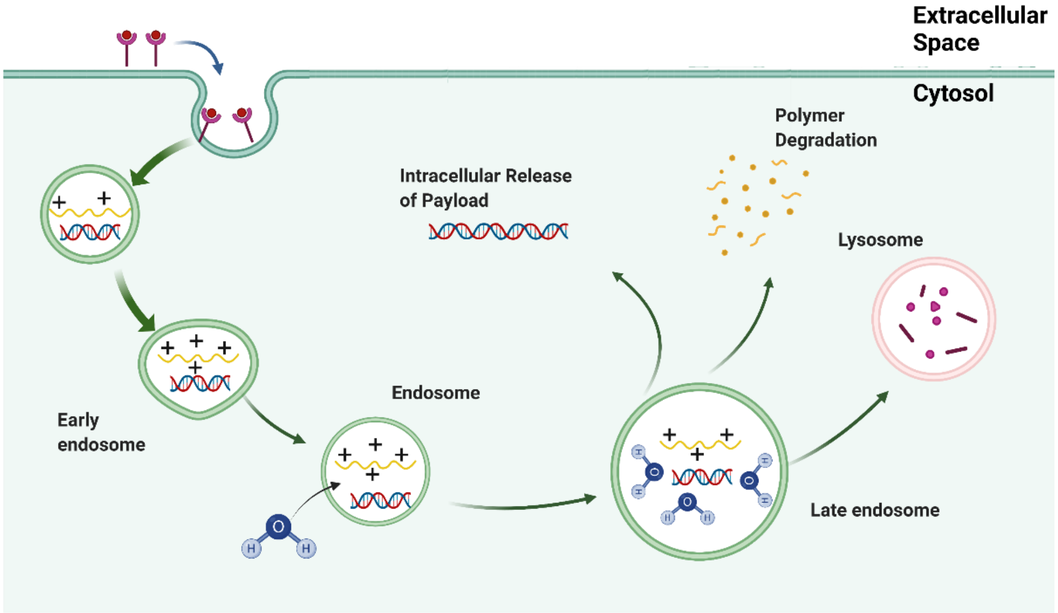

Figure 1-3. Schematic representation of endosomal escape via the proton sponge effect. The SPNPs described here utilize addition of polyethylenimine (PEI) to osmotically swell the endosome, causing it to rupture and release the DNA payload intracellularly. Schematic created with Biorender.com.

Once a NP has been endocytosed, it will be encased in the endosome, which will traffic to the lysosome for degradation unless the NP undergoes endosomal escape (**Figure 1-3**).[53] There are several methods employed to enhance endosomal escape of biologic-delivering NPs.[54] The first, and arguably most common, is inclusion of a cationic (e.g., PEI, imidazole-containing polymers) or zwitterionic (e.g., DOPE) moiety.[55,56] Cationic or zwitterionic polymers with high buffering capacities osmotically swell the endosome until it bursts through a mechanism termed the proton sponge effect.[57–62] Polymeric and synthetic protein nanoparticles (SPNPs) achieve endosomal escape through the so-called proton sponge effect mediated by inclusion of PEI. Other strategies for endosomal escape include addition of fusogenic peptides (e.g., KALA, GALA, etc.)

and chemical agents (e.g., chloroquine, ammonium chloride, etc.).[63] In this work, PEI was incorporated into the SPNPs, causing endosomal swelling and rupture to induce intracellular release of the pDNA payload (**Figure 1-3**).

1.4.3 Strategies for Enhancing Nuclear Entry

Following endosomal escape, a pDNA must be transported from the cytosol to the nucleus, to achieve the desired therapeutic effect (**Figure 1-2**).[64] While there are a few routes to nuclear entry that both viruses and engineered NP systems utilize, a nuclear localization signal (NLS) is typically exploited. An NLS is a protein or peptide derived from a virus such as HIV or Simian Virus that has evolved to trigger nuclear pore complexes to actively transport NLS-containing molecules across the nuclear membrane.[65–67] NLS can be incorporated into NPs or pDNA in a few different ways. One approach is to engineer pDNA to express a NLS encoding region on their backbone, a commonly used strategy in commercially available pDNA vectors. Another approach is to incorporate a cationic NLS protein or peptide into the gene delivery system via electrostatic combination with the anionic pDNA or through chemical conjugation to the backbone of the pDNA.[68] Both of these approaches are effective at increasing gene expression *in vitro* and *in vivo*, exhibiting higher reporter and functional gene expression.[69]

For nuclear entry, delivery systems often rely on mass action of pDNA and mitotic disassembly of the nuclear envelope during cell division to enter the nucleus which does not require the use of an NLS.[64] During cell division, the nuclear envelope is broken down and pDNA can enter through holes in the membrane. To do so, a large number of pDNA must be present, and the cell in question must be a dividing cell.[70] Therefore, NLS are necessary to get meaningful nuclear import in quiescent cells. It is for these reasons that transfection of cells with pDNA is often done in cells that are not confluent and are actively dividing.[64,71]

1.4.4 Biological Outputs and Other Considerations

After the target cell has been transfected, there are still several factors to consider that will impact whether a NP delivery system is deemed successful or not. In general, biological outputs are the most important metrics to measure for success of a NP, although attention is paid to efforts surrounding scalability for commercial applications.[11] The efficacy of the gene delivery vehicle is a balancing act between the cytotoxicity, uptake, and gene expression induced by the NP.[72] That is, a NP that is too toxic to cells will never succeed even if its efficiency is near-perfect because it will have killed the target cells. Uptake is another consideration that must be weighed against toxicity and gene expression to determine the best NP for each application.

It has been established that gene expression is often dependent on the dose of pDNA delivered, with different NP delivery systems reporting different optimal doses.[73,74] However, higher doses of pDNA could result in higher toxicities due to introduction of more exogenous material to the target cells. Therefore, design of the gene delivery system is often a balancing act between viability, uptake, and gene expression where all aspects need to be considered and optimized for. The final NP formulation is generally determined by the desired application and regulatory agencies that may be involved.[75]

1.4.5 Characterization of DNA Delivery System Payloads

While there has been success developing a range of different NPs for gene delivery purposes, the consideration of in-depth payload quantification during NP design remains under-investigated in the field. It is important to fully characterize a gene delivery system so that the impact of engineering decisions can be understood during development of a system. Additionally, regulatory boards require accurate assessment of total payload delivered and thus a complete understanding of the NP system is necessary.[76] However, due to the chemical and structural complexity of engineered gene delivery systems, quantification of DNA loading and distribution is not easy or straightforward.[77]

Indeed, conventional methods for measuring DNA content in solution fails when applied to a NP system and indirect measurement methods are often used.[78–81] Without confidence in the measurement of DNA loaded into a NP, it is impossible to know the amount delivered during an experiment, and therefore the therapeutic dose cannot be understood. Another complicating factor is the potential uneven distribution of payload across various sizes within a NP population. Different sizes of NP will incorporate different amounts of DNA, as the internal volume of a spherical NP varies with its diameter. Without knowledge of loading, the amount of payload that resides in biologically relevant fractions of the particle population cannot be known. Therefore, it is necessary to establish a strategy for quantifying DNA loading within a gene delivery system to gain an understanding of the NP and to establish a therapeutic dose as required by regulatory agencies for application to begin clinical trials.[76]

1.4.6 Aims of This Work

Rational design of a gene delivery system requires careful consideration of each step and changes to the NP formulation that can best exploit the biology of the intended target to drive maximal gene expression. In this thesis, the methodology for characterization of DNA payloads in SPNPs are presented. These methods provide a framework that can be further built upon by future researchers. Later chapters presented here focus on an examination of structure function relationships related to SPNP composition and reporter gene expression. The composition of the reported SPNPs relies on formulation, which utilizes carefully chosen materials to exploit the biology of the DNA delivery route and overcome previously discussed barriers. The following chapters will explore the preparation of fully characterized SPNPs for gene delivery and the rational design of a SPNP formulation that drives maximal gene expression towards two aims:

Aim 1: Engineering and characterization of plasmid DNA payloads in synthetic protein nanoparticles. *Having established that SPNPs can be loaded with plasmid DNA, the content of these SPNPs is quantified and a method is established for characterization of pDNA within a fully crosslinked SPNP system.*

Aim 2: Structure function relationships related to protein nanoparticle composition and reporter gene expression. *The formulation of prepared pDNA loaded SPNPs is varied within a 3D design space and biological outputs are examined to elucidate design rules towards improvement of reporter gene expression.*

Chapter 2

Synthetic Protein Nanoparticles for Delivery of Precisely Determined Doses of Plasmid DNA

The material in this chapter has been adapted with minor modifications from the following article:

1. L. Saunders, A. Chang, A. Mauser, J. Gregory, J. Raymond, J. Lahann. "Synthetic Protein Nanoparticles for Delivery of Precisely Determined Doses of Plasmid DNA", *in preparation*.

2.1 Introduction to DNA Delivery Systems

Non-viral gene therapies using nucleotides (e.g., mRNA, DNA, small non-coding RNAs) hold promise for a broad array of applications, as evidenced by the widespread adoption of mRNA vaccines for the fight against COVID-19.[2,82–84] Multiple gene therapy platforms have emerged as strong candidates for next generation therapies, and the variety and scope of these therapies is rapidly expanding.[85] Gene therapy is extremely versatile and allows the targeting of disease states that have traditionally been impossible to treat.[17] While multiple gene therapies exist in the commercial space, the cost effectiveness of exploration in these regimes means that it is readily available to both research groups and biotechnology startups. In effect, recent advances in gene therapies result in a more level R&D playing field, one that is not completely dominated by pharmaceutical company heavyweights.

While these therapies hold tremendous promise, they still require a well-characterized delivery system to protect the cargo from the extracellular and intracellular environments. This has historically been a stumbling block to the realization so many nucleotide-based applications.[83] Aside from the problems intrinsic to having an effective and well understood delivery system, researchers also seek a high confidence in knowing the state and amount of payload delivered.

Recent developments have shown that mRNA-based technologies can be rapidly scaled where there is sufficient pressure and motivation without the use of viral vectors.[86–88] This has not been displayed for pDNA-based therapies, with established DNA delivery systems typically using viral vectors (for examples see ClinicalTrials.gov).[82] Viral vectors, of which Adeno-associated viruses (AAVs) are the most widely used are highly effective at infiltrating cellular nuclei, but issues with safety and scale-up have challenged translation of these systems.[16,18–20,89–93] As such, there is still much interest in refining non-viral vector pDNA delivery platforms that are well understood in terms of payload incorporation, retention, and loading prior to delivery. Furthermore, understanding nucleotide incorporation efficiency, intra-particle nucleotide distribution, and inter-particle homogeneity will assist in the optimization of emergent technologies.

Given the desire for the expansion of non-viral vector platforms, the enormous interest in DNA delivery platforms has shifted toward the use of synthetic engineered carriers.[25,92,94] In general, engineered gene delivery vehicles enjoy higher loading capacity than their viral counterparts.[6] Standard strategies for this include lipid-, polymeric-, and protein-based technologies.[23,25,94] While promising, these systems often fail to report quantification of DNA loading or dosage (typically reported as a mass percent as formulated or through indirect measurements. Common methods of dosing quantification include measuring changes in the charge of the nanoparticle through a gel retardation assay or measurement of the zeta potential.[78,95,96] Other methods include measurement of loaded DNA after degradation of the delivery system or via comparison of DNA concentration in the nucleotide solution before and after loading.[80,81,97,98] With the goal of developing repeatable, clinically translatable DNA delivery technology, proper characterization of these systems is required. Indeed, regulatory agencies require precise reporting of treatment dosing for drug- and gene- delivery systems.

2.2 Limitations of Measurement Methods for DNA Loading in Nanoparticles

Conventional DNA measurement methods are limited in their application and scope. While there are several methods available for quantifying DNA in isolation or in solution, the ability to determine DNA content in a protein-rich solution or within nanoparticles remains underdeveloped. Here, a review of limitations for common DNA measurement techniques is included.

2.2.1 Limitations of UV-Vis Spectroscopy for DNA Measurement in The Presence of Human Serum Albumin

Owing to the chemical and structural complexity of engineered delivery platforms, measurement of nucleotide loading, and distribution is not facile.[99] Indeed, while nucleotides in solution can be accurately measured by established methods, their accuracy is limited when assessing DNA within solid carriers, or when DNA complexed to polymeric or oligomeric materials. One example is cuvette-based or cuvette-free UV-Visible Spectroscopy (e.g., Nanodrop) which has difficulty parsing proteins from and nucleotides. This is due to a large degree of spectral overlap owing to nucleic acid purine and pyrimidine subunits being confounded with tyrosine and tryptophan subunits in proteins.[99] Furthermore, this region of the UV spectrum is heavily influenced by scattering signal, which is substance, particle size, solvent, and concentration specific. Due to these challenges, few papers have relied on UV-Vis spectroscopic measurements to quantify the DNA loading in nanoparticle systems, but those reported values exhibit high DNA amounts. Spectroscopic measurements are limited in sensitivity and as such, large amounts of DNA are needed for measurement, compared with assays which are an order of magnitude more sensitive.[100] For example, a study reporting on the loading efficiency of PLGA nanoparticles used UV-Vis for DNA measurement and reported on an average per-particle loading with a maximum of 4 µg.[98] Taken together, these factors indicate that direct UV-Visible measurements are of limited use for the measurement of nanoparticle-containing systems.

2.2.2 Limitations of Fluorescence Binding Assays for DNA Measurement in The Presence of Polyethyleneimine

Beyond spectroscopic techniques, fluorescence- and colorimetric-based assays are widely used for the measurement of nucleotides in solution.[100] The utility of fluorescence binding assays for determination of DNA loading in nanoparticles is limited to measurement of the effluent once nanoparticles have been formed.[101] Unfortunately, these methods require complexation or reaction with target nucleotides. A hallmark of most non-viral DNA delivery systems is the inclusion of a cationic macromer or lipid to electrostatically combine with the negatively charged DNA. The inclusion of such molecules, while often necessary for efficient delivery, further complicates measuring the amount of nucleotide present by competing with assay reagents. With this context, groove-binding (or groove-fitting) techniques that rely on intercalation of a fluorescent dye with the DNA backbone often fail to accurately measure DNA once it has been complexed with cationic macromers. For example, widely used Qubit fluorometers are utilized with highly sensitive Next-Generation and single-cell RNA sequencing experiments but have been shown to be less accurate than standard qPCR if DNA complexation has occurred, for example with polyethylenimine (PEI), the most widely used complexing agent.[100–103] These issues are further exacerbated when the genetic materials to be assessed are integrated into material systems which further obscure probe binding sites.

2.2.3 Limitations of Colorimetric Assays for DNA Measurement in Crosslinked Nanoparticles

Similarly, digestion-based colorimetric assay methods such as the diphenylamine (DPA) assay, while robust enough to measure the quantity of DNA present in cells or in the presence of additives, require digestion of the sample via exposure to strong acids and mutagens, which present health hazards to users.[104,105] This results in the destruction of the sample being measured and can complicate interpretation by the generation of byproducts that convolute quantitation. The high protein mass ratio in SPNP systems relative to isolate and biological systems magnifies this convolution further. For potential *in vitro* use, this prevents the researcher from using the same sample that was measured for further studies, requiring batch splitting, and destruction of potentially precious samples. These complications, in total, mean that SPNP genetic payloads are not well characterized by these methods due to matrix interferences, the inability to further use analyzed particles, additional at-bench requirements, and destruction of sample.

2.2.4 Limitations of Current Methods for DNA Measurement in Crosslinked Synthetic Protein Nanoparticles

The above challenges, in addition to the inability to completely dissociate and isolate pDNA from the biomolecular components of the delivery vehicle, obscure the use of other widely employed analysis techniques, such as high-performance liquid chromatography (HPLC), mass spectroscopy, PicoGreen and related assays, qPCR, and surface plasmon resonance. Resultantly, the use of protein-majority carriers for gene delivery requires different strategies to accurately assess payload concentrations 'as used'. Resultantly, this is also required to assess differences from the 'as formulated' state (e.g., payload loss) for a given manufacturing process.

While there are a few established systems capable of intracellular visualization and subsequent quantification of nucleotides, they rely on measurement carried out by flow cytometry or confocal imaging, both methods have associated issues.[106,107] Namely, they require cellular transfection and expression prior to assessment which necessitates the timing of events to be known else transient interactions can be missed. Other limitations include the resolution of the microscope and required sample destruction for staining purposes. Though quantification of total emissivity and subsequent correlation to dose is possible in these systems, it is far from trivial to accomplish. Additionally, as quantification is done after transfection, these methods cannot elucidate the input amount prior to nanoparticle usage in the cells.

2.3 Aims of This Work

This work presents a fluorescent plasmid backbone labeling (PBL) strategy for providing accurate, quantitative payload assessment within a nanoparticle system that is agnostic to synthetic protein nanoparticle (SPNP) components and crosslinking. A model delivery system is used that is composed of crosslinked human serum albumin (HSA) and SPNPs containing a plasmid DNA. The plasmid payload is electrostatically complexed to PEI, and the SPNPs are prepared using the established EHD jetting techniques.[26,30,32] Fluorescence was assessed directly, which allowed for detection of SPNP encapsulated nucleic acids. This approach is also appropriate for high protein concentration solution-based systems where the presence of proteins and other molecules do not allow for reliable sample assessment due to requirements of surface-availability or low competition/complexation for the analyte. The method presented here allows assessment of DNA content in both solution and tightly crosslinked particles with proteins and macromers present, without destroying the sample. This enables dosage information acquisition without necessitating transfection of target cells. This is accomplished without either confocal imaging or flow cytometry; both of which require higher level technical expertise, are more expensive, time-point specific, sample destructive, fail to provide ‘as delivered' information, and complex and laborious to perform quantitatively for this purpose.

This approach enables researchers to directly, accurately, and repeatably assess the quantity of nucleotide loaded into their delivery system without interference from a protein rich environment or complexed macromers. It allows for future assessment of the sample since it is non-destructive in nature, allowing a single population to be assessed throughout a project. Furthermore, PBL utilizes a commercially available kit for cell-tracking and quantification and is done at a recommended labeling density for intracellular tracking, allowing for in situ characterization. When combined with particle size distribution data, this strategy allows for quantification of dosing mass, particle number, and average plasmids per particle. This information can be gathered for a broad range of SPNPs, providing critical information required by regulatory agencies. In summary, the strategy presented herein allows for detailed nanoparticle characterization prior to *in vitro* study, assisting in system optimization and interpretation of biological outcomes.

2.4 Methods

2.4.1 Conjugation of Cy3 Reagent to plasmid DNA

The manufacturer instructions in the Mirus *Label* IT Kit (7020) were followed to target a labeling density of 150-200 base pairs (BP) per dye molecule. This enables future use at this labeling density *in vitro* or for further methods not used herein. The manufacturer offers clear instructions on altering the labeling density of dye on nucleotide backbone, should the reader require a different density. Briefly, the Cy3 reagent was resuspended in the recommended amount of reconstitution solution Buffer “A” provided.

Next, a solution was prepared of UltraPure DNase/RNase free water and the 10X Labeling Buffer provided in the Kit. To this the desired quantity of plasmid DNA was added. Finally, the appropriate amount of Label IT Reagent for the target labeling density was added. The reaction was incubated at 37°C for 1 hour, pulsing the reaction in the centrifuge for 30 minutes to recollect any evaporation, then an ethanol precipitation was carried out to isolate the labeled DNA (Cy3-DNA). The resultant Cy3-DNA was resuspended in 100 µL of DNase/RNase-free water for quantification.

DNA Labeling Reaction	
UltraPure DN/RNase-free water	750 µL
10X Labeling Buffer ("A")	100 µL
1 mg/mL eGFP plasmid DNA	100 µL
Label IT Reagent	50 µL
Total Volume	1000 µL

Table 2-1. DNA Labeling Reaction amounts and order of addition.

2.4.2 DNA measurement using UV-Vis Spectroscopy

UV-Vis measurements as reported in Tables 1-3 were taken with cuvette-free UV-Vis on the microwell attachment of a SpectraMax m5 microplate reader. These measurements are equivalent to those obtained from a Nanodrop (Thermo) microvolume UV-Vis benchtop spectrometer, a staple in many laboratories handling DNA and/or protein. Three absorbance spectra were taken per sample from 200-700nm with a step size of 2 nm. For DNA quantification the equation used to calculate pDNA concentration is:

$$C_{DNA}(\mu g/mL) = (A_{260} - A_{280}) * dilution\ factor * 50\ \mu g/mL$$

Equation 2-1. Calculation to find the amount of Cy3-DNA following reaction

2.4.3 DNA Measurement Using the Qubit Fluorometer

Assay kits designed for use with the Qubit system, a benchtop fluorometer, were obtained from Invitrogen. The Qubit dsDNA BR kit was used to measure the amount of DNA present in samples. Manufacturer instructions were followed to obtain measurements from the Qubit 4 fluorometer. For this study, 10 µL of sample was utilized per read and each read was done in triplicate with a rest time of 30 seconds at room temperature in between reads.

2.4.4 Determination of Cy3 Labeling Density

Detailed instruction for this section can be found in its entirety in Chapter 3. Briefly, a SpectraMax m5 plate reader with a microwell attachment for UV-Visible spectroscopy, a Mirus Cy3 *Label* It Kit (7020), and GFP-pDNA were used.

To begin, an absorbance spectrum of the fluorophore, the pDNA, and the conjugated and purified Cy3-DNA product are taken independently. To enable measurement of all spectroscopic features and obtain a background measurement, each absorbance spectrum is taken from 200-700 nm with a step size of 2 nm. Absorbance values obtained from 680 – 700 nm are attributed to background noise as they are far from the spectroscopic signature of any component molecule, and especially DNA (260nm) and Cy3 (550nm). Within each spectrum, these values are then averaged, and this value is subtracted linearly from their respective spectra. Going forward, all analysis is done with background corrected spectra.

Beer's Law and the DNA-Cy3 value obtained from UV-Vis spectroscopic measurements are then used to obtain the Dye Correction Spectrum. This is then graphed along with the Cy3-DNA absorbance spectrum and adjusted until these two spectra overlap entirely in a graphical representation. This step is done to ensure that the UV signature of the Cy3 moiety can be accounted for when using that region of the spectra for DNA determination.

The Dye Correction Spectrum is then subtracted from the Cy3-DNA spectrum to obtain the DNA Quantification Spectrum. This new spectrum represents the background adjusted amount of DNA in the Cy3-DNA product and is then used to calculate the number of DNA molecules. The uncorrected DNA-Cy3 spectrum is used to determine the number of Dye molecules in the Cy3-DNA reaction product. This can be reported either as dye per DNA or BP per dye. The Beer Lambert law can then be used to obtain the value of Cy3 in the Cy3-DNA reaction product.

2.4.5 Generation of Cy3-DNA Calibration Curve

Detailed instruction for this section can be found in its entirety in Chapter 3.

2.4.6 Generation of Diphenylamine Assay Calibration Curve

Information regarding generation of the diphenylamine assay standard curve and experimental plan can be found in Appendix A.

2.4.7 Preparation of Cy3-DNA Loaded Synthetic Protein Nanoparticles

SPNPs with a Cy3-DNA payload were prepared by electrohydrodynamic (EHD) jetting. The resultant conjugation product is diluted with unlabeled DNA to a dye per BP concentration of 1:1000, this mixture is used in SPNP fabrication. It should be noted that this dilution with unlabeled materials allows for the dye ratio to be constant for all studies in a series. Additionally, since each dye labelling reaction will result in a somewhat different extent of labelling, this allows different batches of DNA-Dye conjugate to be utilized in the same study since the final ratio with dilution will always be constant.

Prior to SPNP fabrication, the Cy3-DNA and PEI were complexed at room temperature for 30 minutes at the desired nitrogen to phosphorous (N/P) ratio. For the solvent, 80:20 vol% of water-to-ethylene glycol ratio was used. Protein solutions were prepared by addition of DNA/PEI, 10% w/w NHS-PEG-NHS crosslinker, 1% w/v HSA, and 0.5% w/v HSA-405 to the solvent system. The solution was pumped using a syringe pump at 2.0 mL $hr^{-1.}$ Once a droplet formed on the end of the needle, an electric field (5 kV) was applied to obtain the characteristic Taylor Cone. Due to the voltage applied, the solution was atomized and pulled towards the grounded plate 20 cm away, resulting in electrospray of particles. The resultant SPNPs were then allowed to crosslink for 7 days in a 37°C incubator before being collected in phosphate-buffered saline (PBS), followed by serial centrifugation to obtain target sizes of less than 300 nm. The formulation for the SPNP sample used for comparisons of the four DNA assessment methods is listed in (**Table 2-2**) below.

Component	**SPNP Composition**		
	Mass	**Moles**	**m/m of total**
	(μg)	**(nmol)**	**(%)**
pDNA	289.47	0.128	4.68%
PEI	373.68	14.947	6.04%
HSA	5000.00	75.188	80.80%
HSA-405	25.00	0.376	0.40%
Crosslinker	500.00	1250.000	8.08%

Table 2-2. This is a representative formulation based on a sample preparation of 5 mg of HSA SPNP. Cy3-DNA at the designated 1000:1 bp/dye was used for assessment via the PBL strategy.

This is a representative formulation based on a sample preparation of 5 mg of HSA SPNP. In this work, unlabeled pDNA was used for established DNA quantification methods and Cy3-DNA at the designated 1000:1 bp/dye was used for assessment via the PBL strategy.

2.4.8 Characterization of Synthetic Protein Nanoparticles — Scanning Electron Microscopy (SEM)

SEM images were taken using a FEI Nova 200 Nanolab SEM/FIB at the Michigan Center for Materials Characterization at an acceleration voltage of 5kV. Images were processed using ImageJ (Wayne Rasband, NIH) to obtain their size and circularity distributions. For particle size distributions, an n > 400 was used.

2.4.9 Characterization of Synthetic Protein Nanoparticles – Number Average Dynamic Light Scattering (nDLS)

DLS measurements were carried out using a Zetasizer Nano ZS (Malvern Panalytical). nDLS was employed to measure the particle size distribution in 1x PBS buffer at room temperature after particle collection and prior to TGA analysis. 3 individual measurements were carried out per sample and averaged to determine the particle size on a count basis.

2.4.10 Determination of Cy3-DNA Percent Loading in SPNPs

Detailed instruction for this section can be found in its entirety in Chapter 3.

2.5 Results and Discussion

The materials and methods used to arrive at the results and conclusions presented in this Chapter are presented in Chapter 3 in full detail. Every effort has been made to include relevant notes and expert advice for reproducing the strategies presented.

Gene delivery is becoming increasingly important to the field of nanomedicine, and the interest in translation of these systems necessitates foundational understanding of both the delivery system and the nucleotide dosing.[108] The difficulty of characterizing nanomaterials and their payload is well-established and is at the heart of several guidance documents published by the Food and Drug Administration (FDA). Prior to filing of an Investigational New Drug application with the FDA, the efficacy and safety must be determined as well as a fundamental understanding of the physicochemical properties of the nanoparticle.[76]

2.5.1 Impact of Work Presented Here

Here, a strategy for in-particle quantification of DNA payload is presented and compared to conventional assessment methods, including UV-Vis spectroscopic methods, groove-fit fluorescence assays (fluorometric assays), and digestion-based colorimetric assays (e.g., diphenylamine). The establishment of this PBL-based quantification regime is used in tandem with Dynamic Light Scattering (DLS) measurements to assess the particle size distribution in context of plasmid-per-particle and the distribution of total plasmid for several different fully characterized SPNPs. In total, this allows for simultaneous assessment of payload by mass, by particle number, or on a plasmid-per-particle basis. Combination of the PBL and DLS methods presented here proved more accurate than the aforementioned conventional quantification methods, including for measurements of solution-based (containing DNA and SPNP substituents) and solid-phase (utilizing a fully crosslinked SPNP system) nucleotides. That is, the PBL strategy retains very low bias (<5%) in the presence of protein, complexing macromers, and other fluorescent dyes; the strategy is also agnostic to the formation of nanoparticles and SPNP incorporation, both of which make quantification with other systems problematic.

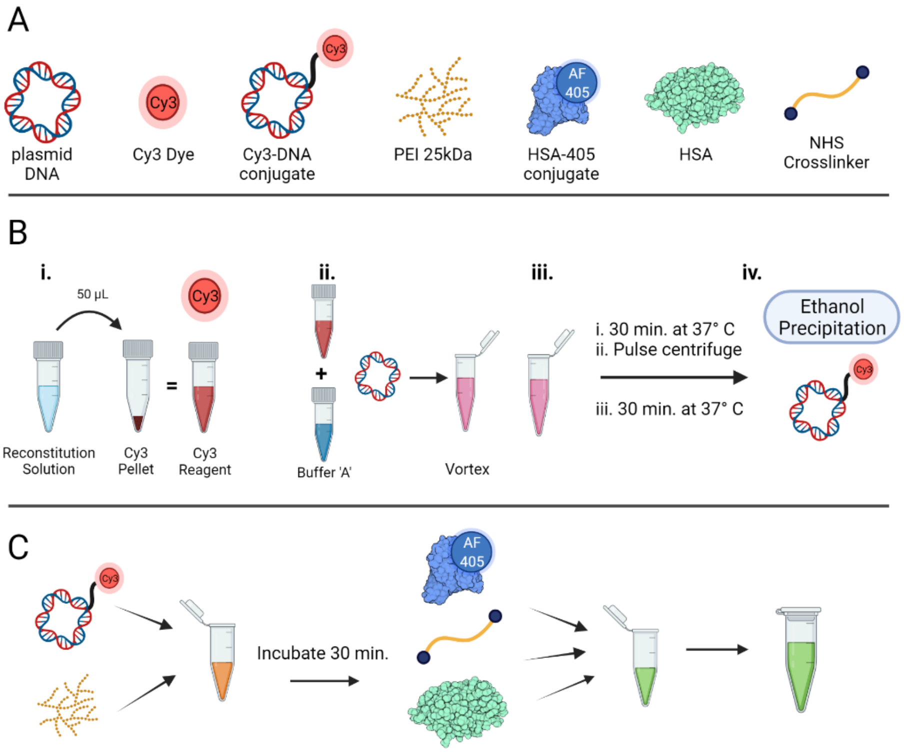

Figure 2-1. (A) Critical Components of SPNPs (B) Cy3-DNA Conjugation Strategy, SPNP Preparation and Processing (C) Preparation of the jetting solution with component molecules.

To create a model material-based delivery platform for PBL evaluation, we utilized established electrohydrodynamic jetting (EHD) of a protein carrier solution and pDNA payload to make SPNPs. This carrier solution could be easily modified with fluorescently labeled pDNA to evaluate the PBL method, as outlined in **Figure 2-1**. A detailed description of labeling density determination and calibration curve generation following the conjugation of Cy3 to the pDNA backbone is found in the methods section of this report.

To evaluate the ability of PBL to quantify DNA concentration in a variety of environments, we created SPNPs suspensions (**Figure 2-1**) alongside isolated DNA and Human Serum Albumin (HSA) solutions, and measured their DNA content via PBL, comparing directly to established DNA measurement methods, including microvolume UV-Vis spectroscopy, a commercial assay utilizing a fluorescent groove-binding technique, and a well-established digestion-based colorimetric diphenylamine assay.

Method	Commercial Method	DNA Concentration	Observed Concentration	In Batch Variability	Average Bias	Average Variability Between Runs
		µg/mL	µg/mL	(%)	(%)	(%)
UV-Visible Spectroscopy	NanoDrop ™	579.00	585.72	1.7	+1.16	-8.18
Fluorescent Binding Assay	Qubit ™		564.05	1.8	-2.58	-13.16
Colorimetric Assay	Diphenylamine Assay		574.74	1.9	-0.74	+0.28
Fluorescent Plasmid Backbone Labeling	N/A (reported here)		587.72	0.9	+1.51	-3.94

Table 2-3. Assessment of just DNA using UV-Vis, fluorescence binding, digestion-colorimetric, and PBL strategies. Broadly, all methods appear fit-for-use for research applications.

2.5.2 Isolated Payload and Matrix Studies

Firstly, when looking at the ability of PBL to assess isolated DNA in solution (in water), we observed that all four methods can quantify the amount of DNA present in solution (**Table 2-3**), as expected. Each technique also had low in-batch variability as determined by replicate measurement (n=20) with each instrument or technique (**Table 2-3**). Nominally, the DPA was found to be the least biased of the four methods, though PBL had a lower bias (average relative percent difference) than commercial assays. It was also found that the batch-to-batch variability of both the DPA and PBL strategies are lower than the conventional methods, even fluorescence-binding assays, which notably require instrument calibration prior to use. Indeed, for pure pDNA in water, all methods appear fit-for-use in a research environment.

Before conducting direct testing of SPNPs, we benchmarked the effect of HSA without DNA to determine the ability of the various techniques to observe DNA in an impure solution with HSA background. This allowed us to calibrate each method for the HSA contribution to DNA signal, allowing for correction when a known amount of HSA is present in the studied systems (**Table 2-4**). As expected, the UV-Vis measurement detected about a third of the HSA as DNA; this indicates a large error that may present issues reading protein-DNA solutions if care is not taken to address the protein interference. The fluorescent binding assay read less than 3% of HSA as DNA, a background that is both small and correctable, while the DPA and PBL strategies read far less than 1% of HSA as DNA. This implies that the PBL and DPA are fit for use in solutions where HSA is present, while the binding assay also appears to provide reasonable results (assuming that the HSA concentration is sufficiently low). While in theory it may be possible to use full spectral deconvolution UV-Vis for assessment of an HSA and DNA solution, this is not trivial and likely too labor-intensive for widespread application.

Method	**Commercial Method**	**HSA Concentration**	**Observed DNA Concentration From HSA Interference**	**HSA Observed as DNA / Bias**
		µg/mL	**µg/mL**	**(%)**
UV-Visible Spectroscopy	NanoDrop ™	500.00	164.45	+32.89
Fluorescent Binding Assay	Qubit ™		11.22	+2.24
Colorimetric Assay	Diphenylamine Assay		0.07	+0.01
Fluorescent Plasmid Backbone Labeling (PBL)	N/A (reported here)		0.27	+0.05

Table 2-4. Assessment of HSA background and DNA observed in an HSA-rich environment using UV-Vis, fluorescence binding, digestion-colorimetric, methods and PBL strategy in water. UV-Vis spectroscopic measurements have the highest HSA interference, all other methods are fit for research use.

2.5.3 Combined Matrix and Payload Studies

We next created solutions containing both HSA and DNA to evaluate the efficacy for each method in determining DNA content in an impure solution (**Table 2-5**). Importantly, here we utilized the previous experiment (**Table 2-4**) to account for HSA interference/bias and corrected all DNA readings for HSA content; briefly, the percent of HSA expressing as DNA was multiplied by the HSA concentration and subtracted from the total amount of DNA observed for each unique technique. This value is presented as DNA Observed and the bias (%) is reported for each method. Upon baseline correction, the UV-Vis method has a bias of less than +2%, similar to the PBL strategy. In contrast, the DPA and fluorescent binding assay struggle to accurately quantify the amount of DNA in HSA solution, with the DPA possessing a bias over +12% and the fluorescent binding assay almost doubling the expected result.

Method	**Commercial Method**	**DNA Observed**				**HSA Corrected**	
		DNA Concentration Known	**HSA Concentration Known**	**DNA Observed Raw**	**HSA Observed as DNA / Bias**	**DNA Observed**	**Bias**
		µg/mL	**µg/mL**	**µg/mL**	**µg/mL**	**µg/mL**	**(%)**
UV-Visible Spectroscopy	NanoDrop ™	579.00	312.00	691.16	102.62	588.55	+1.65
Fluorescent Binding Assay	Qubit ™			53.13	7.00	46.13	-92.03
Colorimetric Assay	Diphenylamine Assay			651.65	0.04	651.61	+12.54
Fluorescent Plasmid Backbone Labeling (PBL)	N/A (reported here)			587.80	0.17	587.63	+1.49

Table 2-5. Assessment of DNA in fully crosslinked SPNPs using the four methods in water. Only the PBL strategy is fit for use in assessment of the DNA in HSA-based SPNPs.

2.5.4 Assessment of Payload in Synthetic Protein Nanoparticles

Having established the extent of HSA interference and the accuracy of each method with HSA present, fully crosslinked SPNPs were prepared using EHD jetting

(**Figure 2-2**) then the amount of DNA present within them was quantified (**Table 2-6**). Following HSA interference correction, the UV-Vis method is wildly inaccurate with a >-600% bias. This is expected, as UV-Vis can be confounded by scattering induced by nanoparticle-sized particulates in solution, and corrections based on single point background subtraction are rarely robust.

The fluorescence-binding assay is likewise inaccurate, with a bias of nearly -50%. This inaccuracy compared with assessment of DNA in isolation, indicates that the surface availability of the plasmid is not sufficiently high for a binding assay to accurately quantify. That is, it is likely that the majority of the pDNA loaded into the SPNPs is internalized or otherwise unavailable for binding. Surprisingly, the DPA assay on digested SPNPs was also inaccurate with nearly +75% bias, notably higher than the +12% observed in the previous assessment of DNA and HSA in solution.

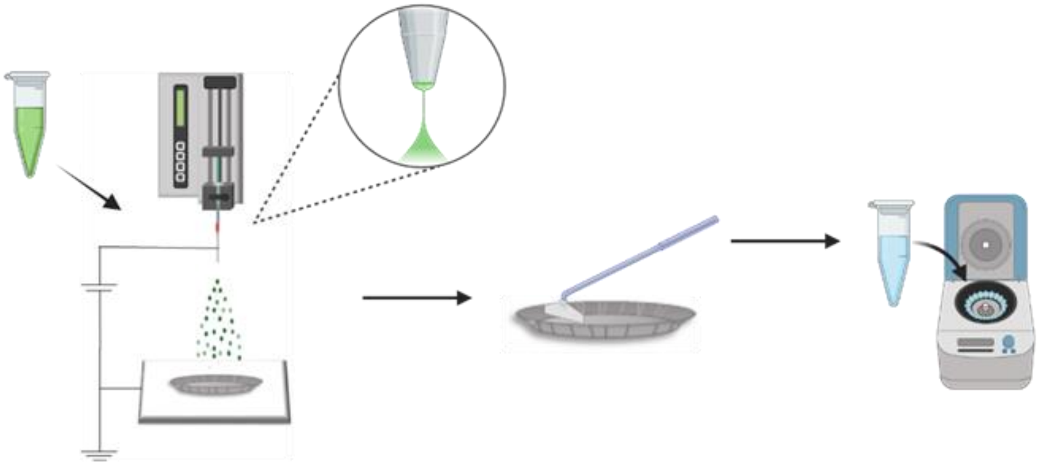

Figure 2-2. Electrohydrodynamic jetting is used to prepare synthetic protein nanoparticles discussed in this work. These SPNPs are then processed via centrifugation to achieve the desired size range of < 300nm.

Given that an incomplete digestion of the SPNP would lead to a negative bias in the DPA reading, a high positive bias for the DPA assay is unexpected; this may be due to SPNP degradation products that are amenable to DPA binding.

While the wavelength of this measurement (595 nm) is not in the UV range, it is also likely that any residual undigested particle scatter could also interfere positively. This said, until working with crosslinked SPNPs, the DPA method was relatively facile and performed on par with PBL, highlighting the difficulty in characterizing complex delivery systems. Importantly, the PBL strategy is found to have a low bias (< -3%) even in fully crosslinked SPNPs. The primary advantage of the PBL strategy is that the high accuracy of the readouts in both solution and in fully crosslinked SPNPs is constant, regardless of whether they represent an HSA-rich or HSA-poor environments.

Robust performance of PBL across different systems will also allow for direct comparison of different technologies and processes steps, while the non-destructive nature also makes it uniquely appealing for samples with costly, unique, or limited samples.

2.5.5 Plasmid Backbone Labeling Strategy Workflow

Having benchmarked assay performance for nucleotide measurement of DNA, HSA, DNA and HSA, and the SPNPs next a workflow to assess DNA loaded SPNPs prior to use was developed (**Figure 2-3**). Toward this goal, a calibration curve was generated for the solution that mimics the eventual SPNP environment (HSA, PEI, HSA-405) and the target molarity of DNA in the SPNPs (**Figure 2-3c**). The concentration of HSA, HSA-405, and PEI were held constant while the amount of DNA varied across each sample.

The choice to vary the DNA, not the HSA or PEI in the calibration curve, was deliberate and allows the calibration curve to remain valid for instances where the DNA loading per particle is varied.

To ensure that the output of fluorescence (a.u.) across the dynamic range is linear and that the PBL strategy is repeatable, calibration curves were generated in triplicate and interrogated using statistical methods. Firstly, prior to quantification of Cy3 present, the reaction product of Cy3-DNA was evaluated using UV-Vis spectroscopy and found to contain the expected absorbance peaks of both DNA at A_{260} and Cy3 at A_{550}. A calibration curve was generated from fluorescent reads in triplicate across the target range of DNA in SPNPs.

Then, a linear regression was used on the resultant curves to determine goodness of fit (r^2) and evaluated statistical differences between the slopes of the three lines of best fit to determine a p-value ($p = 0.9335$), thus the hypothesis that the data points are from different sets is rejected. This suggests that the standard curves generated have a high degree of linearity and are not statistically different from each other, allowing confidence that the standard curves generated for determination of Cy3-DNA in a SPNP environment are reliable and repeatable.

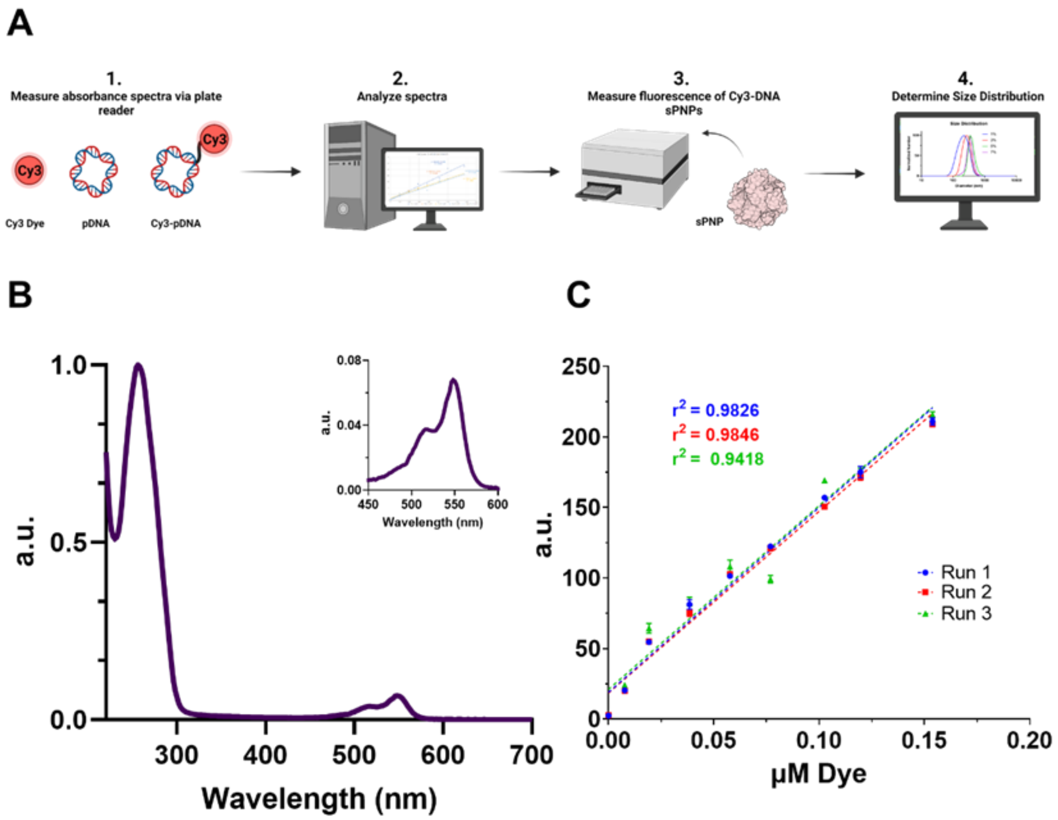

Figure 2-3. Workflow of PBL process and evaluation of Cy3-DNA conjugation and generation of calibration curves for the fluorescent plasmid backbone labeling (PBL) strategy. (a) schematic of the workflow of the PBL (A) Absorbance spectrum of Cy3-DNA reaction product showing characteristic DNA peak at A_{260} and Cy3 at A_{550} (B) Calibration Curve in triplicate across the target range of DNA in SPNPs. All points on curves are measured n = 3 times with 95% confidence interval shown.

nDLS	SEM	Target DNA per particle	Particle Mass Dose	Particles per Dose	Observed DNA per particle	Relative DNA per particle Loading	DNA per protein	DNA Mass Dose	Number DNA per Dose	Plasmid Average per Particle With:			
Average Diameter	Average Diameter									Average Diameter (Target)	Average Diameter (Observed)	D = 150 nm (Target)	D = 150 nm (Observed)
(nm)	(nm)	(m/m %)	(μg)		(m/m %)	(%)	(m/m %)	(μg)		#Plasmids	# Plasmids	# Plasmids	# Plasmids
186	84	1.0	10.0	4.96×10^8	0.2	16.5	1.1	0.02	4.25×10^9	8.56	1.41	6.15	1.01
223	72	2.8	10.0	5.79×10^8	0.8	27.1	3.4	0.08	1.99×10^{10}	34.38	9.31	17.56	4.75
146	100	4.4	10.0	3.70×10^9	3.5	78.5	5.8	0.35	9.19×10^{10}	24.86	19.50	27.96	21.94
185	92	5.2	10.0	1.02×10^9	4.1	79.5	7.0	0.41	1.09×10^{11}	107.22	85.28	61.39	48.83

Table 2-6. Calculations performed on each particle population based on nDLS size distributions. Average plasmid per particle for SPNPs of average diameter and for a diameter of 150 nm for both target and observed DNA amounts are reported.

2.5.6 Assessment of SPNP DNA Loading Efficiency

Given that different delivery systems utilize different DNA concentrations and the widespread screening of various DNA concentrations in the field, we then generated SPNPs of four different loadings. To determine the loading efficiency of pDNA into SPNPs, SPNP systems with target DNA loadings from 1.0 – 5.2 m/m% (DNA/SPNP) were generated and their observed DNA loading was measured. The DNA content of fully crosslinked SPNPs was then obtained from the emission curves. It is of note that the observed and target DNA loading vary significantly, but that the relative loading efficiency increases with an increasing target DNA amount (**Table 2-6**).

This trend can be graphed and fit to either a sigmoidal or linear curve and the maximum theoretical relative DNA loading can be calculated (**Figure 2-4**). The sigmoidal fit has a maximum of 82% relative DNA loading, which is approached asymptotically. This maximum value is close to the 80% achieved by the SPNP with the highest target DNA amount achieved here. A linear fit, on the other hand calculates a 100% relative DNA loading will be achieved at a target DNA just over 6.2 % (DNA/SPNP), which is greater than is possible in the current system. Preparation of a 7.0 % (DNA/SPNP) SPNP was attempted, but abandoned when the jetting solution continued to precipitate prior to EHD jetting. The ability to determine maximum DNA loading per SPNP in instructive for changing the formulation of SPNPs and the predictive ability this gives for determining the loading efficiency of the system relative to the target DNA %.

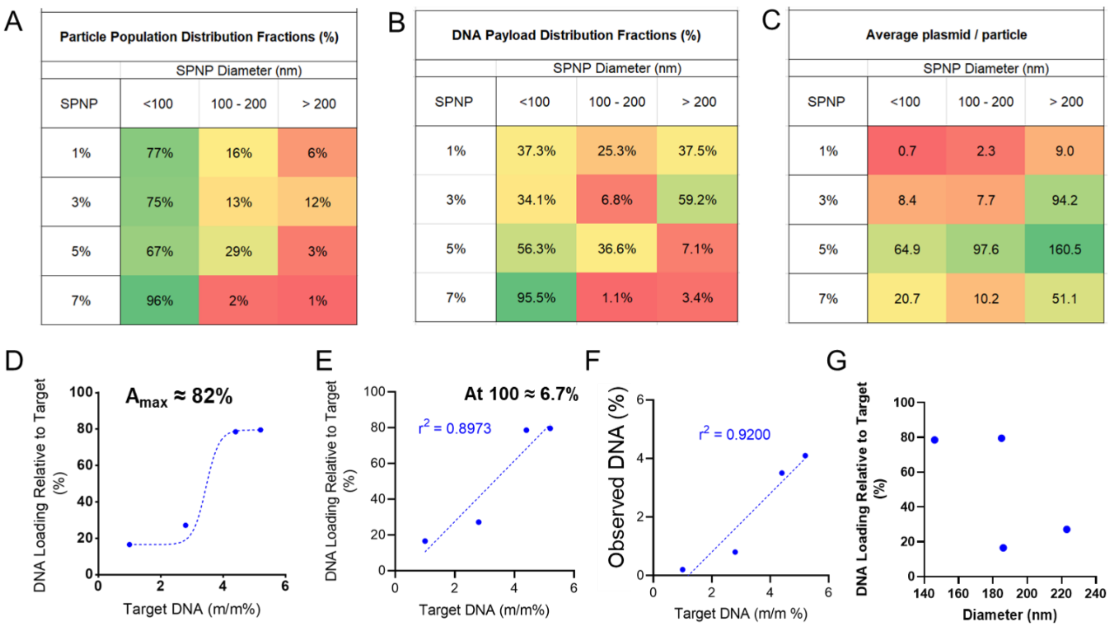

A

Particle Population Distribution Fractions (%)			
	SPNP Diameter (nm)		
SPNP	<100	100 - 200	> 200
1%	77%	16%	6%
3%	75%	13%	12%
5%	67%	29%	3%
7%	96%	2%	1%

B

DNA Payload Distribution Fractions (%)			
	SPNP Diameter (nm)		
SPNP	<100	100 - 200	> 200
1%	37.3%	25.3%	37.5%
3%	34.1%	6.8%	59.2%
5%	56.3%	36.6%	7.1%
7%	95.5%	1.1%	3.4%

C

Average plasmid / particle			
	SPNP Diameter (nm)		
SPNP	<100	100 - 200	> 200
1%	0.7	2.3	9.0
3%	8.4	7.7	94.2
5%	64.9	97.6	160.5
7%	20.7	10.2	51.1

Figure 2-4. The particle distributions and loading relative to target. Heatmaps represent the distribution of (A) SPNPs (B) pDNA and (C) the average number of plasmids per particle in each population prepared. The DNA loading relative to the target is then graphed against target DNA (m/m)% and fit with to a (D) sigmoidal or (E) linear curve to describe the maximum loading or target DNA used in SPNP formulation to attain a 100% loading. Next, (F) the observed DNA % is graphed against target DNA (m/m)% and fit to a linear curve. Other relationships such as (G) diameter vs. DNA loading relative to target (%) were examined but the fit did not converge and thus no correlation coefficient is reported.

2.5.7 Detailed Loading Analysis from Size Distribution

To explore DNA loading at the particle level, dynamic light scattering (DLS) measurements for each SPNP system were obtained. Specifically, the number average DLS (nDLS) distribution (Appendix A) was extracted from the intensity average distribution (iDLS), which is directly derived from the DLS spectra. The nDLS values were used to calculate how the DNA is distributed across the SPNP population. This allowed calculations of average per particle loading of plasmids based on the distribution of SPNPs achieved using EHD jetting (**Table 2-6**). Here, the number of plasmids in SPNPs of average diameter and at a diameter of 150 nm are compared. The data presented in **Table 2-6** also enables calculation of how the SPNPs are distributed within the overall particle distribution and can be extended to where the plasmid population lives within the particle size distribution.

To explore how the population of plasmid correlates with the population of SPNPs, heatmaps in **Figure 2-4 (A-C)** were generated. Here, the percent of SPNPs with a nDLS diameter below 100 nm accounts for between 75 and 96 percent of the total SPNPs measured, which correlates to most of the plasmid dose contained within those particles. It may be counterintuitive that smaller particles would contain a majority of plasmid, however, this is expected as there are many more particles in that size range on an absolute level, compensating for their smaller size. The second largest population of particles is within the 100 -200 nm diameter size range yet accounts for the lowest percentage of the plasmid. When normalizing to particle number (**Figure 2-4C**), it is found that the particles with the highest average plasmid concentration per particle is found for the > 200 nm diameter size range, which is unsurprising as the diameter corresponds to a $\left[\frac{d}{2}\right]^3$ scaling factor to the volume. That is, the larger the particle, the more room it has inside it to fit pDNA and the higher percentage of the population one would expect to see contained in that size range.

2.5.8 Repercussions Of Particle Distribution on Payload and Dose Considerations

A benefit of utilizing this tandem PBL/DLS method to assess particle loading heterogeneity is that it allows analysis of the effect of intra-population particle heterogeneity which the field has not fully explored. To explore where the plasmid population lives, payload distribution fractions were calculated and used to report the average plasmid per particle within those. This enables a discussion on where the bulk of the particles are as well as where the DNA dose is within the SPNPs, which is largely heterogeneous. Researchers that obtain the bulk of DNA loaded into particles outside of the intended target size range would benefit from this knowledge and could then purify their sample prior to use to maximize the efficacy of said particles and deliver less exogenous material for example when conducting transfection studies.

When examining the heat maps (**Figure 2-4C**), it is apparent that the second largest population of SPNPs is within the 100 – 200 nm diameter range. However, as can be seen from the **Figure 2-4B**, the fraction of pDNA within SPNPs in this size range is not the highest, due in large part to how few particles there are within this size range compared to those in the < 100 nm diameter range (**Figure 2-4A**). Suggesting that if the highest payload of DNA per particle were required, this population could be excluded or minimized. This level of granular detail is useful for researchers that are not aware of heterogeneity of their particle populations and enables exploration into which particle fractions would be the most effective in a study. For example, it would be advantageous to know if larger particles have a higher payload but cannot be taken up by target cells, or if particles of a particular size offer advantageous, uptake, efficacy, or otherwise, over a different size population. Nanoparticles are often polydisperse[109], and an interrogation of particle size and loading as laid out here can act as a roadmap for researchers that would benefit from this level of granularity in their particle analysis.

While this work uses DLS to obtain particle size distribution information coupled with the PBL strategy for pDNA quantification, other size characterization methods (SEM, AFM, TEM, Nanosight™, etc.) and gene content analysis methods could also be used (mass spectrometry, elemental analysis, etc.) and the same methodology for obtaining detailed loading analysis can be applied.

2.5.9 Benefits and Application of PBL In Gene Loaded Nanoparticles

The recent success of mRNA vaccines and advances using CRISPR/Cas9 systems all but ensure that gene-based therapies will continue to expand in utility and scope in various therapeutic areas. The continued expansion and application of gene therapies necessitates a thorough understanding of the delivery system. Issues associated with conventional methods of DNA quantification in nanoparticle systems make assessment of loading efficiency and payload amount extremely challenging. PBL enables a high degree of certainty in measurement of DNA within a crosslinked SPNP not achieved by the three conventional methods tested here. This information can be used to inform the design of future formulations based on target loading percent and plasmid distribution throughout the particle population. Information about dose dependence can also be gathered using this method, as the exact amount of DNA delivered is known.

Using the PBL strategy requires minimal chemistry knowledge, small amount of analyte, and access to readily available instrumentation. The kit used here is commercially available and not cost-prohibitive and the fluorophore and nucleic acid can be easily changed while retaining the methodology presented here. The use of another fluorophore within the PBL system demonstrates the ability of the PBL strategy to be applied in an environment where there will be other fluorophores present, such as during cell staining for use with microscopy or flow cytometry. This method does not, however, require transfection into target cells and can be used to calculate doses of DNA prior to transfection, while allowing for intracellular tracking following transfection. PBL is also non-destructive to the sample, requiring less sample to be prepared, and meaning that the sample tested can be the same sample administered. PBL reports low bias in fully crosslinked particles without the use of mutagens and strong acids necessary for some methods.

The repeatability and speed of this technique also lend it to scale-up and it represents a useful tool for various researchers in the biotechnology space. If routine and destructive testing is appropriate, DPA should be used unless it proves to have the complications outlined here. In systems with low scatter and low spectral overlap, UV-Vis spectroscopy methods should be used. While it’s possible that fluorescent binding assays may provide information about surface availability, they should generally be considered unreliable for the quantification of tightly bound genetic payloads.

2.6 Conclusions

This work presents a strategy for the quantitative characterization of encapsulated plasmids within fully crosslinked SPNPs that is more accurate and has a lower bias than conventional methods while laying out a roadmap for assessment of payload quantification based on PSD. While the model system utilized in this work is a protein-rich SPNP, a variety of bio macromolecular gene-host systems may benefit from this quantification approach. This approach is widely and readily applicable to other NP and gene-host systems and could be applied to adjacent fields for many wide-ranging applications. Detailed analysis of DNA quantification using PBL, and three conventional methods demonstrated that the PBL strategy exhibits higher accuracy and lower bias even in crosslinked SPNPs. Using PSD determined by DLS in combination with DNA measurements obtained with PBL, a detailed analysis of the per-particle loading and heterogeneity within the particle population was discovered.

The strategies outlined provide a roadmap for other researchers seeking to gain a better understanding of nucleotide payload within their nanoparticle systems. While the fluorescent dye may need to be custom-selected and calibration curves will need to be generated based on system specifics, this methodology may be useful for other types of gene delivery, not just those encapsulated within proteins. The result of this work allows future investigations into the rational design of SPNP systems with genetic payloads and a thorough understanding of design and parameter changes on genetic payload on a per-particle basis.

Chapter 3

In-Depth Protocols for Characterization of plasmid DNA Loaded Synthetic Protein Nanoparticles

3.1 Introduction

This project utilized a fluorescent plasmid backbone label (PBL) strategy to quantify nucleic acid loading in tightly complexed synthetic protein nanoparticles (SPNPs) for gene therapy applications.

Although some steps of this method exist elsewhere and these techniques are readily available, the intent of this section is to assemble all steps in a way that allows a researcher to adopt, in part or in whole, the methods outlined herein. The step-by-step instructions presented here are accompanied by expert notes of best-practices and lessons-learned along the way while this strategy was developed. Where present, these will be indented and italicized. By reporting in-depth protocols like so, I strive to provide superior accessibility and streamlined roadmaps for future researchers.

The fluorophore used in this work, Cy3, was chosen carefully so it is far from the absorbance signal of DNA (A_{260}), and human serum albumin (HSA) (A_{280}), the protein used here. It is also cohesive with the fluorescent labeling scheme of the SPNPs used for this project, which have AlexaFluor 405, and far from the excitation and emission spectra of the GFP-pDNA, which expresses at 488 nm. For these reasons, Cy3 (Mirus *Label* It Kit 7020) is used in this work, but the reader should choose the fluorophore that suits their system. The methodology and workflow described here remains the same regardless of the fluorophore chosen, provided the system does not contain any overlap in either absorbance or fluorescence signatures. This adaptability makes the technology presented here widely applicable to many systems that require quantification of genetic material present.

3.2 Conjugation of Cy3 Reagent to plasmid DNA Backbone

Note: The conjugation of Cy3 to plasmid DNA (pDNA) backbone may be done before or after measuring the absorption spectra of Cy3 and DNA separately. I use different aliquots for the spectra measurements and reaction, so I have the full 50 µL of Cy3 reagent available for reaction with DNA, and a different another for Cy3 measurements. I have also had success using a small amount of the suspended Cy3 reagent (0.5 µL and dilute it for UV-Vis readings), just be sure to account for this in your reaction volumes.

Note: The protocol for obtaining and measuring the spectra is described in detail in Section 3.4 below. I typically run the spectra on the plate reader during the reaction incubation.

Note: The technical product literature and other fluorophores available for the Label IT kit can be found here: https://www.mirusbio.com/products/labeling/label-it-tracker-intracellular-nucleic-acid-localization-kits

The manufacturer instructions in the Mirus *Label* IT Kit (7020) were followed to target a labeling density of 150-200 base pairs (BP) per dye molecule.

> *Note: This labeling density regime is recommended for intracellular tracking, so it is utilized here. The manufacturer offers clear instructions on altering the labeling density of dye on nucleotide backbone, should the reader require a different density.*
>
> *Note: Those instructions and most complete protocol provided by the manufacturer can be found here:*
>
> *https://www.mirusbio.com/assets/protocols/ml054_label_it_tracker_kit.pdf*

1. Before you start the reaction, prepare the solutions and pre-cool the materials for the ethanol precipitation.
    a. Prior to first use, warm each tube provided in the *Label* IT Kit to room temperature.

       Note: I do this by taking each tube from the packaging and placing in a room-temperature tube rack inside a drawer so that they can warm up faster than in the box but are kept from light and upright.

       Note: Make sure to completely thaw each of the solutions and reagents. The tracker reconstitution solution remains frozen at 4°C and must be room temperature to thaw completely.
    b. Once the *Label* IT reagent is warmed to room temperature, pulse it in a centrifuge to ensure any volatiles are incorporated into the pellet.

       Note: I do this in a Sprout Mini Centrifuge for 2-3 seconds, 3 times total.

   c. Prepare a 5M sodium chloride solution of at least 500 µL.
   d. Pre-cool at least 1mL of 100% ethanol to -20°C.
   e. Ensure that you have at least 1 mL of room-temperature 70% ethanol on-hand.
   f. Refrigerate a centrifuge capable of reaching 14,000g to 4°C.

2. Suspend the Cy3 reagent in 50 µL of the Tracker Reconstitution Solution provided.

   Note: I always use the low-adhesion microcentrifuge tubes from Biotix for preparation of samples and the reaction described here.

   Note: Make sure that samples are well-mixed. I vortex the solution for 5 seconds then pulse it in the centrifuge 2-3 seconds one time to recollect anything that may have stuck on the walls.

3. Add the reagents in the order listed below and ensure that the *Label IT* Reagent is added last, per manufacturer instructions.

   Note: For this reaction, I label the maximum amount of DNA allowed per kit while maintaining the target labeling density of 150 bp/dye.

   Note: This labels 100 µg of plasmid DNA. See the protocol at the link listed above for instructions on changing the labeling density.

   *Note: This reaction size is for the entirety of the Kit, and I recovered a Cy3-DNA sample with between 146- 120 BP per Cy3 dye molecule each of the five times that I have done this experiment (**Table 3-1**).*

DNA Labeling Reaction	
UltraPure DNase/RNase free water	750 µL
10X Labeling Buffer (“A”)	100 µL
1 mg/mL GFP plasmid DNA	100 µL
Label IT Reagent	50 µL
Total Volume	1000 µL

Table 3-1. DNA labeling reaction amounts used in this work.

Note: Once the reagents have all been added I vortex the mixture for 2-3 seconds.

4. Incubate the reaction at 37°C for 30 minutes then remove it from the incubator and pulse it in a centrifuge.

Note: I pre-warm a tube holder in the incubator. I also seal the reaction tube with parafilm, then place in it the tube holder inside the incubator to ensure it remains upright and any volatile components are unable to escape.

Note: This step is critical to maintaining the target concentration of the reaction components and minimizes the effects of evaporation at the elevated temperature.

5. Replace the reaction mixture into the incubator for 30 minutes.

   Note: You do not need to centrifuge at the end of the reaction, as you are no longer interested in maintaining the reaction components at their desired concentration.

6. Carry out an ethanol precipitation to isolate the DNA labeled with Cy3 (Cy3-DNA).
   a. Add 0.1 volume of 5M sodium chloride and 2 – 2.5 volumes of ice cold 100% ethanol to the reaction.

      Note: For the reaction I carry out I use 2 volumes of ethanol.

b. Vortex for 5 seconds then place at -20°C for 30 minutes.

c. Centrifuge the reaction at full speed (15,000 rpm / 21130 rcf) in the refrigerated small centrifuge for 30 minutes.

> *Note: At this size of reaction, the pellet will be obvious (Cy3 is visibly pink), but if you decrease the size of the reaction be sure to keep track of where you would expect to see the pellet.*
>
> *Note: Once the tube has been removed from the centrifuge, bring the centrifuge back to room temperature.*

d. Gently remove the supernatant from the reaction tube.

> *Note: The pellet is quite sticky, so it won't move too easily, but be careful not to disturb it either.*

e. Rinse the pellet with 500 µL of room-temperature 70% ethanol.

> *Note: Vortex the mixture for 5 seconds to mix well and remove the pellet from the wall.*

f. Centrifuge the solution at room temperature and full speed for 30 minutes.

g. Completely remove all ethanol from the pellet.

> *Note: I use a 100 µL micropipette to remove all traced of ethanol.*
>
> *Note: Do NOT allow the pellet to dry for more than 2 minutes as it will be difficult to resuspend. The manufacturer recommends < 5 minutes, but it gets sticky and difficult to work with by 2 minutes drying time.*

h. Resuspend the resultant Cy3-DNA pellet in 100 µL of sterile DNAse/RNase free water for quantification.

Note: You can also use 1X Labeling Buffer "A" per the manufacturer protocol, but I use water. I don't want any potential complicating factors in the spectra while determining labeling efficiency or comparing this to any other reaction/reagent. Additionally, the Buffer is proprietary, and each Kit comes with enough for the reaction but not too much more – I do not want to be in a situation where I need more to run a blank etc. and do not have access to it.

Note: I store the Cy3-DNA in the fridge, completely covering the tube in aluminum foil to protect it from the light. The manufacturer recommends -20°C for long-term storage, but I do not because I use it within a week. I recommend preparing a new batch for each experiment.

Note: There is a troubleshooting guide in the protocol link provided, but I have not struggled with any of these issues when following the protocol listed here.

3.3 DNA Measurement Using UV-Visible Spectroscopy

DNA measurements using UV-Vis spectroscopy were taken with the microwell attachment of a SpectraMax m5 microplate reader. The reader should be aware that it is important to retain enough Cy3 reagent and purified pDNA to obtain absorbance spectra for each component prior to generation of a calibration curve.

1. Add 2.5 µL of each sample to a spot on the microwell attachment for the SpectraMax m5 plate reader. The samples are a 1 mg/mL sample of pure DNA as the control, three samples of the resuspended Cy3-DNA, and three samples of Cy3.
2. Measure the absorbance spectra for each sample from 200 – 700 nm with a step size of 2 nm.

   Note: To enable measurement of all spectroscopic features and obtain a background measurement, the wavelengths extend far beyond the expected scope of the Cy3 measurements. If you use a different fluorophore, be sure to account for this.

   Note: All measurements should be taken in the solvent system your product will be analyzed in.
3. Calculate the amount of DNA present in the sample using the following equation and be sure to keep track of any dilutions you perform.

$$C_{DNA}(\mu g/mL) = (A_{260} - A_{280}) * dilution\ factor * 50\ \mu g/mL \qquad (1)$$

Equation 3-1. This equation is used to calculate the concentration of DNA observed using UV-Vis spectroscopy

3.4 Determination of Cy3 Labeling Density

Note: I do all these calculations and data manipulation in Microsoft Excel.

1. Average the absorbance spectra obtained for each the DNA, Cy3-DNA, and Cy3 reagent to get one spectrum for each sample.

Note: I use a 10x dilution of the Cy3 reagent in water (already suspended in 50 µL), but until you do these calculations the amount of Cy3 reagent is not known, as it is proprietary. The dilution is done so that the proprietary reconstitution solution background effects are minimized, but similar spectra are obtained for 1x, 10x, 100x dilutions so this is not expected to affect the results.

2. Using the averaged absorbance spectra, average the background values (680 – 700 nm) for each spectrum and subtract this value linearly from each corresponding spectrum. Going forward, all analysis is done with background corrected spectra.

    Note: Absorbance values from 680 – 700 nm are attributed to background noise as they are far from the spectroscopic signature of any component molecule, and especially DNA (260 nm) and Cy3 (550 nm).

3. Graph the background corrected Cy3-DNA absorbance spectrum and **Equation 3-2** and zoom in on the peak max at approximately 550 nm.
4. Determine the scaling factor (**Equation 3-3**) needed to completely overlap the two lines by visual inspection of the graph generated in Step 3.

    *Note: The scaling factor (**Equation 3-3**) is approximated by the ratio of the absorbance peak max of Cy3-DNA to the absorbance peak max of Cy3.*

    a. Iterate on the multiplication factor until the overlap of the graph generated by the background corrected Cy3-DNA absorbance spectrum and **Equation 3-2** is complete by visual inspection of the graph.

        Note: A starting value of 1 for the multiplication factor can be used to decrease the rounds of iteration needed.

        Note: I have never needed a multiplication factor outside of ± 5% of 1, if you need a high one there might be something wrong.

5. Duplicate the resultant background corrected Cy3 spectra and multiply it by the scaling factor calculated in **Equation 3-3** to generate the new dye correction spectra.
6. Subtract the Dye Correction Spectrum from the Cy3-DNA spectrum to obtain the DNA Quantification Spectrum (**Equation 3-4**).

    Note: This spectrum represents the background adjusted amount of DNA in the Cy3-DNA product and can now be used to calculate both the number of DNA molecules and the number of dye molecules in the Cy3-DNA.

7. Using **Equation 3-5** and the total mass of Cy3-DNA, calculate the number of dye molecules per DNA using **Equation 3-6**.

    Note: It is important to know the dye per BP for generation of the calibration curve, as the regime at which the calibration curve is generated must be close enough to give an approximation of the system that is being measured.

$$\text{Spectra}_{\text{Dye Correct}}(nm) = \text{Spectra}\left[\frac{\text{C}_{\text{DNA, Cy3}}}{\text{C}_{\text{Cy3}}}\right] \quad (2)$$

$$\text{Scaling Factor} = \text{X} * \frac{\text{A}_{\text{552, Cy3−DNA}}}{\text{A}_{\text{552, Cy3}}} \quad (3)$$

$$\text{Spectra}_{\text{DNA Quant}} = \text{Spectra}_{\text{DNA−Cy3}} - \text{Spectra}_{\text{Dye Correct}} \quad (4)$$

$$\text{A}_{\text{550, Cy3}} = \varepsilon_{\text{Cy3}}\text{bC}_{\text{Cy3}} \quad (5)$$

$$\frac{\text{C}_{\text{Dye}}}{\text{C}_{\text{DNA}}} = \text{dye molecules per DNA} \quad (6)$$

Equation 3-(3-2-6). Relevant equations to calculate the spectra needed to generate Cy3-DNA concentrations for SPNP-loading experiments.

3.5 Generation of the Cy3-DNA Calibration Curve

To measure the fluorescence of the Cy3-DNA loaded SPNP product, a calibration curve was created across the dynamic range of DNA in our target system. Here, the dynamic range is 0.0 - 0.2 µM of Cy3-DNA as our target molarity in the SPNPs is 0.05 - 0.1 µM Cy3-DNA (0.25 – 5.0 µg Cy3-DNA). Our SPNPs contain Human Serum Albumin (HSA), AlexaFluor405, and 25kDa polyethyleneimine (PEI), a calibration curve is established for this condition.

Note: It is important to establish a calibration curve in an environment that is representative of the eventual target SPNP so that the amount of DNA can be calculated in the presence of other molecules. Readers that use different proteins or have other macromers should include these in generation of their calibration curve, as it is important to establish both linearity and the amount of fluorescence that can be expected in the target nanoparticles.

Note: A calculation for the dynamic range can be completed by determining the target loading of your DNA into the SPNP. For example, ours is 4.5 m/m% of the SPNP, so to generate the calibration curve, I used an amount of DNA that corresponds to between 0.4 % and 7.5 % m/m.

Note: The amount of HSA and PEI in the samples used to generate the calibration curve is held constant, as the amount of PEI is varied across formulations and HSA is expected to be the complicating macromer in the solution. This allowed us to say with confidence that a linear calibration curve for the fluorescent DNA (here, Cy3-DNA) can be established regardless of protein components within the solution. This also allowed us to say that if there was a deviation from measurement of Cy3-DNA present once the particles had been crosslinked, it was due to a scattering effect owing to nanoparticle formation or otherwise from encapsulation of the Cy3-DNA within the SPNP.

Note: I included a formulation both with and without PEI present so that the reader can test whether there is a difference in slopes for their anticipated fluorophore. I include ***Figure 3-1*** *showing the change of slopes here, but both are highly linear ($r^2 > 0.9$) and repeatable (n = 3 for each).*

Note: Now that the BP per dye for your Cy3-DNA is known, this is used to dilute the sample to 500 BP/dye by cutting the Cy3-DNA with 1 mg/mL pDNA in water.

This diluted Cy3-DNA is used for the remainder of the calibration curve generation and any in vitro studies.

Note: I use 100 µL of each sample as this allows for full coverage of the bottom of the well in a 96-well plate without approaching the maximum volume of each well.

Note: The plate reader was chosen over a fluorimeter to enable ease of access to this method for life scientists who have access to and regularly utilize a plate reader.

*Note: An example formulation for the calibration curve that I generated is found at in **Table 3-2**.*

1. Each sample is prepared per **Table 3-2** in PCR tubes.

   Note: You don't need to use PCR tubes, I find it useful because of the small sample size.

2. The water is added first, then the diluted Cy3-DNA is added.

   Note: The order of addition is important, and you will get different results if you don't follow it. I've tested it, and you will get a different curve that will not be representative of the particles, as the order of addition is different.

   Note: Pre-mix all solutions separately (HSA + HSA405, DNA at 500 bp/dye, etc.) then follow the established order of addition: water, DNA, PEI, HSA.

3. PEI is added next, and the solutions are vortexed for 5 seconds then incubated at room temperature for 30 minutes.

(A)

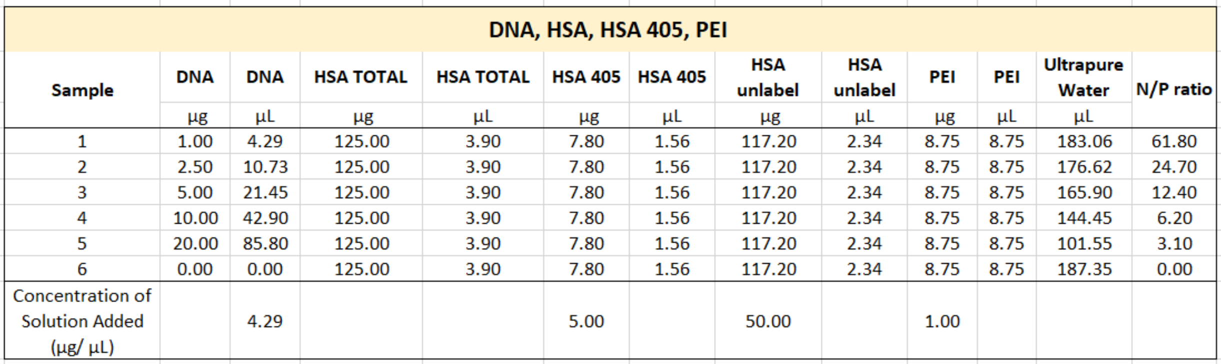

DNA, HSA, HSA 405, PEI

Sample	DNA	DNA	HSA TOTAL	HSA TOTAL	HSA 405	HSA 405	HSA unlabel	HSA unlabel	PEI	PEI	Ultrapure Water	N/P ratio
	µg	µL	µg	µL	µg	µL	µg	µL	µg	µL	µL	
1	1.00	4.29	125.00	3.90	7.80	1.56	117.20	2.34	8.75	8.75	183.06	61.80
2	2.50	10.73	125.00	3.90	7.80	1.56	117.20	2.34	8.75	8.75	176.62	24.70
3	5.00	21.45	125.00	3.90	7.80	1.56	117.20	2.34	8.75	8.75	165.90	12.40
4	10.00	42.90	125.00	3.90	7.80	1.56	117.20	2.34	8.75	8.75	144.45	6.20
5	20.00	85.80	125.00	3.90	7.80	1.56	117.20	2.34	8.75	8.75	101.55	3.10
6	0.00	0.00	125.00	3.90	7.80	1.56	117.20	2.34	8.75	8.75	187.35	0.00
Concentration of Solution Added (µg/ µL)		4.29			5.00		50.00		1.00			

(B)

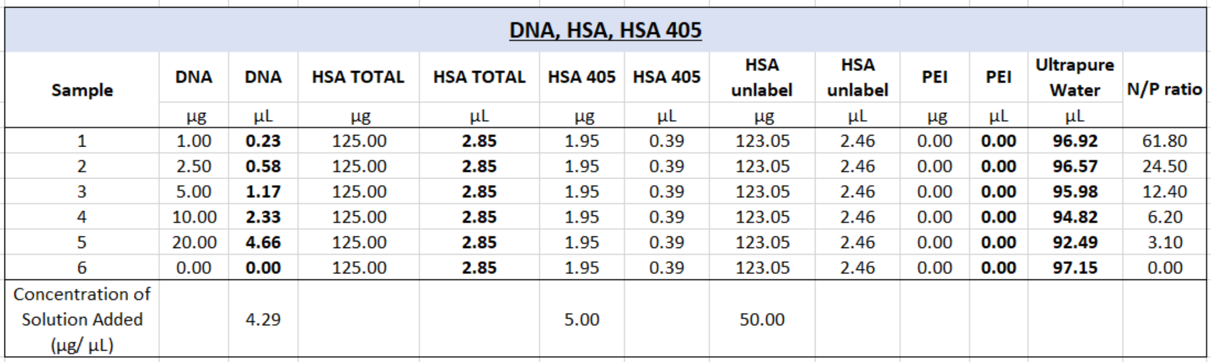

DNA, HSA, HSA 405

Sample	DNA	DNA	HSA TOTAL	HSA TOTAL	HSA 405	HSA 405	HSA unlabel	HSA unlabel	PEI	PEI	Ultrapure Water	N/P ratio
	µg	µL	µg	µL	µg	µL	µg	µL	µg	µL	µL	
1	1.00	**0.23**	125.00	**2.85**	1.95	0.39	123.05	2.46	0.00	**0.00**	**96.92**	61.80
2	2.50	**0.58**	125.00	**2.85**	1.95	0.39	123.05	2.46	0.00	**0.00**	**96.57**	24.50
3	5.00	**1.17**	125.00	**2.85**	1.95	0.39	123.05	2.46	0.00	**0.00**	**95.98**	12.40
4	10.00	**2.33**	125.00	**2.85**	1.95	0.39	123.05	2.46	0.00	**0.00**	**94.82**	6.20
5	20.00	**4.66**	125.00	**2.85**	1.95	0.39	123.05	2.46	0.00	**0.00**	**92.49**	3.10
6	0.00	**0.00**	125.00	**2.85**	1.95	0.39	123.05	2.46	0.00	**0.00**	**97.15**	0.00
Concentration of Solution Added (µg/ µL)		4.29			5.00		50.00					

Table 3-2. The formulas for generation of the calibration curve presented in the previous chapter and used for calculation of SPNP loadings (Chapter 2). (A) with PEI present (B) without PEI present.

4. The solutions are vortexed again for 2-3 seconds, then the calculated amount of HSA is added to each solution mixed well by vortex again for 2-3 seconds.
5. The samples are then loaded one per well into a black-walled 96-well plate with a clear polystyrene bottom.

   Note: I never use the wells on the perimeter of a 96-well plate, as they can suffer from evaporation and change solution volumes.
6. Using the SpectraMax m5 plate reader, fluorescent measurements are taken from 550-700 nm with a step size of 5 nm, excitation 495 nm, Cutoff Filter 530 nm.

Note: These values are chosen to encompass the peak maxima of Cy3, and the cutoff filter is chosen to eliminate the Ramen signal obtained from the presence of water in the system. The reader can change these settings to a wavelength range suitable for their fluorophore, but the same conditions must be used when analyzing the fluorescence of any product.

7. The fluorescent intensity of the Cy3-DNA at the peak maxima wavelength (575 nm) is used to generate a calibration curve for Cy3-DNA emission at the peak intensity by graphing the amount of dye (µM) vs. the fluorescence (a.u.) at each point.

   Note: I have prepared graphs that report dye concentration (µM) vs. the fluorescence signal read from the plate reader (a.u.). To do so, convert from mass of DNA added per ***Table 3-2****, then use the molecular weight of your nucleotide to concert to moles, then moles of BP (depending on your nucleotide's formulation). Next use the molecular weight of your dye and the known dilution of bp/dye (here 500 bp/dye) to convert to mol of dye, then your known volume (here, 100 µL) to convert to molarity of the dye.*

   Note: You can graph a.u. as a function of mols of dye or µM dye, the curve will be similar (linearity, not scale) just be sure to use the correct equation when calculating how much DNA present in your particles later.

8. The amount of DNA (µM) can be easily calculated from the known amount of Cy3-DNA at each point in the curve by converting the known molar amount of Cy3 per BP to Cy3 per DNA and then total DNA mass to molarity.

Note: If it is not provided by the manufacturer, an approximation of the plasmid molecular weight can be obtained by using the equation found on the ThermoFisher website: [https://www.thermofisher.com/us/en/home/references/ambion-tech-support/rna-tools-and-calculators/dna-and-rna-molecular-weights-and-conversions.html]

9. Then, the equation for the calibration curve is established using a linear regression and the goodness of the fit is analyzed using the r^2 values calculated upon linear regression in GraphPad Prism v.9.2.0.

   Note: Once calculated (µM dye or mol dye), the values can be entered into Prism, but you cannot calculate in Prism. If you want to use Origin Lab, you can do it in there, but I use Prism here.

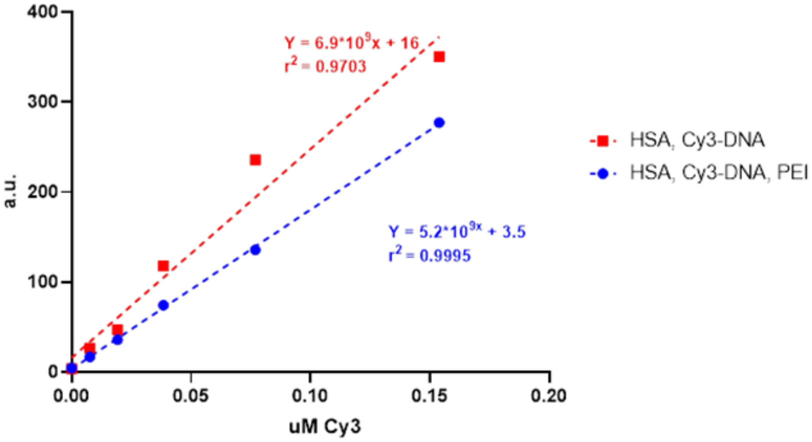

Figure 3-1. Calibration curves generated by the formulations in Table 3-2. The decrease in the slope upon addition of PEI is 32% but the linearity remains high (both r2 > 0.97) and the p-value for the slopes of the lines is p = 0.0277, meaning there would be a 2. 77% change of randomly choosing a data point, and therefore we can conclude that the slopes are significantly different.

10. Three samples were prepared and measured in triplicate at each point and the line of best fit equations were found to exist within a 95% confidence interval (CI) of each other so they can be described by a single linear equation, which was utilized as the calibration curve equation in subsequent steps.

    Note: Again, the linear regression and determination of a 95% CI was done in Prism once the µM dye had been established in Excel.

    Note: The final calibration curve graphs are reported in Chapter 2.

3.6 Preparation of Cy3-DNA Loaded Synthetic Protein Nanoparticles

SPNPs with a Cy3-DNA payload were prepared by electrohydrodynamic (EHD) jetting as described in Chapter 2. Once the previous steps have been taken to calculate the degree of labeling for Cy3-DNA (dye per DNA), the resultant conjugation product is diluted with unlabeled DNA to a dye per BP concentration of 1:1000. This mixture is used in SPNP fabrication. This ratio was established based on preliminary cell studies where a variety of dye to BP concentration were examined from 1:500 – 1:2500. HepG2 cells were transfected using Lipofectamine and identical amounts of DNA. The chosen concentration, 1:1000, was the highest ratio at which confocal microscopy could clearly capture of Cy3 and GFP resulting from DNA expression at 48 hours after treatment (**Figure 3-2**).

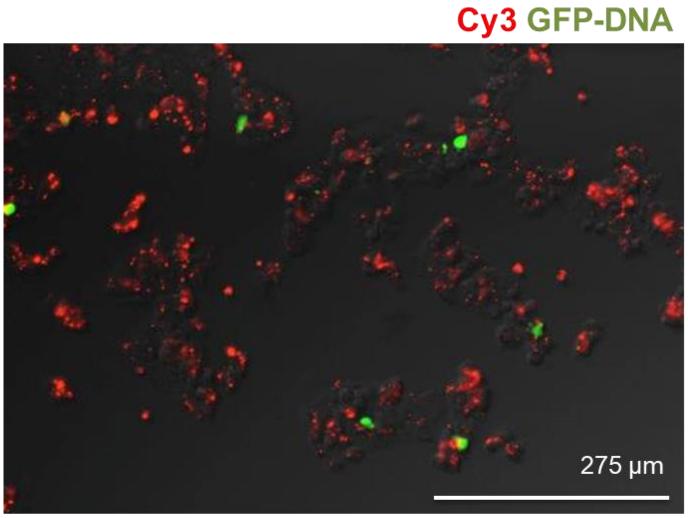

Courtesy of Yao Yao

Figure 3-2. The chosen ratio of 1 dye per 1000 base pairs was tested in HepG2 cells using Lipofectamine and the resultant Cy3 and GFP expression can be clearly imaged using confocal at t = 48 hours. This image was captured by Yao Yao and is included to strengthen the explanation given here.

Note: Be sure to calculate the weighted concentration of DNA for use in the formulations, as it is very likely different from the 1 mg/mL that the unlabeled DNA is already at. You can generate the concentration of DNA in the Cy3-DNA using the nanodrop attachment of the SpectraMax m5 as described above or with a traditional nanodrop instrument, but knowing the concentration is vital to using the proper amount of DNA solution in SPNP formulation.

1. A representative 4.5 m/m% DNA SPNP is presented in **Figure 3-3**.
2. Dilute the Cy3-DNA generated from the conjugation reaction to the desired BPs per dye ratio and calculate the concentration of the resulting solution.

(A)

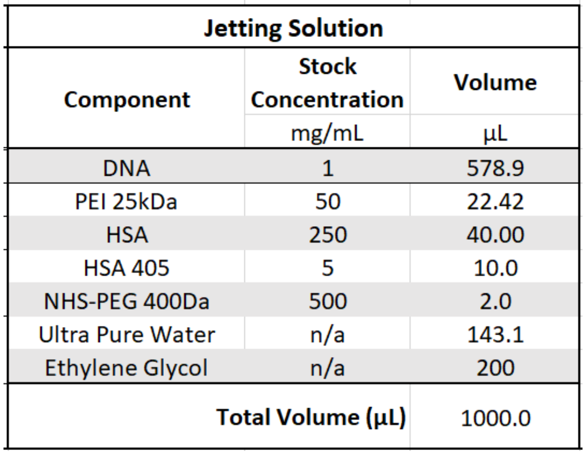

Jetting Solution		
Component	Stock Concentration	Volume
	mg/mL	µL
DNA	1	578.9
PEI 25kDa	50	22.42
HSA	250	40.00
HSA 405	5	10.0
NHS-PEG 400Da	500	2.0
Ultra Pure Water	n/a	143.1
Ethylene Glycol	n/a	200
	Total Volume (µL)	1000.0

(B)

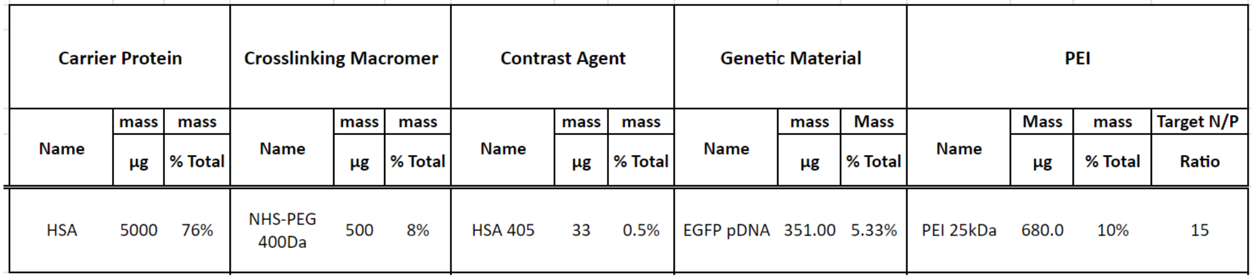

Carrier Protein			Crosslinking Macromer			Contrast Agent			Genetic Material			PEI			
Name	mass	mass	Name	mass	mass	Name	mass	mass	Name	mass	Mass	Name	Mass	mass	Target N/P
	µg	% Total		µg	% Total		µg	% Total		µg	% Total		µg	% Total	Ratio
HSA	5000	76%	NHS-PEG 400Da	500	8%	HSA 405	33	0.5%	EGFP pDNA	351.00	5.33%	PEI 25kDa	680.0	10%	15

Figure 3-3. Formulation of a 4.5 m/m% DNA loaded SPNP. (A) Jetting Solution for a 1.0 mL SPNP prep. (B) The resulting formulation in SPNP.

Note: All preparation of SPNPs in the lab is done based on the volume used, so it is important to account for changes in density that may result from addition of even a small amount of the Cy3-DNA solution.

Note: It is necessary to utilize the same order of addition used to generate the calibration curve. The established order of addition: water, DNA, PEI, HSA.

3. Add 80:20 vol% of water-to-ethylene glycol solution to a microcentrifuge tube.
4. Add the Cy3-DNA to the solvent solution.
5. Add the PEI to the solution. Incubate the Cy3-DNA mixture and PEI at room temperature for 30 minutes.

*Note: The formulation I use for a 4.4 m/m % loading of DNA in SPNP is listed in **Table 3-3** below.*

6. Protein solutions were prepared by addition of DNA/PEI, 10% w/w NHS-PEG-NHS crosslinker, 1% w/v HSA, and 0.5% w/v HSA-405 to the solvent system. The solution was pumped using a syringe pump at 2.0 mL $hr^{-1.}$ Once a droplet formed on the end of the needle, an electric field (5 kV) was applied to obtain the characteristic Taylor Cone. Due to the voltage applied, the solution was atomized and pulled towards the grounded plate 20 cm away, resulting in electrospray of particles. The resultant sPNPs were then allowed to crosslink for 7 days in a 37°C incubator before being collected using an established protocol.[26]

3.7 Determination of Cy3-DNA Percent Loading in Synthetic Protein Nanoparticles

Gravimetric analysis and fluorescence readings are used together to assess the amount of Cy3-pDNA loaded into crosslinked sPNPs. The sPNPs are prepared and collected according to the established protocol described above. The final step of this protocol requires a 1-hour centrifugation to collect the product in the pelleted form. For gravimetric analysis, the pellet is obtained, the supernatant is removed, and the pellet is covered in 200 µL of Milli-Q water for 2 minutes then removed. This is repeated once more, then the washed pellet is lyophilized overnight to ensure that any residual water is removed from the sample.

The lyophilized pellet is then weighed gravimetrically using a Thermogravimetric Analyzer (TGA) instrument. This mass is recorded and used for calculations of Cy3-pDNA loading and dosing for cells. The lyophilized product is resuspended in 1x PBS to a concentration of 1 µg/µL, the concentration is used for *in vitro* dosing. 100 µL of this sample is used for fluorescence measurements and the required amount to total 100ng per sample in a 96-well plate is used for cell work and assessment via flow cytometry.

A fluorescent sweep of the sPNP solution was performed with the same excitation, cutoff filter, and step size as the calibration curve. A black walled 96-well plate is again used, and the volume is held constant for these measurements (100 µL), consistent with the volume used in generating the calibration curve. The fluorescent intensity values (a.u.) obtained at 575nm are then used to calculate the amount of Cy3, and therefore Cy3-DNA present in the solution using the equations described above for generation of the calibration curve. The amount of Cy3-DNA put into the preparation mixture was taken as 100% and the average actual loading vs. target loading. This was determined by calculating the concentration of DNA measured by the plate reader at 575 nm and comparing it to the known input amount **Equations 3-(6-10). Equation 3-6** is obtained from a linear fit of the points generated with the calibration curve and solved for x, which is the amount of dye in the solution (µM). This value is then used to calculate the µM of BP in the solution (**Equation 3-7**) where BP per DNA is the value established earlier for jetting and will be known. µM BP is converted to M of DNA using **Equation 3-8** and finally the g/L DNA in the solution is calculated using **Equation 3-9**. In **Equation 3-10** the mass of HSA is obtained from gravimetric analysis and the known volume of solution measured to obtain the concentration, then the DNA and HSA concentrations are simply divided to arrive at actual loading percent.

$$a.u._{575} = mx + b \tag{6}$$

$$Base\ Pair\ (uM) = \ x * (Base\ Pair\ per\ DNA) \tag{7}$$

$$DNA\ (M) = \frac{Base\ Pair\ (uM)}{Base\ Pair\ per\ DNA * 10^6} \tag{8}$$

$$DNA\ \left(\frac{g}{L}\right) = DNA\ (M) * \ DNA_{Molecular\ Weight} \tag{9}$$

$$Actual\ Loading\ \% = \ 100 * \frac{DNA\ \left(\frac{g}{L}\right)}{HSA\ (\frac{g}{L})} \tag{10}$$

Equation 3-(6-10). Equations used to calculate the actual loading of pDNA into Cy3-SPNPs

3.8 Determination of Particle and Payload Distributions

Now, using the actual loading obtained from the PBL strategy, this information can be used in combination with particle size distribution data to obtain both particle and pDNA payload distributions. First, the particle size distribution of the SPNPs is obtained using dynamic light scattering (DLS) and the number average sizes are used in the work (nDLS). The nDLS spectrum is then used to calculate the plasmid per particle at each size bin measured by nDLS using **Equations 3-(11-18)**. The raw nDLS spectrum is given in percent of total and is not normalized. This is converted to counts per bin (**Equation 3-11**) and then the volume of spheres with that diameter is calculated (**Equation 3-12**). From there, the mass of the SPNP in that bin can be calculated with an assumed density of HSA (**Equation 3-13**).[110]

$$Count = \frac{Percent_{nDLS}}{Percent\ of\ Total} \tag{11}$$

$$V = \frac{4}{3}\pi\left(\frac{d}{2}\right)^3 \tag{12}$$

$$m_{SPNP} = V\rho_{HSA} \tag{13}$$

$$m_{DNA} = Actual\ Loading\ \% * \ m_{SPNP} \tag{14}$$

$$\frac{plasmid}{SPNP} = \frac{m_{DNA} * 6.02 * 10^{23}}{DNA_{Molecular\ Weight}} \tag{15}$$

$$\frac{plasmid}{bin} = Count * \frac{plasmid}{SPNP} \tag{16}$$

$$Diameter_{\ Average\ SPNP} = \frac{\left[\sum_{i=0.4}^{Bin\ max}(Diameter_{Bin})_i * Count_i\right]}{\sum_{i=0.4}^{Bin\ max} Count_i} \tag{17}$$

$$\frac{Plasmid}{particle} = \frac{\left[\sum_{i=0.4}^{Bin\ max}\left(\frac{plasmid}{bin}\right)_i * Count_i\right]}{\sum_{i=0.4}^{Bin\ max} Count_i} \tag{18}$$

Equations 3-(11-18). Equations used to calculate the particle and pDNA distribution within a SPNP population

The mass of DNA is then calculated with **Equation 3-14**, and this is used to calculate the number of plasmids per SPNP within a given bin (**Equation 3-15**). These values are used to generate heat maps of particle population distribution for various SPNP populations as well as the average number of plasmids per particle within various populations.

This can also be expressed as plasmids per bin (**Equation 3-16**). Finally, the diameter of the number average SPNP can be calculated using **Equation 3-17**. The average plasmid per particle can also be obtained (**Equation 3-18**). Identical calculations are done for SPNPs with a diameter of 150 nm, which are reported in Chapter 2. These calculations can be used both either target (input) pDNA within the solution and the observed pDNA measured via the PBL strategy. In this way, comparisons between the target and observed SPNP loading can be made. Graphs comparing the two are presented in Chapter 2 along with fitting of various lines to these data to yield more information.

This works stands as a guide for researchers to use and adapt these methods in whole or in part, to new systems so that the whole community has access to efficient workflows to quantify gene delivery vehicles with confidence.

Chapter 4

Structure Function Relationships Between Synthetic Protein Nanoparticle Composition and Reporter Gene Expression

The material in this chapter has been adapted with minor modifications from the following article:

1. L. Saunders, A. Mauser, N. Habibi, J. Gregory, J. Raymond, J. Lahann. “Rational Design of Synthetic Protein Nanoparticles for Gene Delivery”, *in preparation*.

4.1 Introduction

This work presents a rational design strategy for development of plasmid DNA-loaded synthetic protein nanoparticle (SPNP) gene delivery systems. Currently, there are no SPNP systems capable of DNA delivery, despite the success of using the platform for siRNA delivery *in vitro* and in organismal studies.[32,33,111] To develop a system capable of delivering DNA for gene therapy purposes, a foundational understanding of how SPNP composition affects gene expression is needed.

While hundreds of examples of DNA delivery vehicles exist in the literature, there are several components common across engineered delivery systems.[6,112] Polyethylenimine (PEI) content, a nuclear localization signal (SV40), and plasmid DNA (pDNA) dose are components that are considered to be some of the most important ones.[113,114] Effective engineered nanoparticles for gene delivery are often engineered using a common workflow.[115] First, many NPs are prepared with diverse formulations. Next, these NPs are tested *in vitro* for their ability to induce the desired biological changes. While this approach is common, it is time consuming and inefficient. Therefore, it is necessary to develop a rational design approach to optimizing NPs for pDNA delivery that is capable of efficiently scanning a diverse design space. The work presented here is a step in that direction and can be easily built upon and adapted in subsequent studies, making this platform readily adaptable to various potential applications that are detailed in Chapter 6.

This SPNP pDNA delivery platform represents a plug and play technology that can be widely applied. The rational design strategy outlines clear and straightforward methods for assessing changes to SPNP formulation on biological outputs for future applications. Taken together, both a pDNA delivery platform and a streamlined workflow for assessing and tailoring said platform to certain disease states and applications is presented here.

4.2 Background and Motivation

4.2.1 Introduction to Synthetic Protein Nanoparticles for Gene Delivery

Nanoparticles hold great promise for gene delivery and have been heavily investigated as alternatives to virus-based gene delivery vehicles. There are several different material classes commonly used in fabrication of non-viral nanoparticles for gene delivery such as inorganic nanoparticles[116–119], lipid vectors[15,80], polymeric nanoparticles[103,120], and protein nanoparticles.[32,38,121]

Synthetic protein nanoparticles (SPNPs) are formed using the established technique of electrohydrodynamic (EHD) jetting which is explained in detail in Chapter

1.[26,122] SPNPs prepared by EHD jetting have numerous favorable properties, including high uniformity and high circularity across a particle population. Furthermore, the modularity of EHD jetting enables the ability to tune parameters to achieve particle sizes that are desirable for their intended system,[123] and vary the protein solution that is loaded into the syringe.

SPNP components are carefully chosen to endow the SPNPs with specific qualities. SPNPs are prepared using a bulk protein and crosslinked via an NHS-PEG-NHS ester to form stable nanogel particles.[124] The pDNA payload is electrostatically complexed with a cationic moiety, here polyethyleneimine (PEI) to protect and condense the pDNA. A cationic nuclear localization signal (SV40) is also electrostatically complexed to the pDNA prior to the addition of PEI to aid in its incorporation into the SPNP.

Additional design considerations affect the SPNPs function. For example, benefits of using human serum albumin (HSA) as the bulk material for SPNPs include high stability and solubility in aqueous solutions, favorable drug loading capacity, and high biocompatibility and biodegradability in mammalian cells and organismal studies.[37,125] Albumin has also been used in many gene delivery applications in combination with polyethyleneimine (PEI) and other cationic macromers.[39,126,127]

4.2.2 Considerations for Synthetic Protein Nanoparticles Formulation for DNA Delivery

The complexation and delivery of the pDNA must be accounted for in planning for the inclusion of certain moieties and the design space. PEI is a cationic, branched polymer that is critical for electrostatic complexation with the anionic pDNA and is hypothesized to play an important role in intracellular delivery of the pDNA payload.[57,128] Following cellular uptake via an endocytic pathway, the SPNP is trapped within the endosome, which acidifies as it ages, eventually developing into a lysosome, at which point the contents of the endosome will be degraded.[57] It is therefore necessary for nanoparticles that are endocytosed to escape the endosome to achieve downstream effects. Since PEI is a cationic polymer with primary and tertiary amines and a pKa of 7.1, the amine groups on the PEI become positively charged upon entry to the endosome due to the increasing acidification below physiological pH.[129] This attracts water molecules and causes osmotic swelling of the endosome, leading to rupture and subsequent release of endosomal cargo into the cytosol. This cascade of events is termed the proton sponge hypothesis, and is the accepted mechanism for endosomal escape of PEI-containing nanoparticles.[58] For these reasons, PEI is included within the formulation of pDNA-loaded SPNPs.

A common issue with non-viral DNA delivery systems is low efficiency resulting from the many intracellular barriers DNA must overcome prior to having its intended effect. To have a therapeutic effect, DNA must not only enter the cell and escape the endosome, it needs to further be transported into the nucleus.[68] The nuclear membrane represents a formidable barrier to effective DNA delivery, as active transport across the membrane through a nuclear pore complex or during mitotic disassembly of the nuclear membrane is necessary.[65] This feat is accomplished through either exploiting the breakdown of the nuclear membrane during cell division or incorporating nuclear localization signals (NLS) in the gene delivery vehicle.[130] Traditionally, NLS are derived from viruses, as they evolved to efficiently transfect mammalian cells and can therefore enter the nucleus at a high rate.[131] Improvement of non-viral DNA delivery systems has been seen upon inclusion of NLS proteins and peptides.[69,132] Here, SV40, a NLS peptide derived from the simian virus, will be included in the SPNPs to increase nuclear uptake.

Numerous considerations in the formulation of SPNPs for pDNA delivery, including the bulk material, the pDNA complexing macromer, and additional moieties to assist in exploiting the biology of the target cells, affect the efficacy of gene delivery of the SPNPs. In this work, three components (PEI content (N/P), SV40 content, and pDNA loading) were varied and SPNPs were prepared with different compositions. The diverse set of SPNPs were assessed using the biological outputs that they produce in HepG2 cells, such as the viability of the cells, percentage of particle positive cells (uptake), and the percentage of cells that express the reporter gene (GFP). These biological outputs were quantified using flow cytometry. The various formulations of SPNPs reported here were then examined based on their biological outputs to characterize the structure function relationships between changes in SPNP design changes and reporter gene expression.

4.3 Methods

4.3.1 Determination of DNA Viability – Restriction Enzyme Digestion Assays

To investigate the effects of EHD jetting on plasmid DNA, pCMV-GFP pDNA solutions were jetted at voltages concomitant with EHD jetting of HSA SPNPs that achieve the characteristic Taylor Cone (10-12 kV). Identical DNA solutions were prepared at 50 w/v% in PBS, the same concentration of DNA in the 4.4 m/m% DNA/SPNP formulations. These samples were then either subjected to tip sonication for 1 minute at an amplitude of 5, incubated with HSA at room temperature for 30 minutes, or jetted in

PBS alone. The resultant jetted solutions were collected and subjected to a restriction enzyme digestion to assess the viability of jetted DNA.

The resultant pDNA solutions were assessed using UV-Vis for DNA content, and then digested with an appropriate amount of restriction enzyme (Blpl or Nsil) according to manufacturer instructions. This reaction was carried out per manufacturer instructions in 1x NEBuffer and using 5 units of enzyme per µg of DNA for a 1-hour digestion. The resultant products were run on a standard 1% agarose gel and run at 100V for 30 minutes prior to visualization under a UV lamp.

4.3.2 Determination of N/P Ratio – Gel Shift Assays

The N/P ratio was calculated using **Equation 4-1** and samples were prepared that spanned a dynamic range of N/P = 0 to 30. A standard 1% agarose gel was prepared and loaded with the samples listed in the table below. The gel was run for 30 minutes at 100 V and then visualized under a UV lamp.

4.3.3 Preparation of Synthetic Protein Nanoparticles

SPNPs were prepared by the established electrohydrodynamic (EHD) jetting method. First, the GFP pDNA and SV40 peptide were incubated together at room temperature for 30 minutes at the desired molar ratio. Next, this mixture was added to the required amount of polyethyleneimine (PEI) to achieve the target nitrogen to phosphorous (N/P) ratio and incubated at room temperature for 30 minutes. For the solvent, 80:20 by volume of water-to-ethylene glycol ratio was used. Protein solutions were prepared by addition of 4.5 w/w% DNA per SPNP, 10% w/w NHS-PEG-NHS crosslinker, 1% w/v HSA, and 0.5% w/v HSA-405 to the solvent system. The solution was pumped using a syringe pump at 2.0 mL hr^{-1}. Once a droplet formed on the end of the needle, an electric field (10-12 kV) was applied to obtain the characteristic Taylor Cone indicating that the electrospray of the protein solution was stable. The resultant SPNPs then crosslinked for 7 days in a 37°C incubator before being collected in phosphate-buffered saline (PBS), followed by serial centrifugation to obtain SPNP sizes of less than 250 nm.

4.3.4 Synthetic Protein Nanoparticle Uptake and Expression in HepG2 Cells

Internalization of fluorescent SPNPs loaded with DNA by HepG2s was visualized using confocal microscopy and quantified using flow cytometry. Fluorescent SPNPs were obtained by addition of Alexa Fluor 405 conjugated to HSA (HSA-405) at 5 mg mL^{-1} to the solvent mixture for electrospraying of SPNPs.

For this study, HepG2 cells were maintained in a humidified incubator at 37°C and 5% CO_2. Flow cytometry was used for quantitative uptake, viability, and reporter gene expression studies. HepG2s were plated in a 96-well plate at a density of 18,000 cell per well in EMEM media with 10 v/v% FBS. After 24 h, media was removed from the wells and wells were washed once each with serum-free EMEM. Fresh serum-free media with 1% v/v Penicillin-Streptomycin containing the SPNP groups at 100ng DNA per well or Lipofectamine 2000 with various amounts of DNA was added to each well. Groups treated with Lipofectamine were incubated for 4h, then washed once with EMEM and 100uL of EMEM + 10% v/v FBS was added to each well. After 24-hour incubation of cells with SPNPs, the cells were washed once with EMEM and then 50uL of 0.25% Trypsin was added to each well. The cells were trypsinized in the incubator for 3 min at 37°C, then removed from each well and added FACS buffer. Cells were centrifuged at 300 G for 4 minutes and washed and spun down once more. The cells were resuspended in 1mL FACS buffer and stained with SYTOX red before analyzing them via flow cytometry using a CytoFLEX cell analyzer at the Flow Cytometry Core of the University of Michigan. Data were analyzed using FlowJo software.

4.3.5 Characterization of Synthetic Protein Nanoparticles by Number Average Dynamic Light Scattering (nDLS)

A Zetasizer Nano ZS (Malvern Panalytical) was used to carry out DLS measurements. Following collection of SPNPs, the particle size distribution in was measured at room temperature in 1x PBS. Three individual measurements were carried out per sample and averaged to determine SPNP size. Number average DLS (nDLS) data was extracted from the intensity DLS (iDLS) measurements reported by the instrument and used for reporting of diameters.

4.3.6 Analysis Software

Microsoft Excel 2020 was used for all data manipulation and for the general summary of statistics. GraphPad Prism v9.2.0 was used for presentation of graphs and fitting of linear calibration curves.

4.4 Results and Discussion

To establish the bounds of the design space to be tested, a literature search was conducted to establish biologically relevant ranges for SV40 peptide content.[69] N/P ratio (PEI content) is established using experimental methods described here. The range of these parameters must be wide enough to encompass any changes to the biological outputs.

The range of PEI (N/P) content for SPNP preparation was established via a gel shift assay. A GFP reporter pDNA of 3487 bp was used in this work, and the amount of PEI needed to fully complex with it was established using this technique. The gel shift assay is a common electrophoretic technique used to study PEI-DNA interactions. Briefly, cationic PEI and anionic pDNA were mixed at various nitrogen to phosphate (N/P) ratios and loaded onto an agarose gel (**Appendix B**). An electric field was then applied and charged molecules migrated through the gel. If a band was visible running towards the positive end of the cell, then the anionic pDNA had not been fully complexed with the PEI. If there was no band visible, then the PEI and pDNA have fully complexed. Here, by N/P = 3 there was no band present and so a complex had been formed (**Figure 4-1a**). Therefore, this was the minimum N/P used and the maximum bound is set at N/P = 20 for this iteration of experiments.

$$N/P\ Ratio = \frac{(Y\ g\ PEI)\ *(1\ mol\ PEI)}{(X\ mol\ N)\ *(\frac{25,\ 000\ g}{1\ mol})} \qquad (1)$$

Equation 4-1. Calculation of the N/P ratio is done using this formula.

The range utilized for pDNA content was from 1 – 6 m/m% of the total SPNP. Upon further inspection of the SPNP system, a maximum value of 4.5 m/m% pDNA was established, as higher pDNA percentages induced precipitation of the solution used for SPNP formation. SPNPs of lower mass percentages pDNA were not used in transfection of HepG2 cells, as a pDNA loading with such low values would require a large amount of SPNP to be delivered and would not be efficient. SPNPs of 4.5 m/m % were prepared and their physicochemical properties were measured.

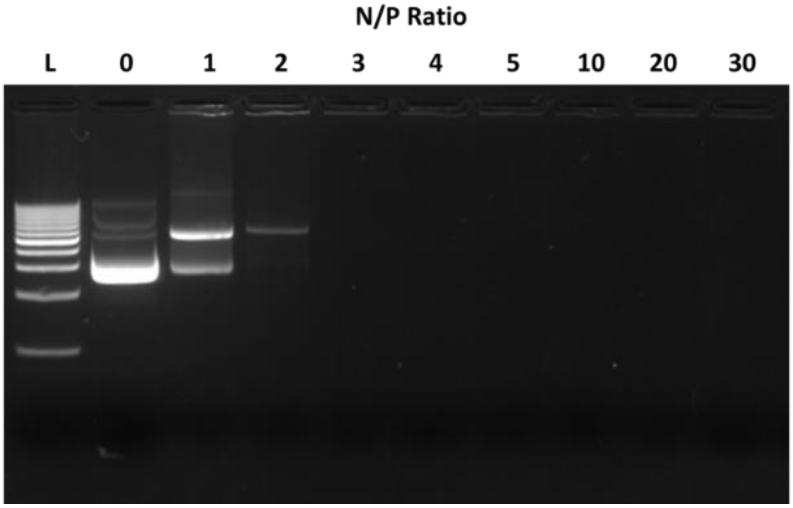

Figure 4-1. A standard gel shift assay is run on 1 v/v% agarose gel electrophoresis. By N/P = 3 no band is present indicating full complexation. N/P = 0 corresponds to naked pDNA.

A polymeric delivery system has been reported to have increased nuclear import and transfection efficiency upon inclusion of an SV40 peptide electrostatically bound to pDNA.[69] This methodology was the basis for experiments conducted here, and a similar molar ratio of 10:1 (SV40 to DNA) was used as the minimum bound with 100:1 set as the upper limit.

4.4.1 3D Design Space of Synthetic Protein Nanoparticles

The design space and workflow presented here enable efficient iteration over the entire parameter space and facile visualization of trends in biological outputs as a result of formulation changes. The design strategy presented here is inspired by statistical design of experiment (DoE) approaches but does not require the rigorous analysis necessitated by DoE, making this rational design approach easily adaptable by researchers.[133,134]

In this rational design approach, the three parameters of pDNA delivery systems, namely PEI (N/P ratio), SV40, and DNA Loading are defined. Each parameter was treated as an axis in a N-dimensional design space, which was here limited to the 3D space represented in **Figure 4-2a**. The bounds imposed on each axis in this design space are discussed in detail in subsequent sections. For the purposes of this work, the 3D design space was then restricted to 2D by fixing the SPNPs prepared at 4.5 m/m% DNA loading, removing the third axis. The SPNP formulations are also represented in **Figure 4-2b** as weight percent of total SPNP mass at various N/P ratios, as inclusion of an ionizable or cationic moiety is often reported as the most important parameter in the literature, but the optimal amount of PEI varies between reported delivery systems.[112,135]

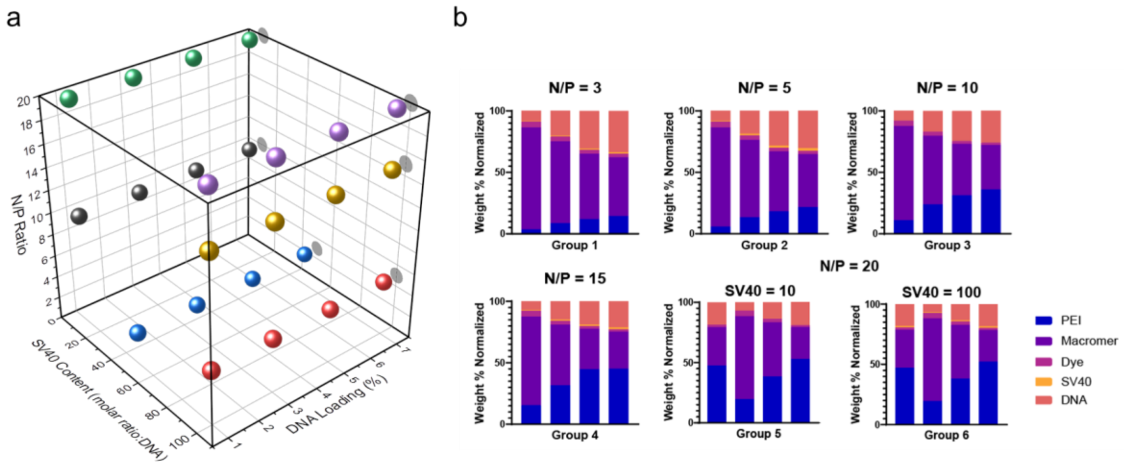

Figure 4-2. The design space of SPNPs reported in this chapter. (a) 3D representation of the SPNP design space with each axis corresponding to a parameter that was varied (N/P, pDNA amount, SV40 content). (b) bar charts corresponding to the normalized weight percent of each SPNP without HAS grouped by N/P ratio tested.

4.4.2 Physicochemical Analysis of SPNPs

As mentioned, a plane is taken of the 3D design space at a DNA loading percent at 4.5 m/m% so that the design space is now constrained to two dimensions (**Figure 4-3a**). The axes are now PEI content (N/P) (y-axis) which is varied from 0 - 20 and SV40 molar content (molar ratio of SV40:pDNA) (x-axis) which is varied from 0 - 100:1. The SPNPs designed and tested are graphed on these axes and described by their x and y coordinates. These same SPNP formulations are presented in bar charts where the weight percentage of each component is normalized to 100% of the overall SPNP weight (without HSA present) for easy visual inspection of each formulation (**Figure 4-3b**).

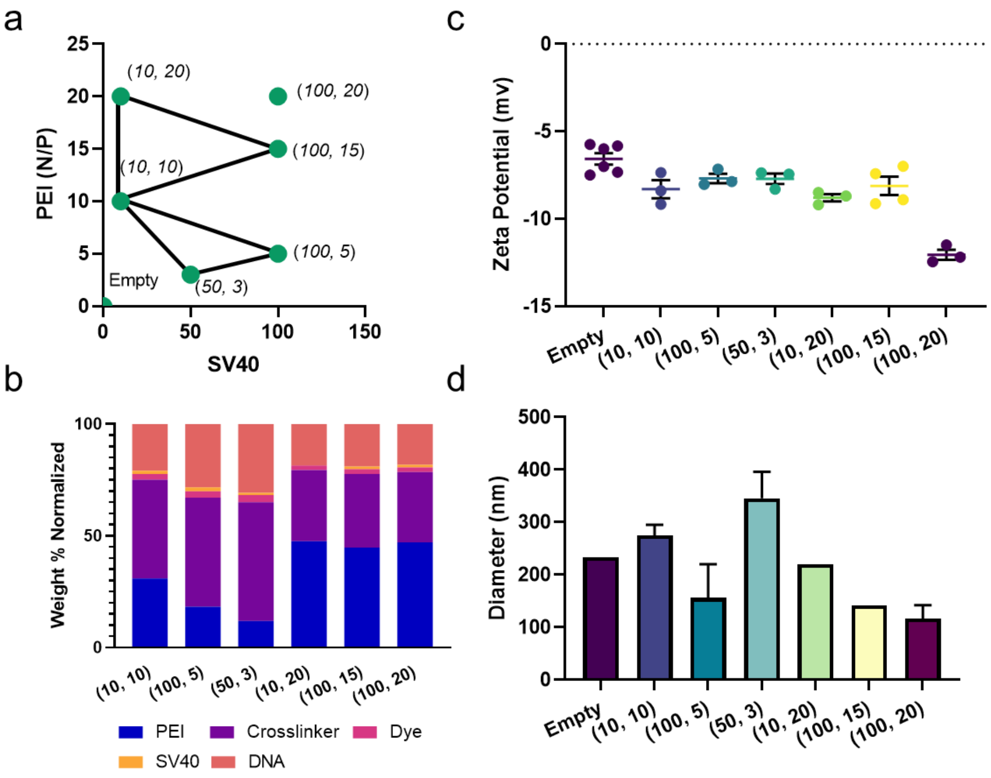

Figure 4-2. 2D design space and physicochemical analysis of SPNPs. (a) The 2D design space at 4.5 m/m% DNA/SPNP (b) Bar charts representing each of the SPNP formulations reported in subsequent steps. All values are weight % normalized to total SPNP without HSA present. (c) Surface charge of each SPNP as measured by zeta potential. (d) Diameter of each SPNP as measured by nDLS.

A representation of the HSA content for each SPNP tested is available for reference in **Appendix B.**

For each formulation, the impact of SPNP composition on physicochemical properties was assessed. The zeta potential of each SPNP is measured and the surface charge assessed (**Figure 4-3c**). All SPNPs prepared have a zeta potential ranging from -7 to -12 mV. The sizes of each SPNP are also assessed for any outliers or deviations from the expected size, as compared to the empty (no pDNA) SPNP. Here, number average dynamic light scattering (nDLS) is used to determine the mass average diameter of each SPNP (**Figure 4-3d**). These results indicate that stable SPNPs of expected size can be prepared across the chosen formulation space.

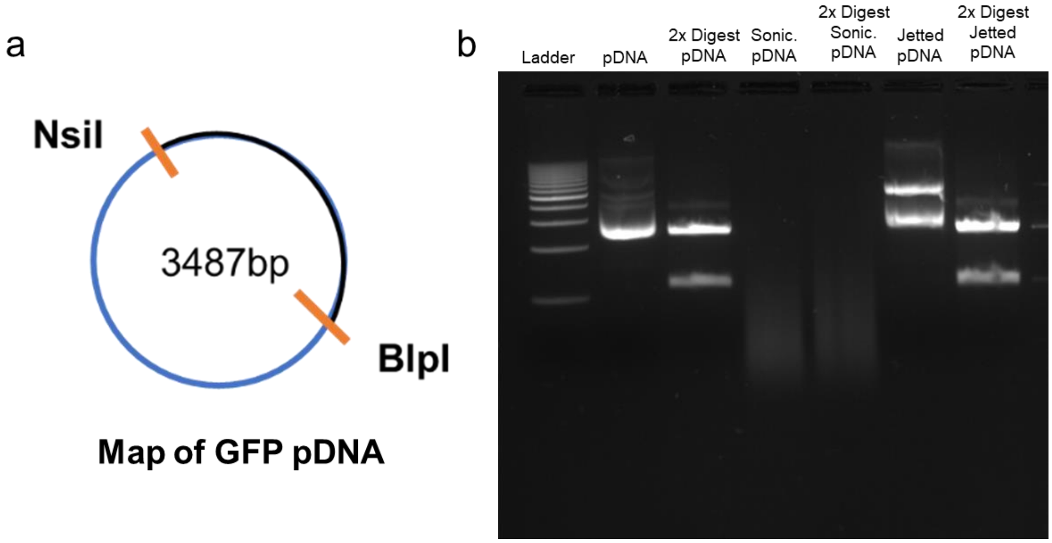

Figure 4-3. DNA stability following EHD jetting. (a) Schematic map of the pDNA examined here with the sites at which the restriction enzymes will cut the backbone marked in orange. (b) a standard agarose gel electrophoresis of al experimental and control groups was run. Importantly, the native and jetted pDNA appear similar, and the double digested pDNA and jetted digested pDNA also appear similar.

4.4.3 DNA Stability Following EHD Jetting

To ascertain whether the high voltage applied during the jetting process was damaging to the integrity of the pDNA, a double restriction enzyme digestion (RED) assay was conducted. The RED assay cuts the nucleotide at two predetermined sites on the backbone, resulting in two linear strands of pDNA (**Figure 4-4a**). A native pDNA was used as a negative control, whereas pDNA sheared by sonication (amplitude 5, t = 1 min) was used as the positive control. Jetted pDNA was run as a sample and subjected to degradation via the RED assay. All controls and experimental groups were run on a standard agarose gel and compared to each other. The native pDNA and jetted pDNA appear similar, and the double digested pDNA and jetted digested pDNA also appear similar (**Figure 4-4b**). This indicates that the integrity of the pDNA is not altered by EHD jetting. The stability of the pDNA is further confirmed by comparison between the sonicated/sheared pDNA and jetted pDNA, which looks markedly different than the jetted experimental group.

4.4.4 Effect of N/P and SV40 Content on Biological Outputs

The biological outputs examined are quantified using flow cytometry following transfection of HepG2 cells with the SPNPs and controls. The imaging scheme for SPNP preparation and measurement is presented in **Appendix B**. HepG2 cells are treated with Lipofectamine 2000 as a positive control and empty SPNPs as a negative control 48 hours prior to collection and measurement on a flow cytometer.

In the following bubble charts (**Figures 4-5, 4-6, and 4-7**), the axes are identical to the 2D design space presented earlier, with PEI (N/P) on the y-axis and SV40 content on the x-axis. The output of interest is included as a third variable, where the size of the bubble is positively correlated with the size of the biological output value. The legend next to each graph shows this correlation in further detail. The percent relative standard deviation (RSD %) is calculated based on the biological output pertaining to the specific figure, which is included as the bubble and its size varies depending on the value. RSD % is incorporated into the bubble charts as a color gradient to enable an understanding of the variability of the values to be visually inspected.

4.4.5 Impact of SV40 and PEI Content on Cell Viability

The viability of HepG2 cells treated with SPNPs and controls was measured at 48 hours after treatment on a flow cytometer (**Figure 4-5**). All SPNP treatment groups reported viabilities above 80%. There does not appear to be a strong relationship between incorporation of either SV40 or PEI content and the viability of the treated HepG2 cells. These uniformly high viabilities and the small spread, as measured by the standard error of the means (SEM) suggests that all SPNPs are tolerable to the cells.

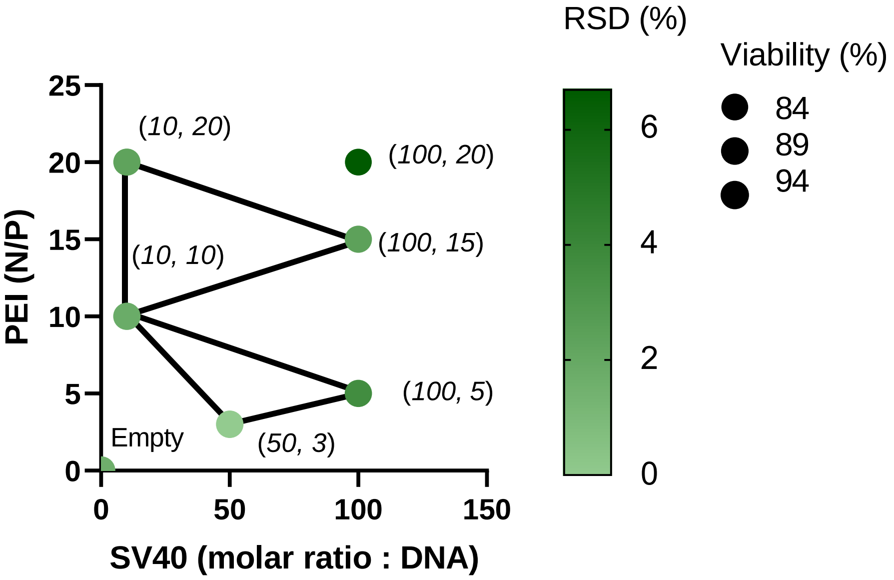

Figure 4-4.Viability of HepG2 cells (t = 48h) treated with SPNPs and controls as measured on a flow cytometer. The viabilities for each SPNP were above 80% and the small spread indicates that all treated groups tolerate the SPNPs well.

4.4.6 Impact of SV40 and PEI Content on Uptake of SPNPs

Uptake percentage is defined as the percentage of cells with particles as measured by a flow cytometer. Across the board, empty SPNPs with no pDNA content exhibit the highest uptake. The uptake between pDNA-loaded SPNPs varies widely. SPNPs exhibiting both the highest and lowest uptake have similar PEI content and identical SV40 content. This might indicate that neither N/P nor SV40 content are positively or negatively correlated to changes in uptake.

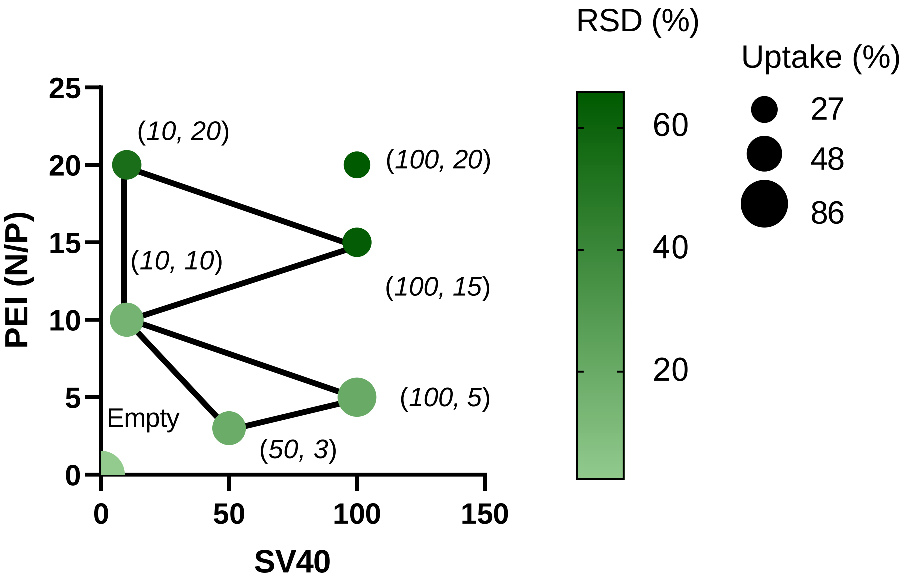

Figure 4-5. Uptake of SPNPs in HepG2 cells (t = 48h) treated with SPNPs and controls as measured on a flow cytometer. There does not appear to be a correlation between composition and uptake.

4.4.7 Impact of SV40 and N/P Ratio on Reporter Gene Expression

Here, a rational design strategy is used to arrive at the SPNP formulation that maximizes the percentage of cells expressing the reporter gene, GFP, as measured by flow cytometry. All SPNPs reported here contain 5 m/m% DNA to HSA content, equating to 4.5 m/m% of the total SPNP. The first three formulations of SPNP tested were (10, 10), (50, 3) and (100,5). Of these first three SPNPs, (10, 10) had the highest GFP expression, with (100, 5) trailing it. From these first three SPNPs tested, it is clear that formulations with higher PEI content exhibit higher GFP expression. This information was used to iterate on the formulations, and the next set of three SPNPs each increased PEI (N/P) content while maintaining the SV40 amounts used in the most successful formulations of the first set to arrive at (10, 10), (10, 20), and (100, 15). In this second set of experiments, (100, 15) exhibited the highest GFP expression. Now, the three SPNP formulations exhibiting the highest GFP expression are (10, 10) , (100, 15), and (10, 20). By visual inspection of **Figure 4-7**, it is clear that increasing N/P increases GFP expression. As such, the PEI content was increased, and SV40 was maintained to arrive at (100, 20). This SPNP (100, 20) exhibited the highest GFP expressing in HepG2 cells, as was expected. By simple visual inspection of the preceding SPNP formulations tested as graphed in **Figure 4-7**, the important biological output, GFP expression, could be optimized.

Graphing the biological outputs against the SPNP formulation enables quick interpretation of potential design rules and trends. As is seen in **Figure 4-7**, SPNPs with a higher N/P ratio result in a higher GFP expression. In general, higher amounts of PEI (higher N/P ratio) are predictive of higher GFP expression with a Pearson r = 0.91. The other parameter that is varied, SV40 incorporation, is not itself predictive of GFP expression (r = 0.42), but visual inspection reveals that for the same N/P ratio, an increase in SV40 increases reporter gene expression (**Figure 4-7**). This trend might have been overlooked if only statistics were considered, and a visual inspection of the parameter space was not conducted.

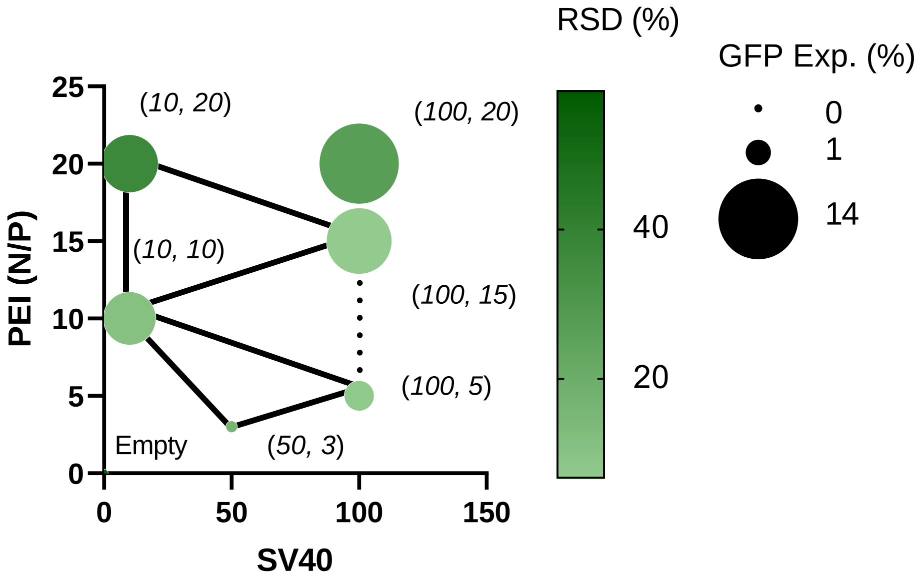

Figure 4-6. Reporter gene expression (GFP %) in HepG2 cells (t = 48h) treated with SPNPs and Lipofectamine controls as measured on a flow cytometer. PEI appears positively correlated with GFP expression, whereas SV40 may not be.

4.4.8 Viability and Uptake Do Not Predict GFP Expression

Upon inspection of the bubble plots presented in **Figures 4-5** through **4-7**, it can be observed that there is poor or no correlation between SPNPs that exhibit high uptake or viability and those with the highest GFP expression. To confirm this, the viability versus GFP expression and the uptake versus GFP expression are plotted against each other and a linear regression is applied (**Figure 4-8**). Visual inspection of the graphs reveals that neither viability nor cellular uptake predict a high GFP expression, as high GFP expression is seen for both higher and lower uptake and viability. Statistical analysis of correlation reveals a Pearson r = -0.65 for viability versus GFP expression and r = -0.73 for uptake versus GFP expression, indicating poor correlation. As noted, the viability ranges are not broad, and the difference in viability between the highest GFP expressing cell population and the lowest is only 10%. The range of cellular uptake is larger, representing a spread of 59%, but there is no correlation between percentage of particle-positive cells and GFP expression. These results indicate that neither the viability nor the uptake of SPNP-treated cell populations can be used to predict GFP expression of the same populations. That is, the only predictor of transfection efficiency as measured by GFP expression is the incorporation of PEI and to some extent SV40.

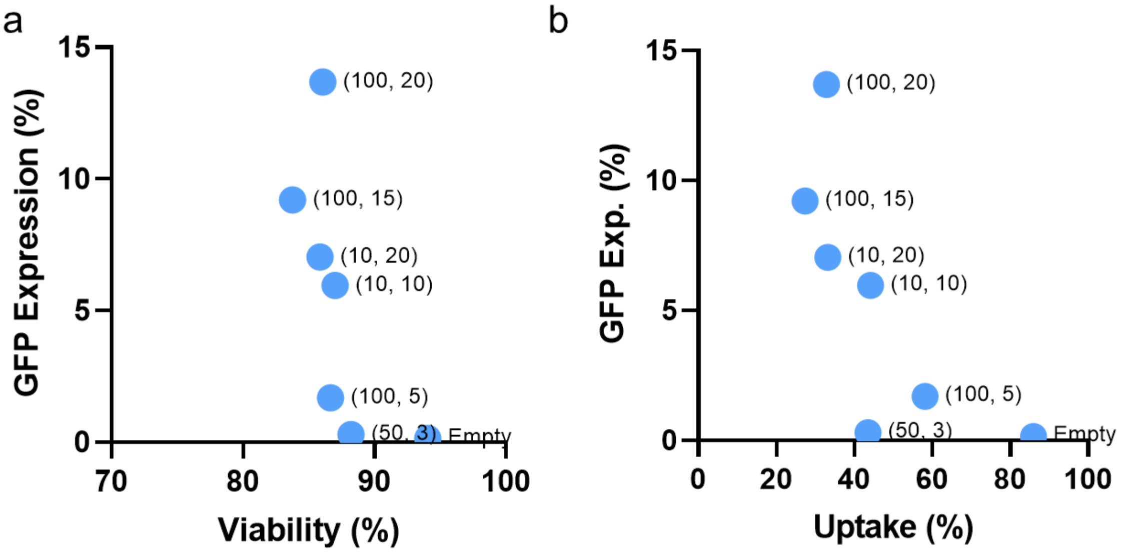

Figure 4-7.Lack of correlation between (a) cell viability and gene expression and (b) uptake and gene expression. In both cases, the biological output is graphed on the x-axis and there is no apparent trend between the x- an y- axes.

4.5 Discussion

Due to the role that PEI plays in escaping the endosome during endocytosis and the active transport hypothesized to be induced by the SV40 protein, they were both expected to correlate positively with GFP expression induced by SPNPs. It is, however, surprising that neither uptake percentage nor viability are predictive of the percentage of

GFP expressing cells. This is especially apparent when examining the high GFP expression rate induced by some SPNPs, namely (50, 3) and (100, 5), that entered cells at a high rate, but did not induce expression at a higher rate than other SPNPs. Paradoxically, the SPNP that induced the highest GFP expression (100, 20) exhibited both viability and uptake that was consistent with other lower performing SPNPs. Visual inspection revealed that the correlation between viability and GFP expression and uptake and GFP expression is non-existent, while the correlation between N/P ratio and GFP expression is strong ($r = 0.91$).

The conflicting results and unexpected findings presented here stress the necessity of a rational approach to designing vehicles for gene delivery. The use of the design strategy allows researchers to test a hypothesis and adapt the experimental plan at each endpoint based on the results gathered from the important outputs. Graphing the ongoing experiments in this way has several advantages including both ease of interpretation and planning the next steps. Additionally, trends that may have been overlooked when considering statistics are apparent when inspected visually in this way. This type of analysis also lends itself to rapid adaptation and allows researchers to be highly agile when designing their next set of experiments while quickly optimizing two parameters at once.

Rational design allows the ability to predict the functionality of different SPNP formulations based on biological output. By graphically mapping the design space and setting the anticipated important parameters, here PEI (N/P ratio) and SV40 content, this allows researchers to visually see where on the map the data is directing them to move. That is, by visual inspection of a graphed set of data, a researcher can pick the formulation of the next two SPNPs to be tested. Subsequent analysis of the data can reveal or confirm trends readily observed in the graphs. This is done with calculation of Pearson's r for correlation between constituent components and biological outputs. Each experiment yields information on optimization around the two axes graphed, speeding up optimization of output more than optimizing parameters one at a time.

Of course, it is important to recognize the limitations of this study as well. First, inspection of the trends revealed here begs the question of whether a higher incorporation of SV40 would further improve SPNPs that exhibited higher GFP expression. Future work would benefit from exploring higher ratios of SV40 at the highest GFP expressing SPNP formulations. Second, it is possible that the champion formulation (100, 20) would change with a different pDNA loading. As the effect of pDNA loading was not examined in this study, it cannot be ruled out that this will have an effect. Third, this work only examined *in vitro* reporter gene expression. Moving to organismal studies or a therapeutic payload may alter the results of this study and should be taken into consideration for future work.

While there are several limitations to the study as presented, the SPNP platform and strategy presented here enables future work to be streamlined and establishes a workflow that can be easily applied to various systems. This outline makes the SPNP pDNA delivery platform widely applicable and highly adaptable to various therapeutic uses, which are discussed in Chapter 6.

Chapter 5
On the Impact of Previous Work

In this chapter, I present work that I conducted during my Ph.D. study that was formative in my approach to research and allowed me the opportunity to develop a foundational understanding of a variety of techniques and disease states. Several manuscripts from these experiences have been published and have been well-received in the field.

5.1 Review Paper: Self-Healing Supramolecular Hydrogels as Biomaterials

The work discussed in this section is reported in **Appendix C** but can be read in its entirety in the following article:

1. L. Saunders, P.X. Ma, ”Self-Healing Supramolecular Hydrogels for Tissue Engineering Applications” Macromol. Biosci. 2019, 19, 1800313

One of the critical experiences that I had earlier on in graduate school came when I was tasked with writing a review on supramolecular interactions present in self-healing hydrogels for biomedical applications.[136] In a matter of six weeks, I was expected to become an expert in the subfield and to write a meaningful review on the topic. From this experience, I learned that a thorough literature review is not about how much you have read or how much knowledge you can gather, but about addressing what the reader of a review would want or need to know. I gained the ability to rapidly distill scientific papers and extract the information that I needed in a way that differed from conducting previous literature reviews in my Ph.D. studies. In the process of writing the review, I gained an appreciation for the amount of work and reading that conducting a “good” review demands. This experience gave me perspective on conducting literature reviews in the future, even if they were for my own knowledge and never formally reported.

Knowledge gained from this literature review was also instructive to the direction of my earlier research. The supramolecular moieties covered in this paper included the widely reported quadruple hydrogen bonding motif ureidopyrimidinone (UPy). I attempted to use UPy to drive autonomous and spontaneous self-assembly of a dextran-based hydrogel at physiologically relevant conditions in a project focused on cardiac tissue engineering (unpublished data, not reported here). The result of this period of intensive focus is a work that I am very proud of and was well-received by the field.

5.2 Bone Tissue Engineering

The work discussed in this section is not reported elsewhere within this thesis but can be read in its entirety in the following articles:

1. M. Dang, L. Saunders, X. Niu, Y. Fan, P.X. Ma, ”Biomimetic delivery of signals for bone tissue engineering” 2018, Bone Res 6, 25

2. Z. Liu, X. Chen, Z. Zhang, X. Zhang, L. Saunders, Y. Zhou, P.X. Ma, "Nanofibrous Spongy Microspheres to Distinctly Release miRNA and Growth Factors to Enrich Regulatory T Cells and Rescue Periodontal Bone Loss" ACS Nano, 2018, 12, 10 9785-9799

The focus of my first two years of graduate study was on utilizing RNA interference mediated by miRNA, siRNA, and influenced by growth factors for bone tissue engineering. Specifically, I worked on projects concerned with the distinct release of these factors and the spatiotemporal control of their release towards rescuing bone tissue loss.

miRNA delivery was the first topic in my graduate school experience that I took ownership of and my work with polymer complexes (polyplexes) for rescuing bone tissue loss culminated in publication of two manuscripts: one review article on biomimetic signals for bone tissue engineering[137] and a data paper on nanofibrous spongy microspheres to distinctly release miRNA and growth factors to enrich regulatory T cells and rescue periodontal bone loss.[138]

This data paper aimed to locally increase the number of regulatory T Cells (Tregs) to have an immunomodulatory effect and enhance tissue regeneration in periodontal bone. For my contribution to this paper, I used a new synthetic method to generate injectable poly(lactic acid-*co*-glycolic acid) microspheres (PLGA MS) and load them with miR-10 to recruit T cells and stimulate their differentiation into Tregs.

For the review paper I conducted a literature review of nucleic acid usage in bone tissue regeneration using immunomodulatory pathways. Towards this, I looked at the ability of both non-coding (siRNA, miRNA) and coding (DNA) genes to regulate cell activity and enhance or stimulate the healing process. As I conducted the literature review for both papers simultaneously, I was able to use insights from one process to inform the other and vice versa. These two papers were instrumental in piquing my interest in injectable scaffold delivery systems and the wider application of genetic engineering in the biomedical space. These themes were featured heavily in my successful F31 application titled “Development of a Polymeric Delivery System for Efficient in vivo Cellular Reprogramming for Cardiac Regeneration” which I was awarded in 2019 from the National Heart Lung Blood Institute at the National Institutes of Health.

5.3 Towards Cartilage Regeneration

The work discussed in this section is not reported elsewhere within this thesis but can be read in its entirety in the following article:

1. Q. Liu, J. Wang, Y. Chen, Z. Zhang, L. Saunders, E. Schipani, Q. Chen, P.X. Ma, “Suppressing mesenchymal stem cell hypertrophy and endochondral ossification in 3D cartilage regeneration with nanofibrous poly(l-lactic acid) scaffold and matrilin-3” Acta Biomaterialia, 2018, 76, 29-38

Another formative experience that I had in graduate school was contributing to the first data paper of my Ph.D. career that focused on utilizing 3D nanofibrous scaffolds to suppress mesenchymal stem cell hypertrophy and endochondral ossification for cartilage regeneration. In this project, I worked with senior graduate students to learn established methods of scaffold production. Through this work I gained a mastery of fabricating nanofibrous poly(L-lactic acid) (NF PLLA) scaffolds and contributed to the writing and editing of this manuscript. The readings that I did while participating in this work were foundational to my knowledge of tissue engineering and informed the direction that I pushed my research in for the remainder of my time in the Ma Lab.

5.4 Investigating Syringe Filtration as An Alternate Processing Method to Centrifugal Filtration for Synthetic Protein Nanoparticles

The material in this section is intended to serve as a guide for those who want to adapt filtration as an alternative processing method for synthetic protein nanoparticles (SPNPs) but is unpublished. This method has only been tested so far with NHS-PEG-NHS crosslinked SPNPs made with Human Serum Albumin (HSA) and would require preliminary testing with other proteins or crosslinking methods prior to adaptation.

5.4.1 Motivation

Currently, the method of processing SPNPs in the Lahann Lab uses serial centrifugal filtration (CF) until the desired diameter is reached according to dynamic light scattering (DLS) traces. Here, a method is reported that in certain circumstances, improves upon this process. The syringe filtration method reported here is more efficient in terms of materials, time, and is repeatable, achieving number average diameters between 60 – 94 nm as reported by number average DLS measurements. This size range is favorable for endocytosis of nanoparticles, the hypothesized method of uptake for SPNPs.[30,48] A schematic overview of the workflow described here is presented in **Figure 5-1.**

In addition to challenges with sample mass loss and inconsistencies between users, the processing of SPNPs is not conducted under aseptic conditions. This presents an issue as the SPNPs are often used *in vitro,* necessitating the use of antibiotics during cell culture*.* Antibiotics can obscure cellular function and issues that may arise during cell culture, making results from experiments more difficult to troubleshoot. The aim of this project was to test whether the use of a sterile, 0.22 µm filter can be used to simultaneously decrease the processing time, establish a repeatable process, and generate sterile SPNPs for use in *in vitro* and *in vivo* work as necessary.

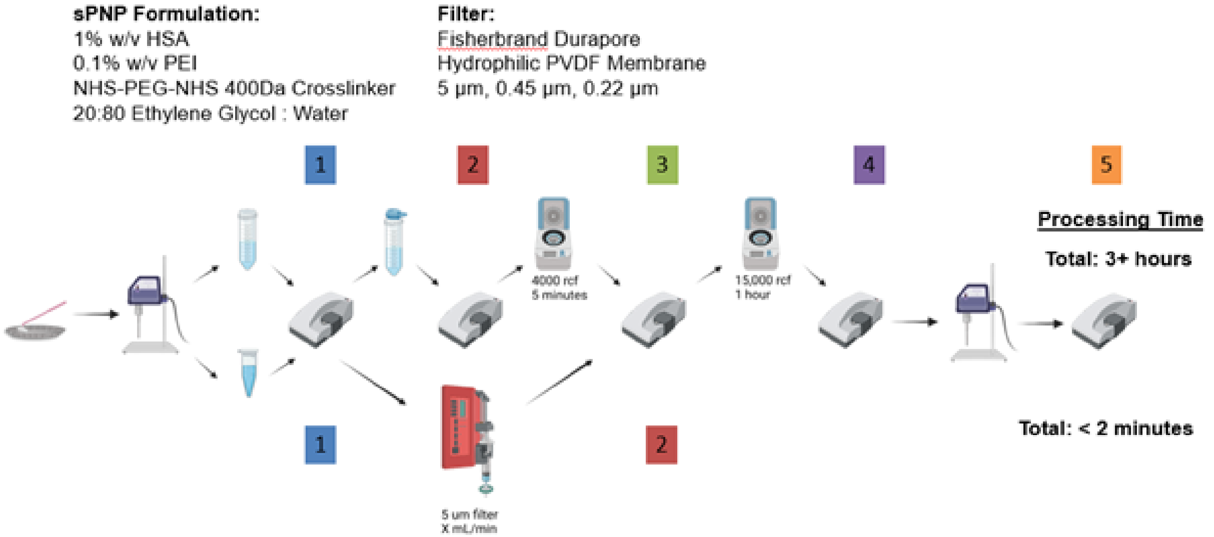

Figure 5-1. A general overview of the process for centrifugal filtration (above) and the finalized syringe filtration protocol (below) following collection of SPNPs. The SPNP formulation used in this set of experiments is detailed as well as the material used in the syringe filtration. Schematic made in part with Biorender.com.

5.4.2 Limitations to Centrifugal Filtration

The centrifugal filtration (CF) processing of the SPNPs is time-consuming, induces significant mass loss, is subject to interpersonal variability, and does not yield consistent SPNP populations. CF takes about 3 hours to perform and has been used in the Lahann Group to acquire SPNPs of the target size, as dictated per project. This process is subjective, though, and the accuracy and volume of refuse removed from the sample once it has been pelleted down varies from person to person. The volume collected from a sample is varies even between experienced lab members.

CF can also suffer from the inability to reproduce similar particle size distributions even amongst identical SPNPs. When the target size is not achieved according to DLS measurements, the SPNP solution is fractionated. The fractionation requires an additional centrifugation at 15,000 rpm (13,130 rcf) for 1 minute, then measuring this supernatant on the DLS. If the target size is still not achieved, this may be repeated for 5 minute and finally, if necessary, 10-minute spin-down times. As one might expect, this results in higher losses of product both due to transfer inefficiencies associated with measurement and increasing mass of SPNP product within the pellet. Once the product solution is deemed to be within an acceptable size range, the solution is transferred to a new microcentrifuge tube for storage, again increasing the lossiness due to transfer. Fractionation of SPNP solution is not routinely done for each sample, and thus it has not been investigated in this work. In addition to being used irregularly within the lab, projects presented in this thesis have not needed to employ this method and thus it was not investigated.

5.4.3 Filtration Method and Calculations Required

In this work, three different syringe filters of various pore size were used: 5 µm, 0.45 µm, and 0.22 µm. The material they are made with, hydrophilized PVDF, is already used with SPNPs in our lab. The filters were tested in order of pore size from largest to smallest on HSA SPNPs and the starting, intermediate, and ending populations were assessed using nDLS. The general workflow along with materials used is presented in **Figure 5-1**.

Each sample has its own concentration and the attenuator in the instrument adjusts automatically to ensure that the laser power that passes through the sample and hits the detector is at a level that will not harm it. A great guide with relevant information can be found at: https://physics.nyu.edu/grierlab/manuals/ZetasizerNanoUserManual.pdf

Two machine parameters are defined here that are critical to understanding of the Zetasizer and calculations performed. *Attenuation Index:* The laser power is attenuated by the software so that count rates are within the limits of the detector. *Count Rate:* The number of photons detected per second, the methods for mass approximation presented here are only accurate for solutions containing more than 1000 particles. The count rate per second must exceed 10,000 but remain below the aggregation limit of the sample.

Using the attenuation index to transmission conversion (**Figure 5-2a**) and data acquired from the Zetasizer (**Figure 5-2b**), the Relative Loss percent versus initial mass can be calculated (**Equation 5-4**):

$$Transmission = \frac{Transmission\ \%}{100} \tag{1}$$

$$m_1 = Relative\ Mass = \frac{kcps}{Transmission} \tag{2}$$

$$m_0 = Relative\ Mass_{Unfiltered\ Sample} \tag{3}$$

$$Relative\ Loss\ \%\ vs. m_0 \ = 100\frac{m_0 - m_1}{m_0} \tag{4}$$

Equation 5-(1-4) . Equations to calculate mass los and compare this between SPNP populations.

This measure of relative mass loss is used going forward to compare all sample masses to their respective starting populations. That is, this method is used to compare the initial sample mass to the sample mass at each step in either the CF or filtration processes and comparisons can be made between each.

5.4.4 Centrifugal Filtration for Human Serum Albumin Synthetic Protein Nanoparticles

A representative CF clean-up is presented in **Figure 5-3**, with each step analyzed using number average DLS. Using **Equations 5-(1-4)** and the attenuation index from the Zetasizer instrument (**Figure 5-2a**), the relative mass loss (%) is calculated for each step detailed in **Figure 5-3**. This process and calculation protocol is repeated two more times to ensure consistency. All diameters obtained with the CF and reported by DLS are typical for HSA SPNPs.[26,32]

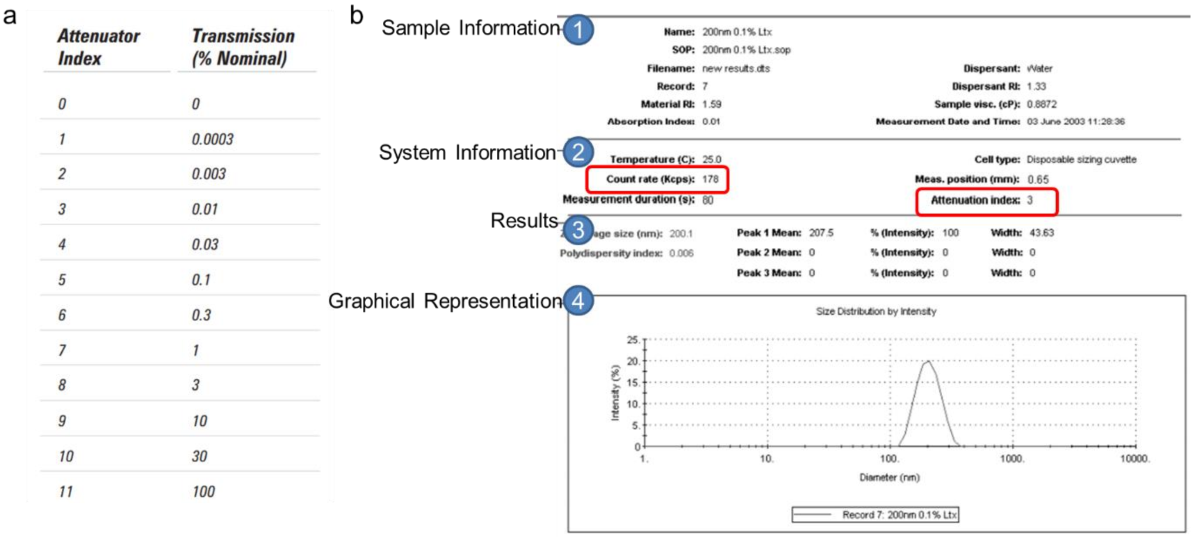
a

Attenuator Index	*Transmission (% Nominal)*
0	*0*
1	*0.0003*
2	*0.003*
3	*0.01*
4	*0.03*
5	*0.1*
6	*0.3*
7	*1*
8	*3*
9	*10*
10	*30*
11	*100*

b

Name: 200nm 0.1% Ltx
SOP: 200nm 0.1% Ltx.sop
Filename: new results.dts
Record: 7
Material RI: 1.59
Absorption Index: 0.01
Dispersant: Water
Dispersant RI: 1.33
Sample visc. (cP): 0.8872
Measurement Date and Time: 03 June 2003 11:28:36

Temperature (C): 25.0
Count rate (Kcps): 178
Measurement duration (s): 80
Cell type: Disposable sizing cuvette
Meas. position (mm): 0.65
Attenuation index: 3

Z age size (nm): 200.1
Polydispersity index: 0.006
Peak 1 Mean: 207.5 **% (Intensity):** 100 **Width:** 43.63
Peak 2 Mean: 0 **% (Intensity):** 0 **Width:** 0
Peak 3 Mean: 0 **% (Intensity):** 0 **Width:** 0

Figure 5-2. Readout from the Zetasizer when running DLS measurements. (a) Attenuation index and the % nominal transmission of laser light that corresponds to each attenuator reading as well as sample information, obtained from the Zetasizer Manual. (b) System information, and results that will be used for calculation and better understanding of this method are presented.

5.4.5 Collection Method of Synthetic Protein Nanoparticles

The process begins with collection of SPNPs from the pans on which they were jetted. Once the solution is collected, the entire population is sonicated using a tip sonicator for 30s while submerged in an ice-water bath. This well-dispersed solution is measured via DLS then split into two equal parts by volume. One part undergoes CF and the other undergoes syringe filtration to ensure that the starting population is identical and to enable direct comparison between the initial DLS traces and measurements taken after each step in the workflow.

Following sample splitting, the CF sample is filtered through a 40 µm cell strainer, then a DLS trace is taken. Next, the CF sample is centrifuged at 4000 rpm / 3220 rcf for 5 minutes, and the supernatant is again measured via DLS. It is at this step that the first user judgement is required, and interpersonal variability is likely first introduced. When collecting the supernatant, the user employs a pipette to collect as much of the supernatant as they can, without disturbing the pellet, which is waste. Depending on the comfort and skill level of the user, a different amount of supernatant is collected, and the pellet may or may not have been disturbed during the process.

Next, the supernatant is loaded into microcentrifuge tubes and spun at 13,130 rcf for 1 hour. This again has the same potential for collection error as the previous transfer step. The resulting supernatant is the final SPNP solution and is analyzed using DLS. For DLS measurement, the pellet is resuspended in 1x DPBS using the same sonication protocol as above. Finally, this solution is measured on DLS. The resulting DLS traces at each step are presented in **Figure 5-3**.

From the relative mass loss calculations, it is clear that this method cannot capture the mass changes in the resuspended pellet but is consistent for the 2 repeats up until that point. It can be assumed that the mass loss expected in the resuspended pellet would be 100 – relative mass loss % achieved up to that point, and then might be close to 70%. That is, mass loss measured after the 5-minute spin-down is approximately 40% and the supernatant mass loss is around 70%, taking 70% of 40% and summing that with 40% results in 68%. The mass loss seen across the samples as the CF process is carried out is concerning both from a processing standpoint and for those researchers that work with precious samples, such as SPNPs loaded with difficult to manufacture and/or expensive therapeutic materials.

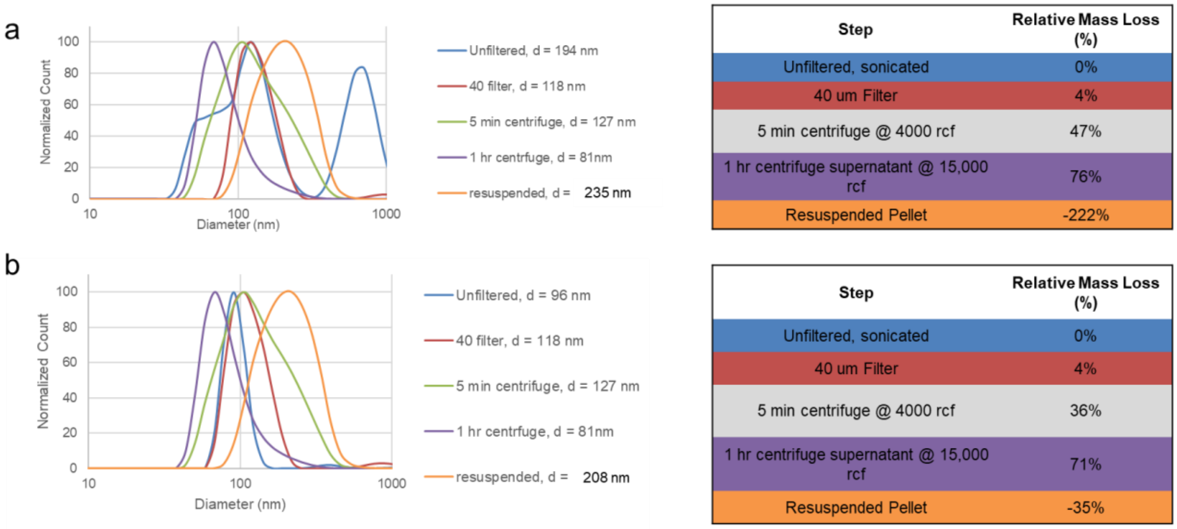

Step	Relative Mass Loss (%)
Unfiltered, sonicated	0%
40 um Filter	4%
5 min centrifuge @ 4000 rcf	47%
1 hr centrifuge supernatant @ 15,000 rcf	76%
Resuspended Pellet	-222%

Step	Relative Mass Loss (%)
Unfiltered, sonicated	0%
40 um Filter	4%
5 min centrifuge @ 4000 rcf	36%
1 hr centrifuge supernatant @ 15,000 rcf	71%
Resuspended Pellet	-35%

Figure 5-3. Representative CF clean-up of HSA SPNPs. Each panel (a, b) is a repeat of the same process with a new population. The orange trace is the resultant SPNP population following processing and each trace is color-coded with the corresponding value in the resultant SPNP population following processing and each trace is color-coded with the corresponding value in the table.

5.4.6 Syringe Processing Filtration of Synthetic Protein Nanoparticles

Prior to using a filter for the first time, the filter must be hydrated to prevent lossiness of solution in the holdup volume and ease the passage of the solution through the pores. To do this, 1 mL of dPBS is passed through the sterile filter to prime it for the SPNP solution. Following sonication and sample splitting, the SPNP solution is loaded into a 1 mL luer-lock syringe. The primed filter is attached to the luer-lock and the entire system is loaded into the syringe filter for use with SPNP solution.

A syringe pump is used to ensure the rate at which filtration is conducted remains constant throughout the experiment as well as making the process repeatable for any user. A pump rate was chosen based on the diameter of the syringe being used. In this experiment, a flow rate 0.3 mL/min was set for a 1 mL syringe. The entire volume of SPNP solution is pumped through the filter into a collection vial. Next, the filter is removed and retained while the syringe is charged with air, the filter is reattached, and the entire volume of the syringe is again pumped down into the collection vial to ensure that losses of SPNP product are minimized. This solution is the final product.

5.4.7 Appropriateness of a 5 µm Filter for Synthetic Protein Nanoparticle Processing

Following the sonication of the starting population, the half of the sample reserved for syringe filtration is passed through a 5 µm syringe filter to remove dust particles and large precipitates that are present. This step is done to mimic the 5-minute low-speed centrifugation step that results in removal of large aggregates and other refuse in the collected SPNP sample. A DLS trace resulting from this process is presented in **Figure 5-4**. Filtration through a 5 µm syringe filter is done three times in series on the same population to see if there are inconsistencies within this step. Of particular concern was the possibility of SPNP anisotropy that would lead to the filters producing a different sub-population each time. Also of interest was the relative mass loss and how that would increase across filtration steps.

The DLS traces (**Figure 5-4**) indicate that the filtered populations are nearly identical even following repeated passage through the filter. This experiment shows repeatability, and a relative mass loss similar to the supernatant achieved following the 5 minute 3220 rcf centrifuge step as seen is **Figure 5-3**. Importantly, there are no decisions or judgement calls in the syringe filtration process, like is seen at this point for CF. Also of interest, this entire sample is pumped through the syringe filter in under 2 minutes and there is no sonication required to resuspend the pellet, as there is no pellet. This removes a step of state transition (solution to solid to solution) as well as the aggressive sonication needed to resuspend the pelleted mass. With biomolecules and proteins, often the less manipulation, the closer they resemble their native state.[139]

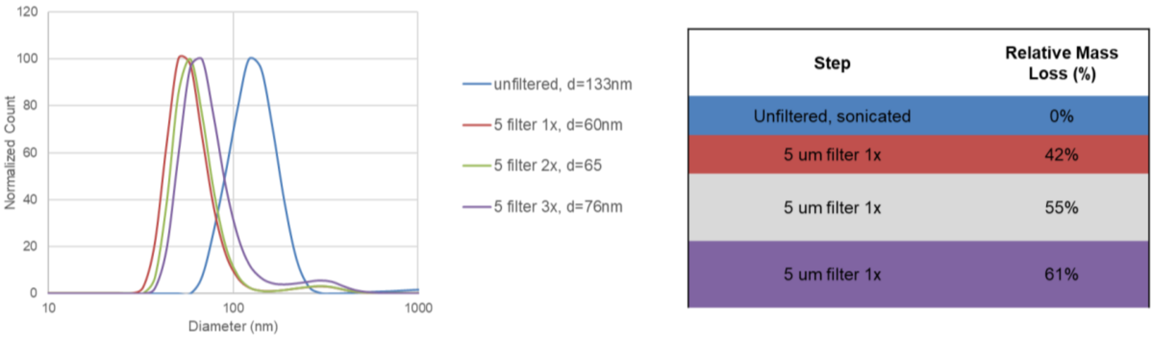

Step	Relative Mass Loss (%)
Unfiltered, sonicated	0%
5 um filter 1x	42%
5 um filter 1x	55%
5 um filter 1x	61%

Figure 5-4. A DLS trace of the starting population and resultant DLS traces following serial filtration of the population using a 5 µm syringe filter. The 5 µm filter was successful in obtaining a repeatable population with a center of mass diameter between 60 and 76 nm.

The nDLS in **Figure 5-4** shows that the three populations acquired from the 5 µm syringe filter have similar particle size distributions with number average diameters between 60 – 76nm. The slight change in mass across the 3 passes indicates that while some material is retained within the filter itself, the SPNPs may have a low anisotropy as they pass through the filter repeatedly. If they were highly anisotropic due to being oblong or extended in one direction, one would expect to see more mass loss and potentially higher degree of change in number average diameter, neither of which is seen here.

Use of the 5 µm filter was successful in obtaining a repeatable population in the target size range (<150 nm). Syringe filtration also induced less mass loss than centrifugation up until the 5-minute spin-down and assuming the balance of supernatant is retained in the pellet. As noted above, the actual population of the final solution cannot be accurately measured, as all relative mass loss % are negative. The negative mass loss read by the DLS may also indicate that the population is changing. This could be due to aggregation between particles and a resultant change in the amount of surface available to read. This is supported by both the broadening of the nDLS peak in the resuspended SPNPs vs. filtered populations and the increase in size of the nDLS trace of the 5 min population vs the 1-hour population (**Figure 5-2**).

5.4.8 Appropriateness of a 0.45 µm Filter for SPNP Processing

As the 5 µm filter met the metrics, a filter of 0.45 µm pore size was next used to determine if any residual SPNPs at 450 – 500 µm could be removed or decreased in number. SPNPs in this size range can be seen in **Figure 5-4**, and are often too large to be effectively endocytosed.[44] First, the particle size distributions of the initial population and a subsequent 5 µm syringe filter are measured using DLS. Then that same solution is passed through a 0.45 µm syringe filter. The population size distribution changes with each pass through the 0.45 µm filter and is broader than the population passed through the 5 µm alone (**Figure 5-5**). This indicates that the 0.45 µm filter appears to be shearing the SPNPs. In addition to the unreliable sizes obtained and higher dispersity seen, the mass loss of SPNP solution following use of the 0.45 µm filter was around 80% or more. Since the intention of this project was to establish a repeatable filtration method, the use the 0.45 µm filter was discontinued due to its mass loss and inconsistent size distributions resulting from its use.

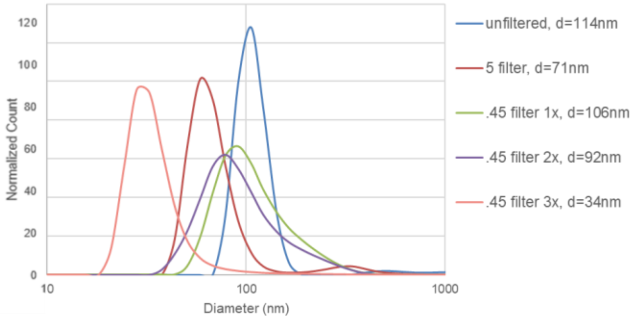

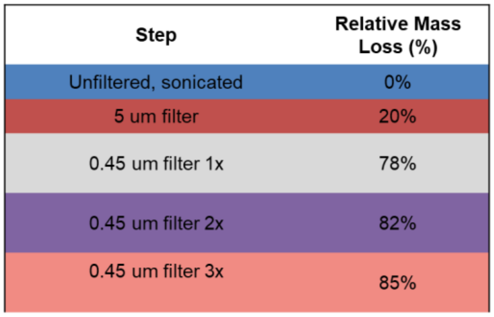

Step	Relative Mass Loss (%)
Unfiltered, sonicated	0%
5 um filter	20%
0.45 um filter 1x	78%
0.45 um filter 2x	82%
0.45 um filter 3x	85%

Figure 5-5. A DLS trace of the starting population and resultant DLS traces following syringe filtration first with a 5um pore size filter, then with a 0.45 µm filter in series (3 times). The 0.45 µm filter appears to be shearing the SPNPs as the population changes with each pass and is broader than acquired by the 5 µm.

Originally, use of a 0.22 um “sterile” filter was the aim for this work as it would remove the need for culturing cells with antibiotics or preparing the SPNPs with ethanol to sterilize them. However, this was abandoned as a 0.45 µm filter resulted in shear of the SPNPs. Furthermore, preliminary results indicated that a 0.22 µm filter induced mass loss over 90%, preventing collection of reliable DLS traces.

5.4.9 Effect of Filtration Rate on Particle Size Distribution

Next, increasing the rate of syringe pump filtration was tested to obtain the maximum rate at which repeatable results can be achieved with the lower mass loss than CF. Regardless of the starting population, the diameter peaks resulting from 5 µm filtration at various flow rates are between 79 - 88 nm at their center of mass (**Figure 5-6**). The syringe pump was tested at a range of flow rates of 0.14 – 1.71 mL/min for a 1 mL syringe.

Again, after undergoing syringe filtration, all populations observed were compared against their respective starting populations, which varied in number average size from 90 to 403 nm. All populations resulting from 5 µm filtration had average diameters between 79 and 94 nm regardless of the syringe pump rate. Additionally, all samples

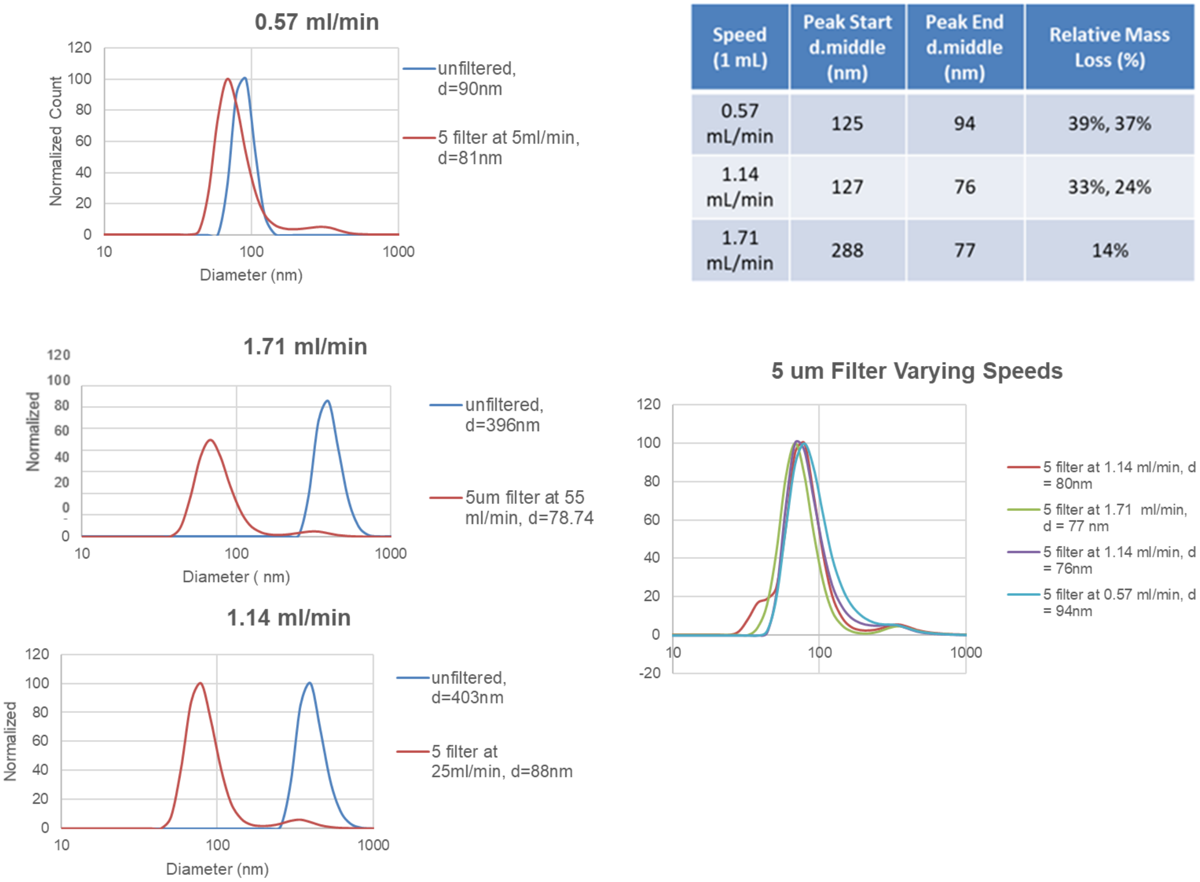

Speed (1 mL)	Peak Start d.middle (nm)	Peak End d.middle (nm)	Relative Mass Loss (%)
0.57 mL/min	125	94	39%, 37%
1.14 mL/min	127	76	33%, 24%
1.71 mL/min	288	77	14%

Figure 5-6. Investigation of the resultant population following varying the pump rate and method of sonication on the syringe pump. Regardless of the starting population or sonication method used, the resultant diameter peaks are between 77 - 94 nm at their center of mass.

resulting from 5 µm filtration have a DLS peak in the 200 - 300 nm range, which may be the result of aggregation within the sample that is not removed in the 5 µm size range.

Regardless of the starting population or filtration rate, the 5 µm filter results in a consistent final population, which is important to the reliability and reproducibility of SPNP populations. Therefore, it is believed that pump filtration rate does not affect the size distribution of the particles. However, a lower relative mass loss % was observed in the highest pump filtration flow rate.

5.4.10 Effect of Sonication on Particle Size Distribution

As mentioned, the aggressive solution disruption induced by the tip sonicator was of concern as it contributes to formation of aggregates and can compromise the integrity of delicate biomolecules. Therefore, the effect of sonication amplitude using both a tip and a horn sonicator was tested. First, the initial SPNP solutions were tested using the two different methods and amplitudes to ascertain the result of sonication on the initial populations. If gentler sonication resulted in populations consistent with populations obtained using the tip sonicator, this would enable less sonication of the SPNP populations. Following various initial sonication methods (**Figure 5-7**), the SPNP samples were passed through a 5 µm syringe filter and the resulting populations were assessed via DLS. The starting population is not reliably changed due to sonication (**Figure 5-7a**), but once passed through a 5 µm syringe filter, final SPNP populations of around 75 nm were reliably obtained (**Figure 5-7b,c**). This indicates that future work might not require substantial sonication if a syringe filter is utilized to process a SPNP population, which would be advantageous to researchers using delicate payloads within the SPNPs.

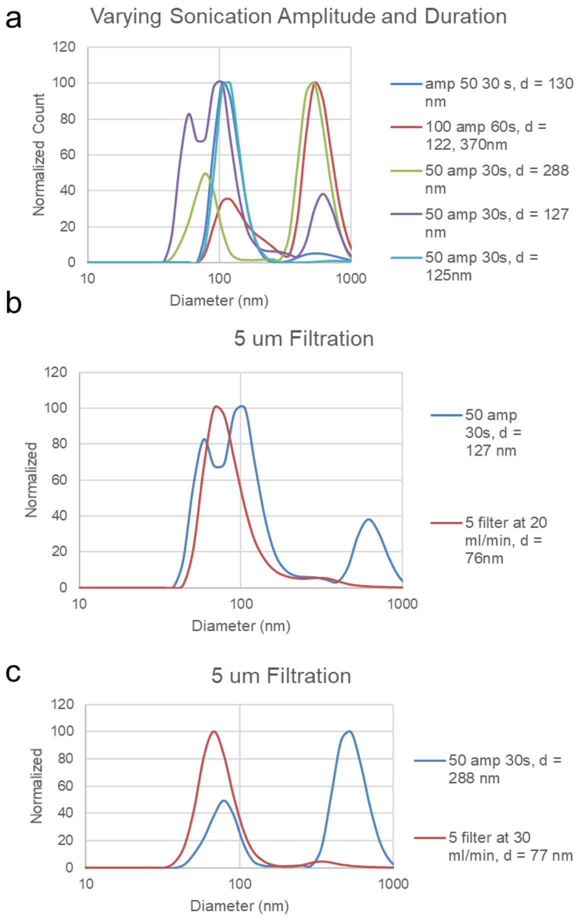

Figure 5-7. Effect of sonication on starting populations and efficacy of 5 um syringe filtration. (a) Varying sonication methods results in unreliable starting populations of SPNPs (b, c) syringe filtration consistently yields similar SPNP populations.

5.5 Conclusions

This work established that syringe filtration using a 5 µm pore size results in consistently sized SPNP populations with mass loss similar to CF regardless of the starting population. Across each experiment, SPNP solutions resulting from the use of a 5 µm syringe filter exhibited number average diameters ranging from 60 – 94 nm. These diameters are within the biologically relevant size range for endocytosis of SPNPs. Adding to the reproducibility of this method, use of syringe filtration is done with a syringe pump to ensure constant and precisely controlled pumping rates. This consistency cannot be replicated using CF where the recovery of the pellet and supernatant following centrifugation depend on the user's judgement and introduce interpersonal variability.

Additionally, this method benefits from less manipulation of the SPNPs than CF, resulting in less mass loss of the SPNP sample. The mass loss in CF can be attributed to incomplete recovery of sample after spin-down and to transfer inefficiencies between multiple centrifuge tubes. While these are non-existent in the syringe filtration method, there is some mass loss associated with holdup in the syringe filter itself. This is expected, and a mass loss of zero is not possible in any system, as the SPNPs are not monodisperse, meaning there will always be some portion of the population outside the intended size range. Also, the collection method used to obtain the SPNPs may result in collection of dust and aggregates that are not part of the sample. These may contribute to the measured initial SPNP mass if they are not filtered out.

Finally, the syringe filtration method represents a time-saving processing step that simplifies the process of obtaining consistently sized SPNP populations. Syringe filtration takes under 15 minutes to complete. It requires only pre-wetting the filter, loading the syringe, pumping the sample through the filter, and passing air through the filter to collect any residual sample held up in the filter. Due to the ease of application and promising preliminary results, this method should be further investigated for future applications within the Lahann Lab.

5.6 Future Work and Outlook

The syringe filtration method represents a promising step towards a repeatable and streamlined workflow, but there are some questions to be addressed. Future work in this area should include testing of various SPNP concentrations, as pressure-based filtration might change due to sample concentration. Higher concentration might cause the filtration to be more inefficient and induce higher mass loss or necessitate a lower pump rate. The inability to concentrate samples without addition of another technique is a limitation of the method presented here. Regardless, this should be explored prior to application of the method to very concentrated solutions.

Another consideration is whether filtration influences the surface charge of the final SPNP population. The zeta potential can be readily measured and compared between the final populations obtained using CF and syringe filtration methods. Future work should include this prior to applying SPNPs to *in vitro* work. It is likely that the surface charge measured would change slightly, as larger SPNPs have more surface area than smaller SPNPs. I would expect the surface charge to increase for smaller SPNPs that have a higher surface area to volume ratio.

Aside from DLS measurements, these results should be corroborated with nanoparticle tracking analysis such as the NanoSight as this can offer greater resolution of the particle size distribution. NanoSight can also ascertain particle concentrations (number/mL) more accurately than DLS can, and mass loss can be validated in this way. This was not done in this work, as DLS is higher throughput and offers a wider range of nanoparticle sizes making it ideal for screening in preliminary work such as this.

Generally, SPNPs are produced in the Lahann Lab for use in either cell or organismal studies, and as such, this work should be extended to *in vitro* experiments. The viability and uptake of resultant SPNPs should be tested in cell lines to ensure that they exhibit similar properties to SPNPs processed using CF, although it is unlikely. A change in the surface charge of the SPNPs, consequent of differences in surface area to volume ratio, might confer differences to the viability and uptake and should be considered.

The aim of this work was to establish a repeatable method to sterile filter SPNPs while maintaining tolerable mass loss compared to CF. Part of this was achieved, with a 5 µm syringe filter offering a consistent and time-saving method while achieving mass loss lower than or approaching CF. However, sterile filtration was not achieved due to the 0.22 µm syringe filter causing more than 90% mass loss of the sample. Therefore, resultant SPNPs still require antibiotics for use *in vitro.* The repeatability of this work lends itself to scale up, as the parameters can be controlled and replicated. Overall, this work represents a promising step towards improved processing of SPNPs, and a streamlined workflow for SPNP production.

Chapter 6

Outlook and Future Work

6.1 Conclusions

The work presented in this thesis establishes methods to formulate and characterize plasmid-loading in nanoparticle delivery systems for gene delivery. First, plasmid DNA (pDNA) loaded synthetic protein nanoparticles (SPNPs) were prepared and fully characterized using a method presented in Chapter 2. The plasmid backbone labelling (PBL) strategy quantifies the amount of pDNA present in a system. Compared to three commercial DNA quantification methods, the PBL strategy showed the lowest measurement bias in SPNPs. It is the only approach of the four methods tested that is fit for use in the presence of protein and in crosslinked SPNPs. An in-depth protocol for utilizing the PBL strategy is presented in Chapter 3 to enable researchers to adapt this strategy to their needs.

Next, the impact of altering the formulation of pDNA loaded SPNPs was examined to understand the effect of engineering decisions on biological outputs of the SPNP platform. A rational design strategy was established and the impact of polyethyleneimine (PEI) and SV40 peptide content on reporter gene expression mediated by various SPNPs was examined in Chapter 4. We found that PEI content positively correlates with reporter gene expression in HepG2 cells. While SV40 alone was not correlated with reporter expression, it did increase the efficacy of SPNPs across formulations with the same PEI content.

Also examined within this thesis was a new method for processing SPNPs to reduce the mass loss and increase the repeatability of the process. A syringe filtration system was established that might allow future work to be done more efficiently. When the syringe filtration system was compared to centrifugal filtration, it decreased the processing time eight-fold and led to significantly lower mass loss.

This work will be instructive to future researchers looking to design new and improved gene delivery vehicles as well as those looking for new ways to analyze and better characterize their systems. Laid out below are some immediate applications of this work, potential combinations of the presented technologies, and considerations for translation of this work to organismal studies.

6.2 Applications of the Plasmid Backbone Labeling Strategy to Various Nucleotides

Chapter 2 presented a set of fully characterized SPNPs with a pDNA payload using the newly developed PBL strategy. This is beneficial and important for work done in the Lahann Lab, as there is now an established strategy for quantifying the loading of pDNA within the SPNPs. Additionally, Chapter 2 discusses the framework of a tandem PBL/Dynamic Light Scattering (DLS) approach that allows researchers to determine the distribution of the pDNA payload within the particle population with a level of granularity not widely reported in the literature. It was found that the PBL strategy had lower measurement bias than UV-Vis spectroscopic methods, fluorescent groove-fitting assays, and colorimetric assays in SPNPs. The PBL strategy was suitable for pDNA quantification in both a protein-rich solution and in crosslinked SPNPs as determined by the low bias. In this work a roadmap was created that will allow future researchers to apply the methods detailed in Chapter 2 in part or in whole to various systems. This blueprint is useful for researchers that would benefit from this level of granularity in their particle analysis, as characterization of DNA payloads in nanoparticles remains underinvestigated in the field.

With the ability to fully quantify the amount of pDNA present, future efforts could focus on applying the PBL strategy to a variety of systems to quantify other parameters of interest. For example, the PBL strategy could be employed to determine release of pDNA from SPNPs, as well as the stability of these SPNPs in aqueous solutions. The pDNA loss associated with sonication or other purification techniques such as centrifugation could also easily be measured with accuracy. This would allow researchers to gain further insight into pDNA loaded systems and understand the usage of their nanoparticles.

Although developed for use with pDNA loaded SPNPs, the PBL strategy could be extended to SPNPs with different nucleotide payloads. The siRNA SPNPs used within the lab might benefit from application of the PBL strategy to quantify loading, release kinetics, and other parameters of interest. Since these parameters have been measured indirectly thus far, and dosing information for future studies could be obtained using the PBL strategy to understand these parameters more accurately. Similar information for SPNPs loaded with additional nucleotides of interest, including miRNA and mRNA could also be easily gathered and assessed in the same way presented in Chapters 2, 3, and 4. By quantifying loading and release kinetics more accurately using the PBL strategy, the design of SPNPs can be optimized to improve their intracellular fate which can be interrogated via imaging or flow cytometry.

6.3 Applications of the Plasmid Backbone Labeling Strategy to Intracellular Tracking

Although not tested within the work presented in this thesis, the fluorophore kit used herein is designed for intracellular tracking, allowing the intracellular trafficking of SPNPs to be observed. While the path that DNA must take to be expressed by a cell is well-known, the fate of DNA-loaded SPNPs has not been investigated and remains a black box. By following the path of the nucleotide through cells that have been transfected, researchers can identify if there are stumbling blocks to the expression of the nucleotide. A natural extension to this work would be to test different SPNP formulations to see if they can overcome these hurdles.

To enable researchers to apply the PBL strategy for intracellular tracking, Chapter 3 describes in-depth the methodology employed and considerations that need to be taken when adapting PBL to a new nucleotide or fluorophore system. It should be emphasized that the broad applicability and modularity of the PBL strategy is a strength and provides a key tool for quantification of the SPNP system but could be broadened to use with other bio macromolecular gene-host systems.

6.4 Towards Improving Reporter Gene Expression

Chapter 4 lays out the rational design of pDNA loaded SPNPs to achieve the desired output of GFP expression using a two-dimensional parameter space. Although this work presents a clear rational for the design of future SPNPs, the maximum GFP expression achieved was still modest and there is room for improvement. Future work should focus on developing a SPNP system with improved reporter gene (GFP) expression so that it can be applied to induce a therapeutic effect. While the expression observed in Chapter 4 may be sufficient to induce a therapeutic effect, a higher efficiency would likely result in a more effective treatment.

While optimizing the GFP expression induced by SPNPs, certain design rules became apparent. It was found that increasing PEI (N/P) content increased GFP expression, however, upon attempting higher N/P ratios than reported, precipitation of the solution was observed and SPNPs could not be reliably formed. As reported in Chapter 4, increasing SV40 content in the SPNP results in a modest increase in reporter gene expression, although it is not predictive. Therefore, use of higher SV40 peptide amounts should be investigated to ascertain whether that has a positive effect on GFP expression. While higher GFP expression is investigated, it will be important to ensure that the cell viability does not drop too low, decreasing the overall efficacy of the SPNPs. Although there was also not a reported effect of SV40 on the uptake of SPNPs into the cells, this is biological output should be monitored.

As this work was constrained to a two-dimensional design space, future work could benefit from exploring other parameters, including increasing the pDNA loading amount or delivering a higher pDNA amount to cells. Increasing the pDNA dose has been shown to increase SPNP-induced GFP expression in other work (**Figure 6-1**). The pDNA loading was held constant (4.5 m/m%) and the amount of pDNA delivered into each well was varied from 50 – 500 ng per well in a 96-well plate. In each case in Chapter 4, the dosage tested was 100 ng per well in a 96-well plate. **Figure 6-1** shows that although the SPNP tested had minimal (~3%) GFP expression at 100 ng, raising pDNA loading continued to increase GFP expression. The GFP expression (10%) achieved at 500 ng neared the highest expressions achieved in the studies reported in Chapter 4 while the viability remained above 90%. Taking this into consideration, higher amounts of pDNA should be tested in future work and might be a promising route to increasing GFP expression without affecting other biological outputs such as viability.

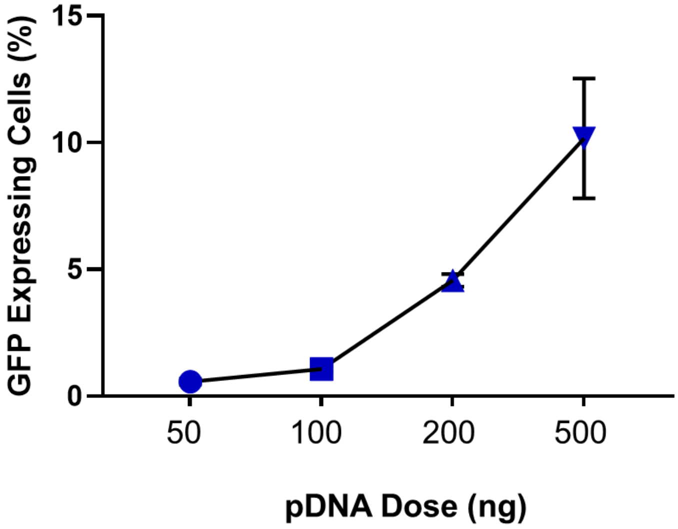

Figure 6-1. Increasing pDNA delivered to HepG2 cells using the same SPNP increases GFP expression. The typical dose used in all work presented here was 100 ng per well in a 96-well plate and this was varied to 50ng, 200ng, and 500ng. A strong increase in GFP expression in seen as the pDNA dose delivered is increased.

6.5 Towards *in vivo* Application of Synthetic Protein Nanoparticles Mediated pDNA Delivery

The foundational understanding of SPNP loading and characterization that this work enables will be instrumental in applying and utilizing systems for biomedical purposes. Further application of DNA loaded SPNPs will require translation into organismal studies, which come with their own obstacles.[140–142] The work reported here to develop a platform for SPNP gene delivery was conducted entirely *in vitro*, however the eventual goal of this work is to deliver therapeutic DNA to human patients. As such, it is important to consider the steps needed to move this *in vitro* technology past potential barriers that exist to animal models and eventual human studies. Barriers to effective gene delivery exist at the cellular, organ, and organism levels, and different engineering strategies and considerations must be exploited to overcome each unique hurdle. Obstacles to effective cellular delivery have been discussed at length throughout this thesis, and so considerations for organismal SPNP delivery will be reviewed here.

The method of SPNP delivery is a major consideration, as a systemic injection will result in different obstacles than a direct injection or locally administered scaffold. Discussion here will focus on systemic injection, which has been performed with SPNPs in the past.[32,123,143] Upon systemic IV injection, SPNPs enter the bloodstream and are subject to clearance by the reticuloendothelial system and the mononuclear phagocyte system.[144] A critical hurdle for all nanoparticles is crossing the cell membrane to be taken up into the target cell before they are cleared from the body.[112] *In vitro*, this barrier is not as formidable as it is in animals, as *in vitro* experiments are designed such that the cells in the dish are the target cells for transfection, and typically the only cell type present.

There is also no consideration taken of clearance time and the treatment is directly delivered to the dish in which the target cells reside. In animals, active targeting of nanoparticles to specific organs using surface-available ligands such as RGD, GalNAc, or folate has benefits such as improving cellular uptake and decreasing non-specific uptake in other organs while allowing nanoparticles to utilize more than one endocytic route to uptake.[46,47,145] For these reasons, active targeting of SPNPs to cells is expected to be much more beneficial *in vivo* than *in vitro*.

Within an organism, organs and organ systems are not equally accessible to therapeutics and different strategies are required to increase delivery to target organs. Some organs such as the liver, are easily reached by nanoparticles, a property which has been exploited by dozens of research and clinical trials for gene therapy.[146,147] For hepatic delivery this is advantageous, however for delivery to other organ systems, this can present an additional and formidable barrier.[146] The biodistribution of gene delivery systems is of great importance to the efficacy and off-target effects generated by the platform.[32,148] Indeed, active targeting agents for particular organ systems are often utilized to enhance localization of the gene delivery vehicle to an organ or tissue.

Utilizing active targeting for organ specific delivery of therapeutics is a promising and established strategy for improving efficacy of the therapeutic by enhancing delivery to the intended site.[149] Increasing the efficacy would be of particular advantage in delivery platforms which exhibit modest efficacy, as seen with the pDNA SPNPs presented in this thesis. Of note, GalNAc has been utilized with siRNA-conjugates to enhance hepatic delivery[47,150] and inflammation markers (ICAM, VCAM) have been used in stroke models to increase the recruitment of nanoparticles to inflammation sites.[151] This technique can be extended to red-blood cell hitchhiking that crosses the blood brain barrier, one of the most formidable barriers in the human body.[152] HSA, the protein used as the bulk material in SPNPs, has many sites available for conjugation of various targeting ligands. This presents ample opportunity for modification of HSA SPNPs and tailoring to specific disease states or for delivery to target organs. The ability to easily add targeting ligands further enhances the broad applicability and facile adaptability of the SPNP pDNA system presented in this thesis.

Another strategy for tailoring SPNPs to a specific organ or disease state involves replacing the HSA with another protein that has specific or complimentary biological features to enhance therapeutic efficacy. Proteins such as transferrin, hemoglobin, insulin, and ovalbumin have been reported to form stable SPNPs.[26,121,124] Choosing a different protein depends on the biology that one wishes to exploit. The HSA used to formulate the SPNPs for pDNA delivery is a generic protein with many favorable features including wide availability, good biocompatibility, and prior use in gene delivery systems.[32,37] However, this system can be adapted to a specific disease state or biology with a facile change in the bulk protein used. Due to the plug and play nature of SPNP preparation, doing so requires swapping the HSA with the new protein prior to EHD jetting and proceeding with formation and collection in a manner identical to HSA SPNPs.

While the work here utilizes a GFP reporter pDNA, preclinical and clinical trials will utilize various genes delivered to address different therapeutic targets. Considerations for changing SPNP formulation to accommodate changes to the gene delivered mainly revolve around the size of the gene. The presented formulation of SPNP was calibrated for a certain molecular weight of pDNA (3487 bp), and therefore a change in PEI amount to retain the desired N/P ratio will be required. Additionally, SV40 is added in a molar ratio to the pDNA in the formulation, which will change depending on the molecular weight of the gene delivered. These changes to formulation will be necessary to maintain the optimized formulation presented in this thesis. It may be, however, that a significantly smaller or larger gene is required, and in this case, *in vitro* testing consistent with that presented in Chapter 4 should be conducted prior to application. The strategy for SPNP optimization is detailed in Chapter 4 and can be readily applied to new genes and SPNP formulations if needed. Further, the PBL strategy in Chapter 2 can be utilized to establish the pDNA loading after modifications so that the dose of the new gene can be known and iterated upon if need be.

The SPNP pDNA system is a plug and play system that is almost endlessly adaptable, presenting a broad platform for delivery of therapeutics. As described, the preparation and formulation of SPNPs enable a facile change in bulk protein, amount of PEI and SV40, and the gene (pDNA) used. This platform can be expanded towards delivery to certain organs by conjugation of different ligands to the SPNP surface in a post-processing step. With this arsenal of readily available modifications and strategies for quantifying the loading and optimizing the formulation of SPNPs after modification, application towards animal and human health models is feasible.

6.6 Towards Therapeutic DNA Delivery in Human Patients

The broad applicability of pDNA delivery with SPNPs is promising for various applications in human health. A potential application should fulfill the requirements of utilizing pDNA delivery, requiring a lower immune response than is induced by currently available vectors, and using of the plug and play capabilities of the SPNP platform.

One such application is vectored immunoprophylaxis (VIP), the practice of inducing immunity in a population via delivery of genes that code for antibody secretion. VIP uses the host as a sort of factory to make antibodies against a particular virus. This approach has implications in providing immunity without vaccination and requires efficient delivery of a pDNA. Current technologies, however, utilize adeno-associated viruses which have safety and immunogenicity issues. pDNA loaded SPNPs offer a safer alternative approach to this application, with many benefits and considerations discussed here.

Despite success developing effective vaccines for a number of diseases, immunization against some of the most devastating diseases in the world remains an elusive goal.[153,154] Strategies for immunoprophylaxis against viral diseases include active prophylaxis conferred by vaccines and passive prophylaxis conferred by antibody-based preparations to protect an individual against a specific disease.[155] Vaccines are ineffective in those who cannot mount an effective immune response, such as the immunocompromised and elderly, necessitating an alternative approach to protection against infectious diseases.[156] Use of conventional vaccines against HIV in particular has remained impossible despite remarkable research efforts.[154] Therefore, as an alternative to vaccination, the field has turned towards viral vector-mediated gene transfer to induce host production and secretion of broadly neutralizing antibodies.[154] This approach, termed VIP, has been investigated for applications in human health and has been the subject of intense research and at least one clinical trial.[157] VIP requires transfection of non-hematopoietic cells with genes encoding the neutralizing antibody of interest and subsequent secretion of the monoclonal antibodies.[153,158] To facilitate gene transfer, pDNA has been investigated as part of many preventative measures against infectious and acquired diseases, including Human Immunodeficiency Virus (HIV).[159]

SPNPs represent a promising delivery system for immunoprophylaxis against HIV infection, as current viral vectors exhibit several efficacy issues. These include limited carrying capacity and inability to re-dose or administer a booster if the host has mounted an immune response to the vector.[160] Therefore, VIP necessitates an alternative delivery strategy. It would be advantageous to expand the SPNP gene delivery platform reported here towards this therapeutic goal.

VIP against HIV infection is a particularly appealing application of the SPNP pDNA delivery platform, as the efficacy of pre-exposure treatment suffers from a lack of adherence to the recommended treatment remgimens.[161] Delivery of a one-time SPNP-mediated VIP treatment would remove continued patient compliance from the equation. Additionally, due to the lack of antibodies specific to SPNPs following treatment in mice,[32] there is not a reason to believe that difficulty redosing, or utilizing this delivery system for another SPNP mediated VIP treatment would suffer from the same immunogenicity issues associated with viral vectors.

While VIP has been heavily investigated against HIV transmission, it can be extended towards malaria, dengue, hepatitis C, influenza, and other transmissible diseases that researchers have struggled to develop immunization or vaccines against.[153] As such, a SPNP delivery system capable of efficient non-viral VIP would serve as a broad platform with applications in many disease states.

Another potential use for SPNP mediated gene delivery in human health is targeted pDNA delivery to muscle cells to restore lost function. Restoring muscle function in skeletal muscle is of great interest as it is necessary to treat Duchenne's muscular dystrophy (DMD). Polyploid skeletal muscles represent a target for direct injection, and the causal gene in DMD has been estimated to be restored with as little as 4% of the wild type function, meaning a lower efficacy is needed to treat this disease than is typically expected.[162,163] This among other genetic diseases not listed here represent a promising target for SPNP mediated gene delivery.

Some consideration should be taken for the initial *in vitro* experimental design as it relates to the eventual organismal or human trials intended. VIP is performed *in vivo* on humanized mice and *in vitro* using HEK293T and other non-hematopoietic cells. HEK293Ts are a common choice as they represent an easily transfected and rapidly dividing cell type, which is beneficial for transfection and rapid secretion of the monoclonal antibodies. As another example, in this work HepG2 cells were used as a model cell line. Future work could utilize similar cells and study the effect of GalNAc targeting ligands on cellular uptake and eventual expression.

In general, both the SPNP formulation and experimental design can be easily modified to interrogate the disease state or environment of interest. Overall, the SPNP pDNA delivery platform is robust and represents a broad system that can be readily altered for application in different disease states.

6.7 Applications of Syringe Filtration to Synthetic Protein Nanoparticle Processing

In Chapter 5, a new method for processing SPNPs once they have been collected was presented. Processing the collected SPNPs via syringe filtration increased the repeatability of the SPNP sizes while removing the need for the user to make judgement calls during the centrifugal filtration (CF) process. This method also exhibited similar mass loss to the traditional CF process, while decreasing the processing time from 3 hours to approximately 15 minutes, a 90% reduction in processing time.

While the syringe filtration method was tested using Human Serum Albumin (HSA) based SPNPs crosslinked via an NHS ester, it can be readily adapted to other SPNPs and streamline SPNP processing to improve repeatability and reproducibility between users and batches. If the intention is to utilize different formulations of SPNPs, future work should first ensure that preliminary testing of syringe filtration with the new SPNP is done. The same conditions (pump rate, filter size) should be used and DLS spectra should be obtained for the intended carrier protein and crosslinking method. This will ensure that the mass loss is similar and that shearing of the SPNPs does not occur as seen with the 0.45 µm syringe filter, reported in Chapter 5. It is possible although unlikely that different proteins would respond differently to syringe filtration. It is more likely that different crosslinking methods would result in different SPNP populations, however, this might be intrinsic to the crosslinker. Nonetheless, preliminary testing should be done so that this method can be adapted with confidence to new SPNP formulations.

A natural extension of this work would be examination of cell viabilities, uptakes, and other biological outputs resulting from use of SPNPs processed with syringe filtration.

It is likely that different sized SPNP populations result in different cellular uptakes. It has been shown that nanoparticles with lower diameters, as seen in SPNPs that have been filtered, result in higher rates of endocytosis compared to larger diameter nanoparticle populations.[44] Therefore, it is likely that higher cellular uptake can be expected from syringe filtered SPNPs, which had smaller diameters, than SPNPs processed by CF. This might impact other biological outputs, and even on the required dose to have the intended effect, as more of the drug or gene could be entering the cells. For example, if the drugs encased in the SPNPs are cytotoxic, cell viability could decrease. Viabilities should be carefully monitored to avoid an unexpected increase in cytotoxicity.

Since cell viability and uptake depend on SPNP, cargo, and cell type, each scenario will require testing to understand any potential differences that syringe filtration imposes on the SPNPs. While preliminary testing needs to be done prior to utilizing the syringe filtered SPNPs in cell or animal work, the streamlined workflow presented here can improve repeatability and decrease hands-on time for SPNP processing. This method leads to less manipulation of the SPNPs and a higher degree of confidence in the SPNP product, which could be critical in future collaboration and *in vivo* studies.

6.8 Future Outlook

The work presented in this thesis was developed with the goal of understanding the formulation and the loading of pDNA carrying SPNPs to improve reporter gene expression. The loading information that is gained by application of the PBL strategy can be combined with intracellular tracking as mentioned previously, but also with the rational design strategy presented in Chapter 4. By combining technology established in Chapter

2 for loading quantification and Chapter 4 for formulation design, the SPNP delivery platform can be further examined, and the intracellular route interrogated. By elucidating the cellular path that the pDNA takes and determining stumbling blocks to efficient gene expression, the SPNP can be engineered to overcome these challenges, using the rational design strategies presented here to reach a SPNP formulation that maximizes the desired output.

The goal of DNA delivery is to move beyond reporter gene expression and ultimately achieve a therapeutic effect. Future work will be able to combine these technologies and the insight gained from this work to move towards delivery of a therapeutic DNA. Already, siRNA has been used in the Lahann Lab to mediate RNA interference and knock-down certain pathways at the mRNA level.[32,33] DNA has further knockdown utility, including delivery of CRISPR/Cas9 systems that generates work at the DNA level.[164] This can completely and permanently silence genes to cure diseases rather than treat them transiently. By engineering a SPNP that can induce significant reporter gene expression, these tools detailed in this work pave the way for achieving therapeutic delivery of DNA. Applications and barriers to doing so have been discussed here, along with the engineering considerations for formulating ne SPNPs based on the platform developed and presented in this thesis.

Overall, the work presented here establishes methods to formulate and quantify plasmid DNA-loading in SPNP delivery systems for gene delivery. pDNA loaded SPNPs have been fully characterized and the impact of altering the formulation on biological outputs has been examined. Foundational understanding is critical to applying and utilizing systems for ultimate clinical translation, and the work presented here contributes to doing so.

Appendices

Appendix A

Materials:

Reagents:

Human Serum Albumin, Alex Fluor 405 NHS Ester, polyethylenimine 25kDa, Ethylene Glycol, Anhydrous DMSO, Amicon Ultra-15 Centrifugal Filters, and 96-well flat bottom black walled plates were purchased from Sigma Aldrich (St. Louis, MO). 7.5% Sodium Bicarbonate Buffer was purchased from Thermo Fisher (Waltham, MA). UltraPure DNase/RNase-Free Distilled Water was purchased from Invitrogen (Waltham, MA). Dulbecco's phosphate-buffered saline (DPBS) was purchased from Gibco (Waltham, MA). O,O′-bis[2-(N-succinimidyl-succinylamino) ethyl]polyethylene glycol (NHS-PEG-NHS) with a molecular weight of 400 Da was purchased from NANOCS (New York, NY).

Instrumentation

A SpectraMax M5 plate reader from Molecular Devices (San Jose, CA) was used in these studies. A Qubit 4 Fluorometer, Molecular Probes Quant-iT Qubit dsDNA HS and dsDNA BR Assay Kits, Qubit Assay Tubes, Ultrapure DNA/RNAse free water were purchased from Invitrogen (Waltham, MA). A Thermo Fisher Nova 200 Nanolab SEM/FIB was used to capture micrographs of the SPNPs. A Discovery TGA from Texas

Instruments (New Castle, DE) was used for gravimetric analysis. A Zetasizer Nano ZS from Malvern Panalytical (Malvern, UK) was used to carry out particle size distribution measurements.

Analysis Software

ImageJ v1.53c was used for image analysis. Microsoft Excel 2020 was used for all data manipulation and for the general summary of statistics. GraphPad Prism v9.2.0 was used for presentation of graphs, linear calibration curves.

Methods

Generation of DPA Calibration Curve

For quantitative analysis of the DNA loaded SPNP, the diphenylamine assay was generated using the same dynamic range of unmodified plasmid DNA concentration as described above. The formulations for sample preparation are listed in the Cy3-DNA calibration generation section with no additional modification.

For absorbance measurement, a SpectraMax m5 plate reader was used for intensity reading with a black-walled 96-well plate with polystyrene bottom. At a sample to DPA reagent ratio of 1:2, a total of 150 µL was added to each well for absorbance reading simultaneously after a 4-hour incubation at 37°C. Absorbance readings at 595 nm were recorded and a plotted curve of optical density (O.D.) versus DNA concentration (ug/mL) was made.

A mathematical equation of the linear regression curve was calculated with GraphPad Prism and a goodness of fit can be evaluated with the r^2 value. Measurements were made with 3 repeated samples of each concentration and readings were made in triplicates to establish confidence in the linear regression and repeatability of the assay. The average and standard deviation are provided. The desired concentration of the DNA containing SPNP was back calculated through plugging the absorbance intensity back into the previously derived equation.

Determination of DNA Amount with DPA Assay

The diphenylamine assay prepared according to a protocol established by Burton et. al. Modifications were made accordingly to accommodate volume changes. Briefly, 0.75g of diphenylamine was first dissolved in 50 mL of acetic acid and 0.75 mL of concentrated sulfuric acid was added sequentially. The mixture was stored in the dark at room temperature. At time of use, premade aqueous acetaldehyde (16 mg/mL) was added to the mixture at a volume ratio of 1 aqueous acetaldehyde to 200 acid-diphenylamine mixture. Sample and the diphenylamine assay were mixed at a 1:2 ratio and were incubated at 37°C for 4 hours. Absorbance measurements were made with reading at 595 nm on a microplate reader.

Fluorescent Labeling of HSA with Alexa Fluor 405

For the purpose of imaging protein particles, a fluorescently labeled albumin was generated. In brief, 60.0 mg of human serum albumin (Sigma, A3782) was dissolved in 25 mL of 0.1 M sodium bicarbonate buffer (pH 8.3). Once completely dissolved, 0.5 mL of a previously prepared solution, consisting of Alexa Fluor 405 NHS Ester (Sigma, A30000) dissolved in anhydrous DMSO (10 mg/mL), was added, and mixed well. The resulting mixture was incubated in dark conditions, at room temperature, for 2h under constant rotation. Upon completion of the reaction, the removal of reaction byproducts and unreacted dye molecules was performed through a series of buffer exchange steps. The solution was split and transferred to two Amicon Ultra-15 (30 kDa MWCO) centrifugal filter devices. Filtration was performed by centrifuging the solution for at 4,000 rcf for a period of 1h. Once concentrated, the remaining solution was diluted with DNase/RNase-Free water before concentrating again. The filtration and buffer exchange steps were performed a total of three times to ensure complete removal of free dye molecules before characterization of the resulting conjugate was performed.

To characterize the resulting protein-dye conjugate and quantify the number of dye molecules per albumin, both dye and protein concentration of the resulting solution were determined independently. Protein concentration was determined using a Pierce 660nm Protein Assay. In parallel, Alexa Fluor 405 dye content was determined through fluorescent measurements (Ex/Em 395/425) compared against a previously generated calibration curve. Sample measurements were made at multiple dilution points within the linear range. Prior to introducing the resulting Albumin-405 to the jetting process, the final concentration was adjusted to 5 mg/mL in ultra-pure water, aliquoted for future use, and stored at -20°C.

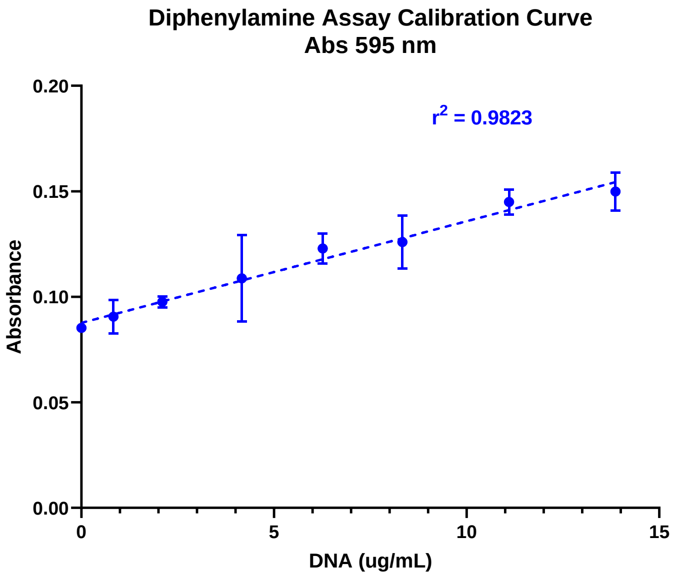

Figure A-. The DPA calibration curve used to calculate DNA content presented in Table 3 in the main body. The range of values and conditions (solvent system, DNA, HSA and PEI content) and the preparation method is identical to the calibration curve generated for fluorescent measurements (PBL).

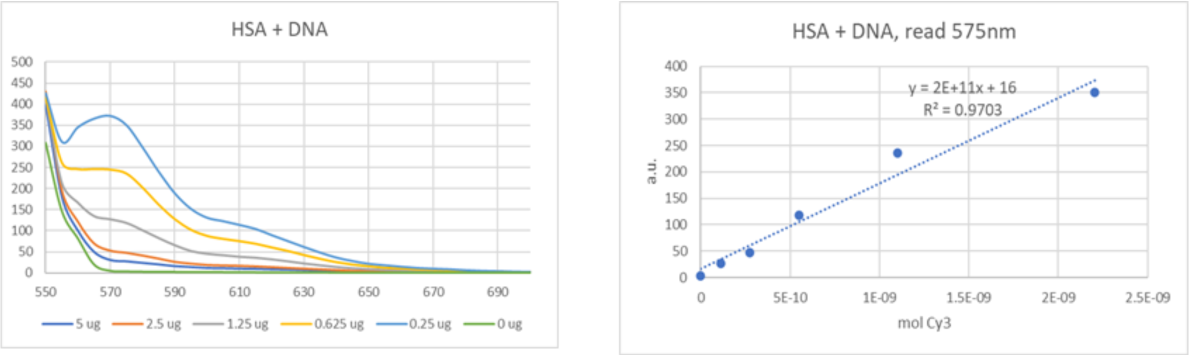

Figure A-2. Fluorescent spectra of varying Cy3-DNA amounts from 550-700nm step size 5 nm EX 520nm Cutoff Filter 530nm. Curve resulting from experiment with HSA + DNA in water.

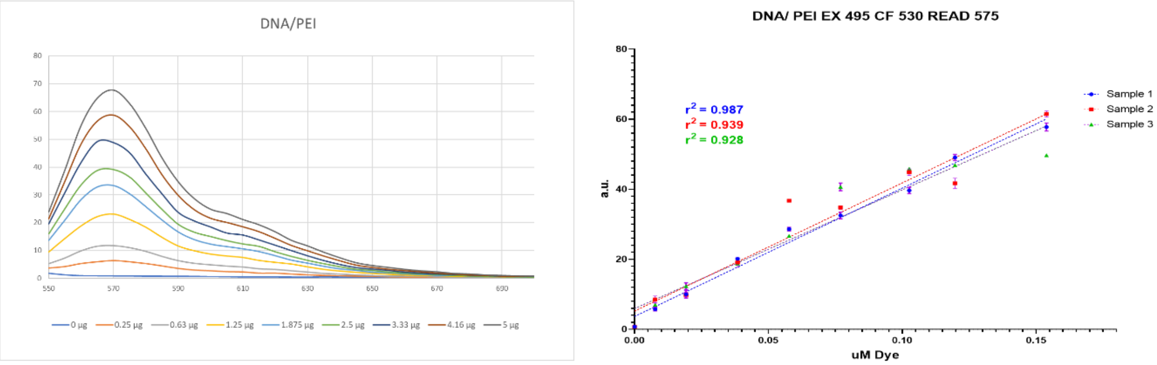

Figure A-3. Fluorescent spectra from 550-700nm step size 5 nm EX 520nm Cutoff Filter 530nm. Curve resulting from experiment with DNA and PEI in water

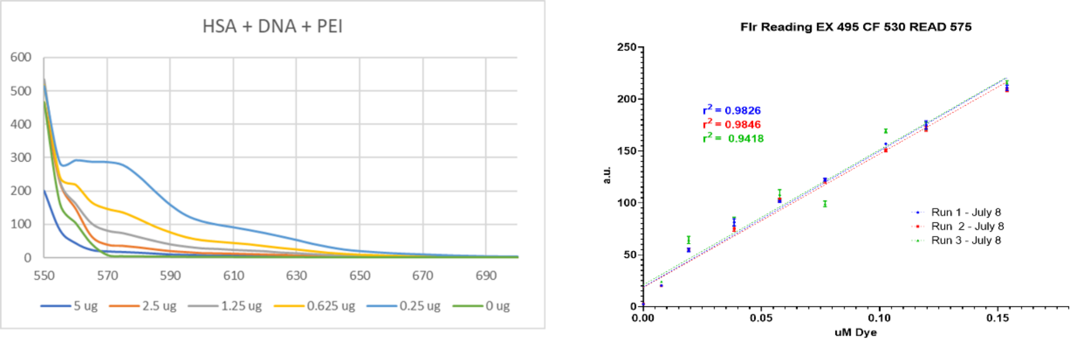

Figure A-4. Fluorescent spectra from 550-700nm step size 5 nm EX 520nm Cutoff Filter 530nm. Curve resulting from experiment with HSA + DNA + PEI in water.

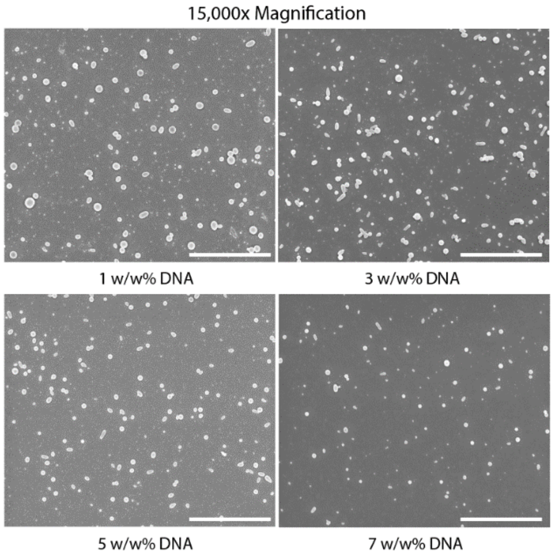

Figure A-5. Representative SEM micrographs of each formulation reported in the main text. For PSD analysis, n > 400 was used. Scalebar 3 µm.

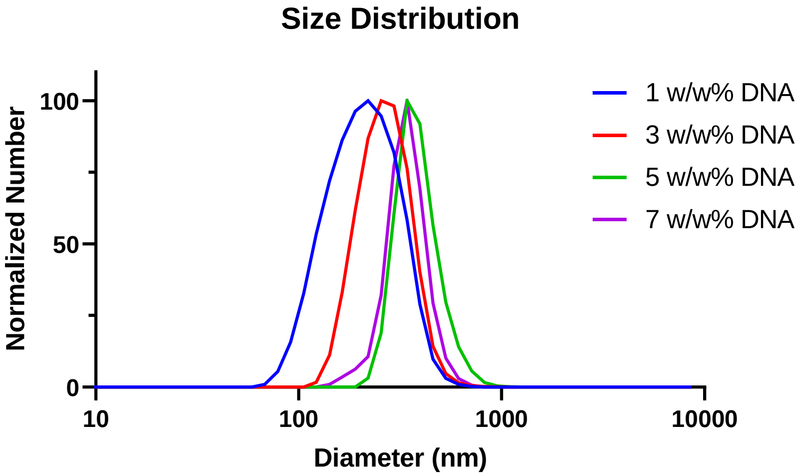

Figure A-6. Representative nDLS traces of the SPNPs analyzed in Table 3. Each trace is the average of 6 measurements

Appendix B

Presented here are the materials and methods for experiments reported in Chapter 4 of this thesis as well as Supplemental Figures generated as a result of experiments reported in Chapter 4.

Reagents:

Human Serum Albumin, Alex Fluor 405 NHS Ester, polyethylenimine 25kDa, Ethylene Glycol, Anhydrous DMSO, Amicon Ultra-15 Centrifugal Filters, and 96-well flat bottom black walled plates were purchased from Sigma Aldrich (St. Louis, MO). 7.5% Sodium Bicarbonate Buffer was purchased from Thermo Fisher (Waltham, MA). UltraPure DNase/RNase-Free Distilled Water was purchased from Invitrogen (Waltham, MA). Dulbecco's phosphate-buffered saline (DPBS), Trypsin EDTA (0.25%), Fetal Bovine Serum, and Penicillin-Streptomycin were purchased from Gibco (Waltham, MA). SYTOX™ Red Dead Cell Stain were purchased from Invitrogen (Waltham, MA). NsiI and BlpI restriction enzymes were purchased from New England Biolabs (Ipswich, MA). O,O′-bis[2-(N-succinimidyl-succinylamino) ethyl]polyethylene glycol (NHS-PEG-NHS) with a molecular weight of 400 Da was purchased from NANOCS (New York, NY). eGFP-pDNA was purchased from Plasmid Factory (Bielefeld, Germany). 96-well flat bottom black walled plates were purchased from Sigma Aldrich (St. Louis, MO).

Instrumentation

A SpectraMax m5 plate reader from Molecular Devices (San Jose, CA) was used in these studies. A Thermo Fisher Nova 200 Nanolab SEM/FIB was used to capture micrographs of the SPNPs. A Zetasizer Nano ZS from Malvern Panalytical (Malvern, UK) was used to carry out particle size distribution measurements. Flow cytometry measurements were taken using a CytoFLEX Flow Cytometer from Beckman Coulter (Brea, CA).

Analysis Software

Microsoft Excel 2020 was used for all data manipulation and for the general summary of statistics. GraphPad Prism v9.2.0 was used for presentation of graphs and fitting of linear calibration curves.

Methods

Determination of N/P Ratio – Gel Shift Assays

Control/Lane	pDNA Solution (μL)	100x PEI Dilution (μL)	UltraPure Water (μL)	Total (μL)	N/P Ratio
Ladder	0	0	0	25	n/a
Control	1	0	24.00	25	0
3	1	0.26	23.75	25	1
4	1	0.52	23.48	25	2
5	1	0.78	23.22	25	3
6	1	1.04	22.96	25	4
7	1	1.30	22.70	25	5
8	1	2.60	21.40	25	10
9	1	5.20	18.80	25	20
10	1	7.80	16.20	25	30

Table B-1 Sample preparation for gel shift assays

Representation of Prepared Synthetic Protein Nanoparticles on a Molar Basis

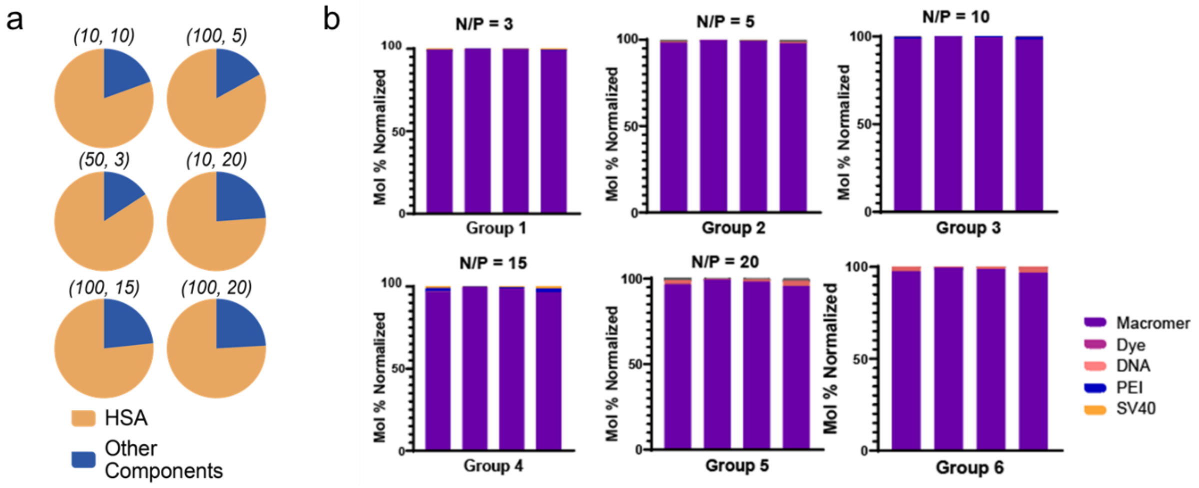

Figure B-1 The design space of SPNPs. (a) Pie charts indicating for each SPNP formulation the portion of HSA present on a mass basis. (b) Each SPNP formulation is presented as normalized to 100 mol% of the total particle without the presence of HSA.

Analysis of GFP Expression by Flow Cytometry

<table>
<tr><th>Sample</th><th colspan="2">Example Flow Result</th></tr>
<tr><td>Empty</td><td>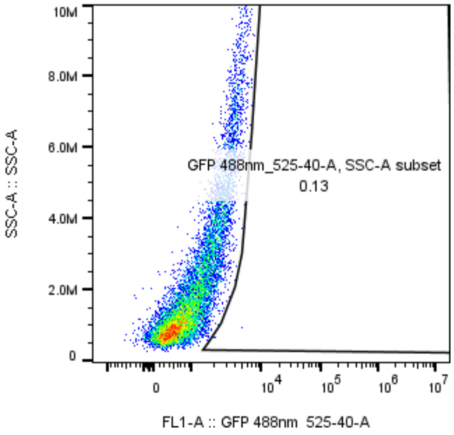
</td><td>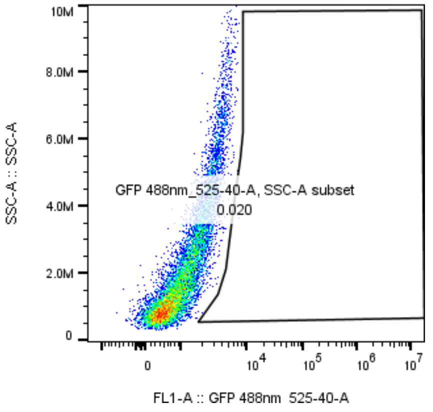
</td></tr>
</table>

(10, 10)	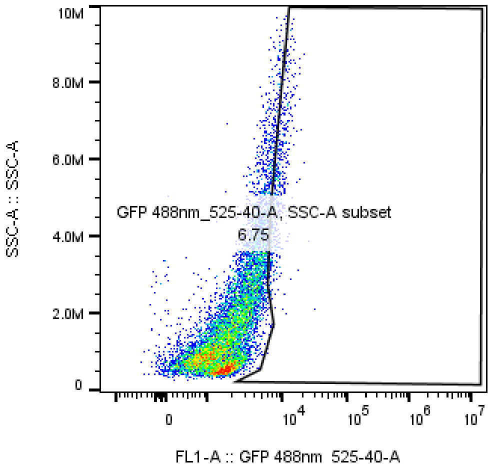	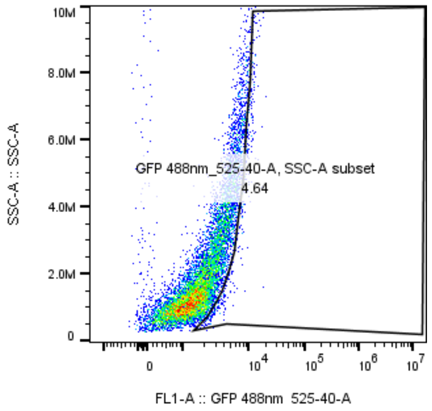
(100, 5)	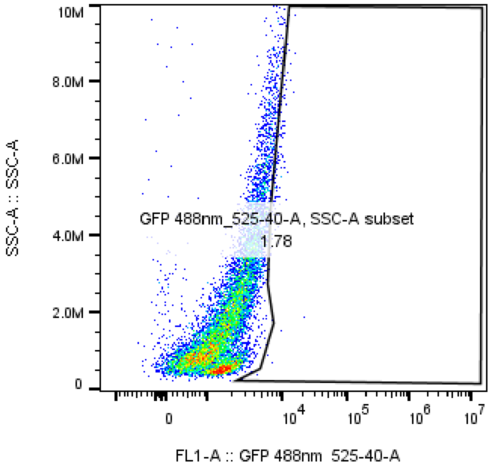	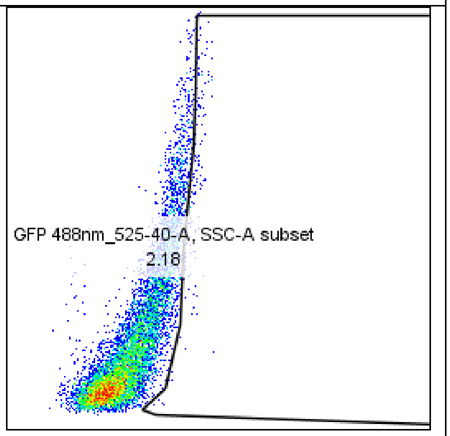
(50, 3)	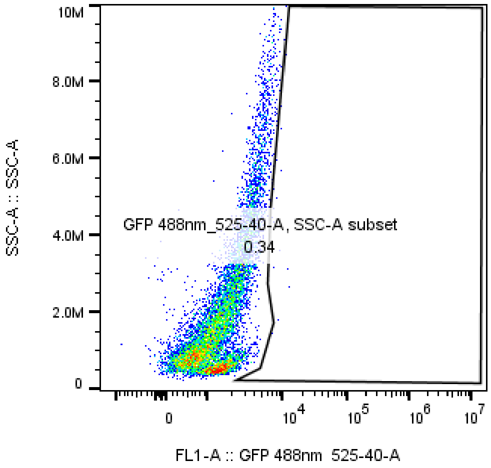	

(10, 20)	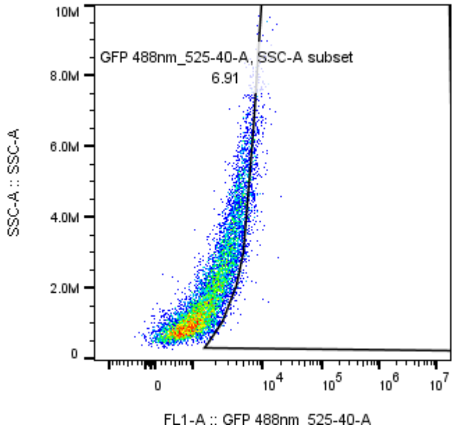	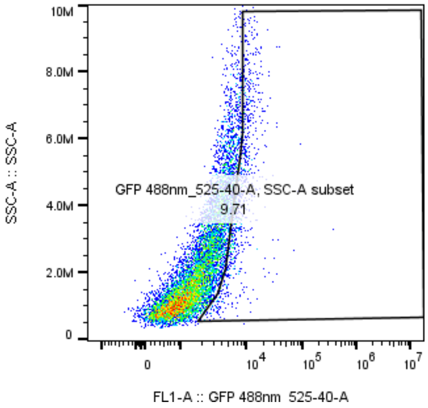
(100, 15)	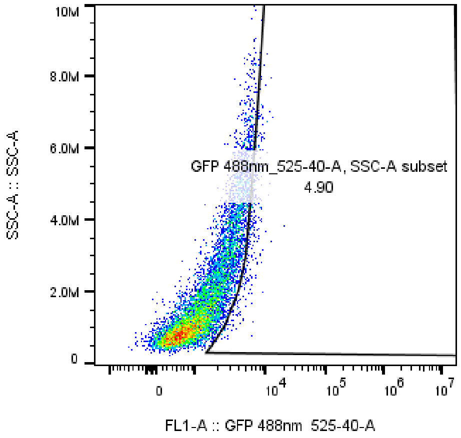	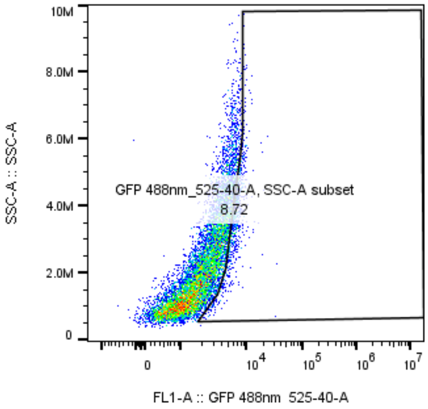
(100, 20)	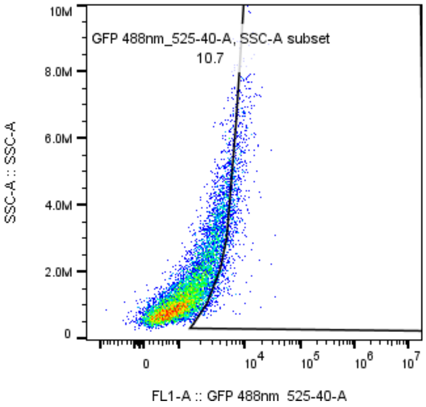	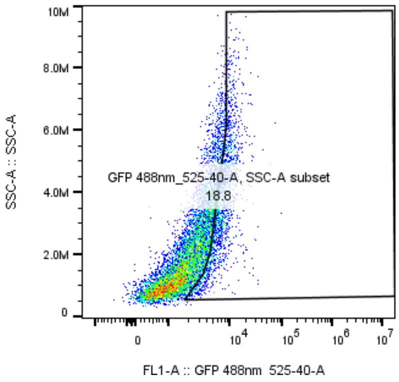

Lipo 2000	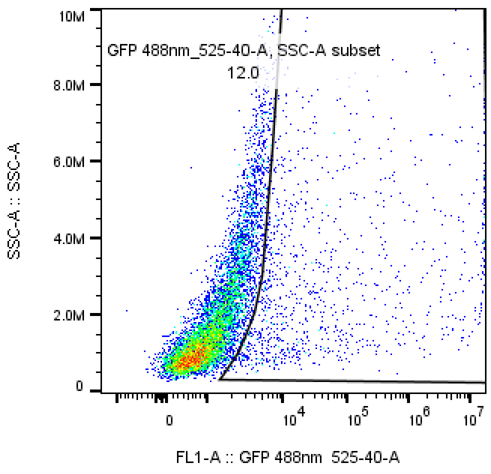	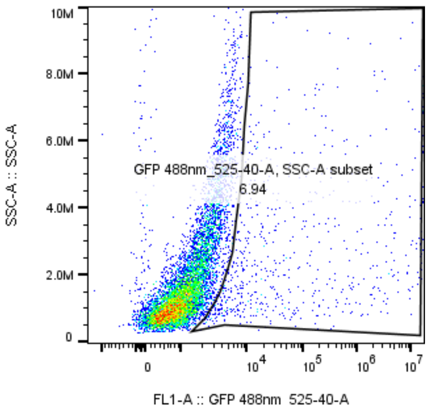

Figure B-**2**. Representative flow cytometry graphs gating for GFP .

Appendix C

Self-Healing Supramolecular Hydrogels for Tissue Engineering Applications

The material in this section has been adapted with minor modifications from the following articles:

L. Saunders, P.X. Ma, ”Self-Healing Supramolecular Hydrogels for Tissue Engineering Applications*” Macromol. Biosci.* 2019, 19, 1800313

C.1 Introduction

In recent decades, increasing demand for biomaterials capable of aiding in regeneration or replacement of damaged tissue motivated the development of new tissue engineering constructs.[165] Due to their unique biocompatibility and biomimetic properties, hydrogels have been widely used in many biomedical applications such as contact lenses, wound dressings, and drug delivery vehicles.[166–168] The properties of hydrogels follow from their structure: namely their highly swollen, hydrophilic 3D cross-linked polymer network that may be either chemically or physically cross-linked to form a material that mimics advantageous properties of the highly hydrated extracellular matrix (ECM) and facilitates nutrient and oxygen transport due to its porous structure.[167,169]

While hydrogels offer many useful properties, the permanent covalent cross-links in traditional hydrogels are often not ideal for tissue engineering applications, considering the dynamic nature of tissue regeneration and integration with the host. Tissue engineering has yet to achieve anticipated clinical impact, largely due to a failure to integrate with existing vasculature and host tissue.[170] The irreversible covalent cross-links result in a material that is unable to heal after breaking, making such hydrogels ineffective in sustaining their function or maintaining their desired mechanical properties.[171,172] Covalent cross-links also constrain the movement of polymer chains in the hydrogel bulk, decreasing their flexibility and creating an elastic material, which contrasts with the viscoelastic and deformable ECM of native tissue.[173] While hydrogels formed by dynamic covalent cross-links have been investigated for biomedical applications, the reversibility of the linkages can rely on harsh conditions such as elevated temperatures, low pH, UV light, or a combination of these.[174–182] Such hydrogels are therefore limited to applications that utilize their harsher cross-linking conditions such as cancer therapy, where pH sensitive gelation can occur only in the acidic tumor microenvironment.[183] The tissue-specific microenvironment is an important design component of effective tissue engineering scaffolds as cells are constantly interacting with, remodeling, and moving through the ECM to perform normal functions.[184–186] Recent work has looked into dynamic covalent chemistries including Schiff's Base, imine cross-links, and disulfide exchange that would allow for cellular remodeling and tunable cleavage of the hydrazone or disulfide linkers.[172,173,179,187–189] These gels undergo dynamic chemical degradation while maintaining the bulk properties of the hydrogel and have been used primarily as self-healing 3D cell culture substrates. These materials often exhibit slower reversibility than their supramolecular counterparts and can require the addition of a catalyst, but they have still been used for 3D printing as their shear-thinning and self-healing behavior makes them desirable candidates for extrusion-based printing.[188,190,191] Compared to permanently cross-linked hydrogels, the incorporation of cells into dynamic hydrogels is relatively new, and work remains to be done toward the development of adaptable covalent hydrogels for tissue engineering[173].

To achieve properties that remain largely unrealized by covalently cross-linked hydrogels such as self-healing and reversible linkages, supramolecular hydrogels have been developed that combine the unique advantages of hydrogels and supramolecular chemistry.[192] The properties of these hydrogels follow from the dynamic nature of their constituents: supramolecular bonding motifs that rely on hydrogen bonding, electrostatic interactions, π–π bonding, host–guest interactions, hydrophobic interactions, or metal coordination act as dynamic cross-links between hydrophilic polymers to form hydrogels.[193–199] The variety of supramolecular building blocks offers many tools for development of a diverse range of biomaterials that offer promise as scaffolds for tissue engineering.[200,201]

This review will focus on important work that has been done toward development of self-healing supramolecular hydrogels for tissue engineering applications, with emphasis on supramolecular bonding motifs used for hydrogel formation and recent advances toward their use in regenerative medicine. We will conclude by looking forward at important challenges facing the development of ideal hydrogels as both scaffolds and drug or biologic delivery vehicles to regenerate, maintain, or improve lost or damaged tissue.

C.2 Supramolecular Bonding Motifs

C.2.1 Motivation

To advance the field of tissue engineering, new biomaterials capable of effective, controlled delivery of drugs and biologics, and recapitulation of native tissue properties must be developed. Cells exist in vivo within a dynamic, 3D matrix consisting of polysaccharides, ECM biopolymers (proteoglycans and proteins), and soluble factors secreted by nearby cells.[202] This 3D environment is critical to normal cell function, as it enables important cell behaviors including cell adhesion, proliferation, migration, and differentiation.[202–206]

Hydrogels have a long history as tools for tissue regeneration and 3D cell culture as they may be engineered to mimic the desired aspects of the native local ECM depending on their intended usage. Early attempts at recapitulation of the ECM included hydrolytically cleavable and matrix metalloproteinase (MMP)-cleavable permanently cross-linked but dynamic hydrogels. For example, a dynamic MMP-cleavable hydrogel was developed to facilitate cell invasion and render the polymer networks degradable by cells to mimic this feature in native tissue, however the enzymatic cleavage of the cross-links is permanent, leading to degradation of the bulk material.[207,208] It was shown that both hydrolytically and enzymatically degradable hydrogels were favorable over their static covalent counterparts in in vitro cartilage regeneration.[209] Later efforts toward development of dynamic systems included a permanently cross-linked, pH-switchable hydrogel to enable repeated self-healing via hydrogen bonding, however, the gelation occurs at $pH \leq 3$ and is therefore limited in its application to tissue engineering.[210]

Supramolecular hydrogels have emerged as a promising tool for tissue regeneration as they can be biocompatible and recapitulate the viscoelastic nature of the ECM better than their elastic, covalently cross-linked counterparts due to the presence of dynamic linkages. The resulting viscoelastic and dynamic behavior of these linkages are responsible for other advantages such as self-healing and injectability. In addition to offering advantageous scaffolding for tissue engineering, supramolecular hydrogels can be engineered to effectively encapsulate, sequester, protect, and deliver cells, biologics, and drugs for regenerative medicine.

Of particular interest are supramolecular hydrogels that can self-heal after damage either spontaneously or in the presence of a physiological stimulus.[210] This characteristic extends the lifetime of materials and makes them ideal candidates for applications involving repeated mechanical stress or injection.[199,211,212] The dynamic nature of reversible cross-links responsible for self-healing behavior also results in shear-thinning (decrease in viscosity as shear stress increases) behavior, leading to injectable hydrogels which have recently been heavily investigated, as they represent a critical step toward less invasive delivery of therapies.[213,214] The properties of self-healing supramolecular hydrogels may be selected for and tuned by careful choice of a hydrophilic polymer and the supramolecular bonding motif utilized as a physical cross-linker (Table 5-1). Ideally, hydrogels for tissue engineering should enable cell infiltration as well as encapsulate and deliver cells and biologics, and be able to autonomously, rapidly, and repeatedly heal in situ at physiological conditions.[215] The most important supramolecular bonding motifs used in hydrogel formation for tissue engineering applications, with an emphasis on recent advances, are described below.

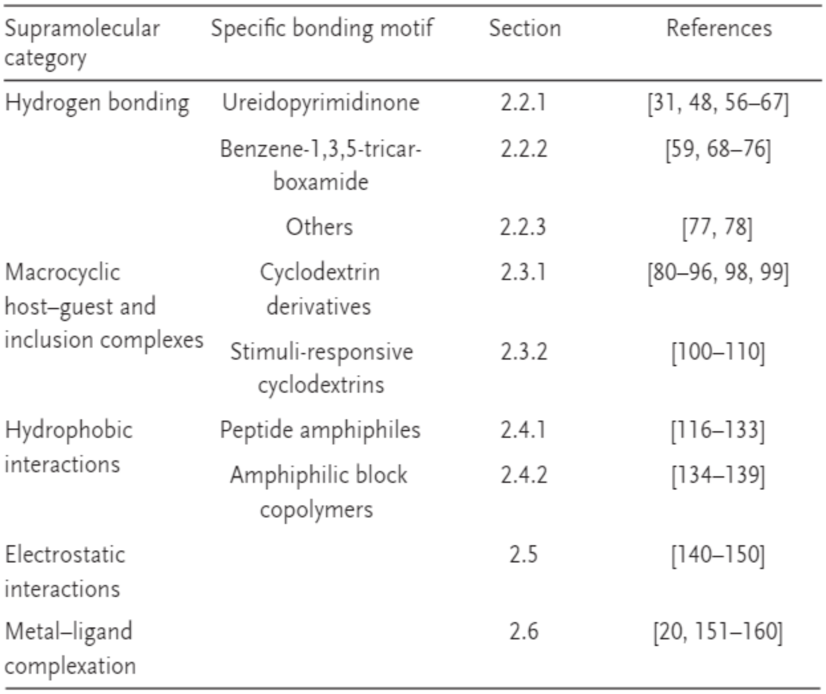

Supramolecular category	Specific bonding motif	Section	References
Hydrogen bonding	Ureidopyrimidinone	2.2.1	[31, 48, 56–67]
	Benzene-1,3,5-tricarboxamide	2.2.2	[59, 68–76]
	Others	2.2.3	[77, 78]
Macrocyclic host–guest and inclusion complexes	Cyclodextrin derivatives	2.3.1	[80–96, 98, 99]
	Stimuli-responsive cyclodextrins	2.3.2	[100–110]
Hydrophobic interactions	Peptide amphiphiles	2.4.1	[116–133]
	Amphiphilic block copolymers	2.4.2	[134–139]
Electrostatic interactions		2.5	[140–150]
Metal–ligand complexation		2.6	[20, 151–160]

Table C- 1. The categories of supramolecular interactions and the specific bonding motifs covered in this review.

C.2 Hydrogen Bonding Motifs

Hydrogen bonding is an important tool for self-assembly in biological systems as it is responsible for nucleobase pairing in DNA and RNA as well as the 3D assembly of proteins.[216] While the strength of a single hydrogen ‘bond' is relatively weak compared to covalent and some other non-covalent interactions, multivalent molecules greatly increase the degree of association possible between supramolecular moieties.[217] In fact, the cooperative effect of hydrogen bonding is responsible for some of the toughest covalent materials known, including Kevlar and silk.[218,219] Hydrogen bonding has also been utilized to great effect to generate self-healing permanently cross-linked hydrogels, however as was mentioned, the cross-linking occurs at a low pH and therefore is not useful in tissue engineering.[210]

C.2.1 Ureidopyrimidinone

Multiple hydrogen bonding motifs such as the widely reported quadruple hydrogen bonding motif ureidopyrimidinone (UPy), first described in a pioneering work in the 1990s, have been widely utilized in supramolecular hydrogels as a driving force for hydrogel formation.[195,220,221] Multiple hydrogen bonding units act as both hydrogen bond donors and acceptors and intrinsically increase the concentration of hydrogen bonding motifs in solution, leading to increased association between supramolecular building blocks. To achieve hydrogel formation in an aqueous environment, inter- and intramolecular effects must overcome water competition by either increasing the functionality per molecule, the molecule concentration, or using a combination of driving forces. Hydrogel formation is realized when a high enough association constant between supramolecular units is reached. Above a critical concentration, hydrogen bonding, hydrophobic spacers (which protect the hydrogen bonding groups from the solvent), and p−p stacking combine to combat competitive water and drive hydrogel formation.[222–225]

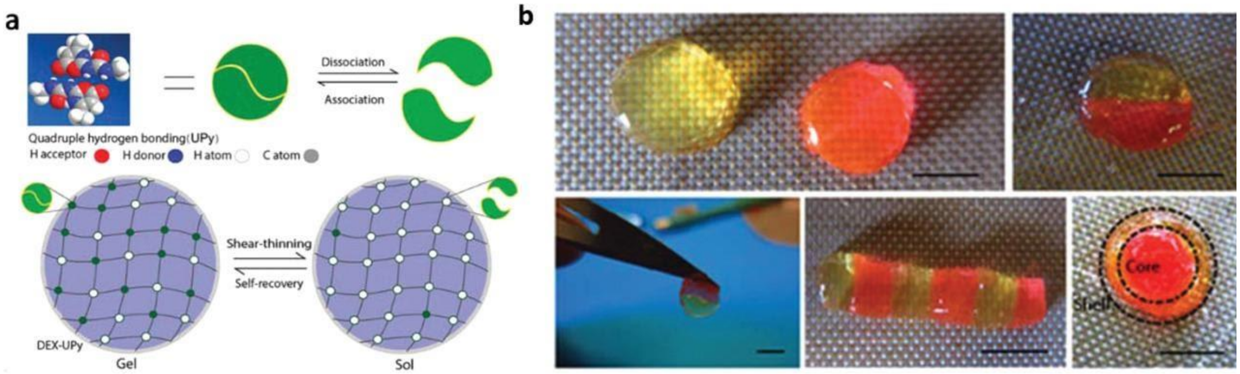

Figure C-1. Design of a Dextran-Ureidopyrimidinone (Dex-Upy) hydrogel for multi-tissue regeneration. a) Schematic illustration of Dex-UPy hydrogel formation and the mechanisms of the shear-thinning and self-recovery properties. Top: multiple hydrogen bonds of UPy and their dynamic interactions. Bottom: hydrogel network formation through UPy hydrogen bonds, the shear-thinning under shear stress and self-recovering of the hydrogel. b) Self-integration of the hydrogel pieces to form various structures. Some hydrogel disks were dyed pink with rhodamine and the others were left with the original light-yellow color to visualize the interfaces. Scale bar = 5 mm. Adapted with permission.181 Copyright 2015, Wiley.

Early work on supramolecular polymer networks formed through UPy interactions found that while they exhibited viscoelasticity and shear-thinning behavior, they eroded rapidly in aqueous environments due to oligomer dissociation, making them unfavorable materials for stable hydrogels.[226–228] More recently, work has been done on preparation of biocompatible UPy-based hydrogels that are capable of autonomous and spontaneous self-assembly at physiologically relevant conditions for tissue engineering purposes.[199]

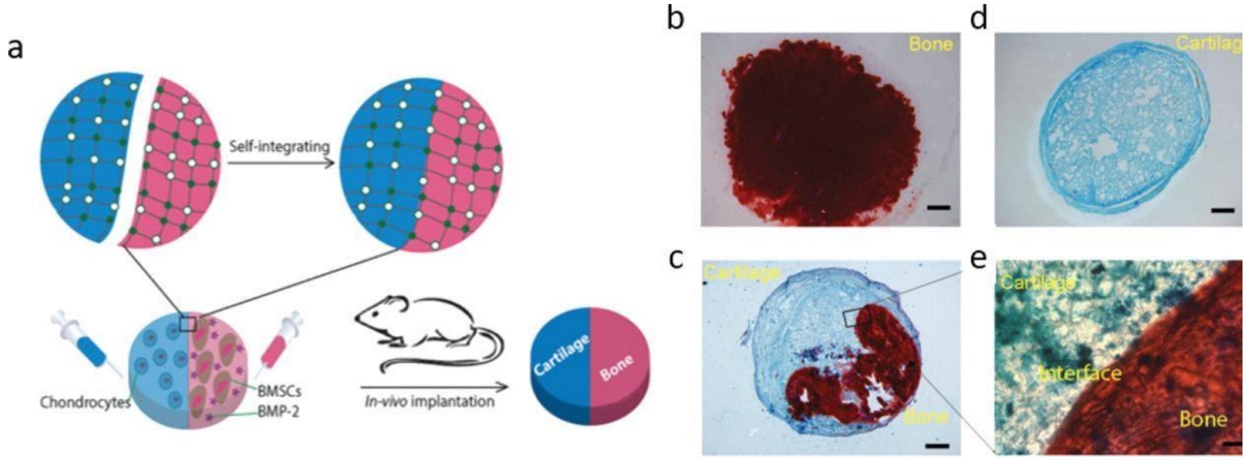

Figure C-2. In vivo testing of Dextran-Ureidopyrimidinone (Dex-Upy) hydrogel for bone and cartilage tissue regeneration. a) Schematic illustration of self-integration and the application in cartilage–bone tissue complex regeneration. Hydrogels encapsulating chondrocytes (blue) and Bone Marrow Stromal Cells (BMSCs)/Bone Morphogenetic Protein 2 (BMP-2) (red) were integrated into a construct and then implanted subcutaneously in a nude mouse to form the cartilage–bone tissue complex. b–e) Subcutaneous implantation of the cell-gel constructs. b) A section of BMSCs/BMP-2 only group, stained with Alizarin red (positive staining represents mineralized bone tissue). c) A section of chondrocytes only group, stained with Alcian blue (positive staining represents cartilage tissue). d) A section of the self-integrated group, stained with both Alizarin red and Alcian blue. e) A magnified image of the interface region of image 'c'. Adapted with permission.[199] Copyright 2015, Wiley

Minimally invasive injectable hydrogels capable of carrying growth factors and cells offer an attractive route to regenerate injured tissues. Injectable, self-healing supramolecular hydrogels utilizing UPy interactions have been used as biologic carriers and cell-delivery systems, and have been studied in vivo as minimally invasive protein delivery systems for soft tissues including kidney, and cardiac regeneration after injury.[199,225,228,229] For example, a pH-switchable, self-healing UPy-modified polyethylene glycol (PEG) hydrogel was delivered to the myocardium via local catheter injection to fast-release growth factors to reduce infarct size and subsequently for sustained-release of angiogenic factors to promote cardiac regeneration in a chronic infarct pig model.[229,230] These hydrogels are also useful for hard tissue engineering such as bone and cartilage regeneration.[199] In contrast to the majority of hydrogels that utilize telechelic

UPy units to induce cross-linking a dextran-based hydrogel with multiple pendant UPy units per chain was developed as a cell carrier and drug delivery system that does not require the addition of hydrophobic spacers for gelation. This system has been used to carry chondrocytes, bone marrow stem cells, and bone morphogenetic protein 2 (BMP-2) in an integrated construct to induce seamless osteochondral tissue complex regeneration in an in vivo mouse model (**Figure C-1**).[199] Its self-healing and shear-thinning nature allows possible cell migration and dynamic tissue modeling/remodeling following injection, and it represents an important step toward clinically relevant self-healing hydrogels for multi-tissue organ regeneration. (**Figure C-2**).

Another approach to generating shear-thinning supramolecular hydrogels is incorporating UPy modified with bulky, hydrophobic adamantyl groups, instead of alkyl spacers, to create “hydrophobic pockets” that shield the hydrogen bonds from solvent interactions and act to stabilize the structure, resulting in a self-healing and viscoelastic hydrogel that retains its rheological characteristics post injection.[231] This material is likely nontoxic but its suitability for tissue engineering may be limited due to rapid erosion because of progressive solubilization in highly aqueous environments and requires further testing.

C.2.2 Benzene-1,3,5-Tricarboxamide

More recently, benzene-1,3,5-tricarboxamide (BTA) has been recognized as a useful multiple hydrogen bonding unit for formation of supramolecular hydrogels.[232,233] BTA is a disk-shaped molecule functionalized with hydrophobic alkyl spacers and oligo(ethylene glycols) to increase solubility in polar solvents, such as water.[232] In water, BTA uses a combination of its threefold hydrogen bonding, protective hydrophobic pocket, and π–π interactions between the benzene rings to self-assemble into helical fibers (**Figure C-3**).[234,235] At high enough concentrations, BTA-based hydrogels form as a result of cross-linking of telechelic BTAs, and much like UPy-based hydrogels, are very sensitive to the ratio between hydrophobic and hydrophilic spacers.[233,234,236] Recently, this method of self-assembly has received increased attention, and has been combined with principles of DNA-origami to enable precise control over the spatial distribution and recruitment of proteins in adaptive scaffolds. Most recently, self-assembly of BTA monomers were used to form 1D supramolecular polymers that allow facile incorporation of various and DNA-functionalized BTA monomers that enabled efficient and dynamic control of protein activity along the polymer.[236–239] Functional BTAs have been incorporated into hydrogels for siRNA capture that represent a versatile platform for further development of various functionalized BTA polymers.[240] While promising and well characterized, these materials have yet to be tested in vitro for cytotoxicity and have not been developed toward use in regenerative medicine.

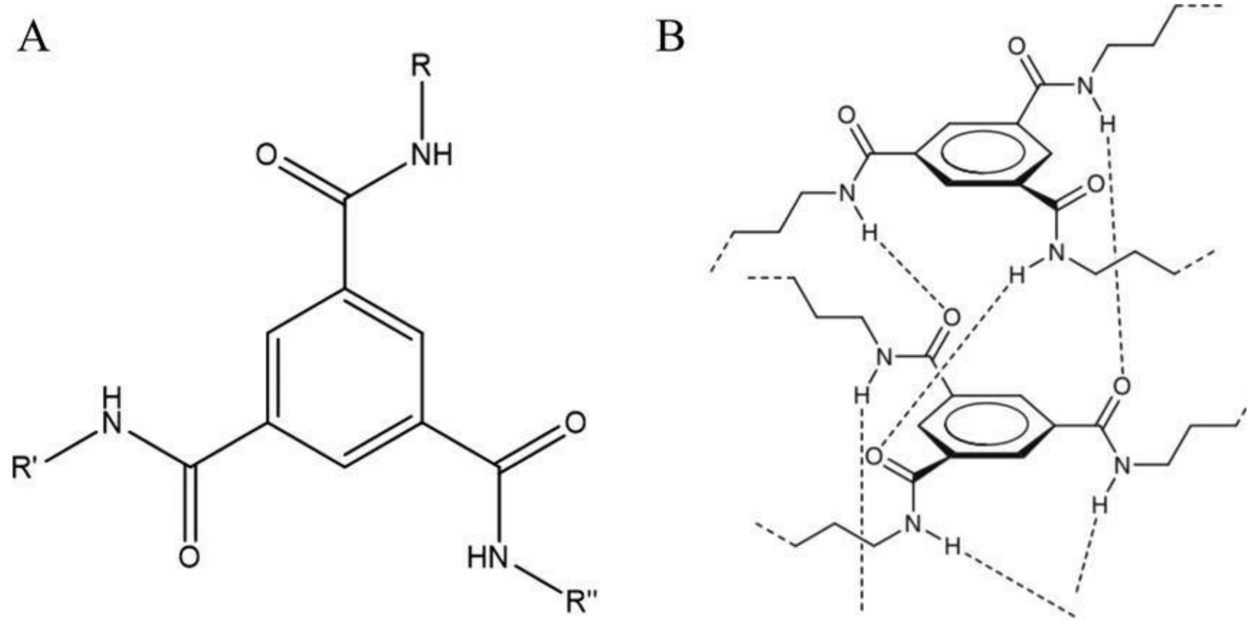

Figure C-3. A) Structure of Benzene-1,3,5-Tricarboxamide (BTA). R,R′R″ are alkyl chains/other substituents. B) Threefold hydrogen intermolecular bonding and helical assembly of BTA. Figure Part B adapted with permission.71 Copyright 2009, American Chemical Society

C.2.3 Other Hydrogen Bonding Motifs

Poly(vinyl alcohol) may also form pH-sensitive self-healing hydrogels based on hydrogen bonding and, to a lesser degree, hydrophobic interactions.[241] These materials do not retain their mechanical properties upon re-integration, but hold promise for drug delivery systems for cancer therapy, and require further investigation.[242] While non-UPy hydrogen bonding moieties remain largely un-utilized in tissue engineering applications, they offer alternative routes to formation of self-healing hydrogels, and the novel chemistries described here hold promise for advancing the field in new directions.

C.2.4 Macrocyclic Host–Guest Interactions and Inclusion Complexes

One of the most studied non-covalent methods for formation of supramolecular hydrogels is host–guest interactions based on macrocyclic compounds such as cyclodextrins (CDs), cucurbit[n]urils, crown ethers, catenanes, and cyclophanes. This review will focus on self-healing supramolecular hydrogels based on CDs and their derivatives. A comprehensive review of supramolecular host–guest systems for biological applications can be found in the literature.[243,244]

2.3 Cyclodextrin Derivatives

CDs are a family of oligosaccharides first discovered in the late nineteenth century and have a long history of use in biological applications due to their superior biocompatibility, unique inclusion capability, and ease of functionalization.[245–247] They have a truncated 3D cone shape with a hollow, tapered inner cavity and a fixed length (0.79 nm).[248] The width of CDs may be increased with the number of glucose repeat units, connected by α-1,4 glycosidic linkages (**Figure C-5**).[244] Since their discovery, α-, β-, and γ-CDs, composed of 6, 7, and 8 glucose units respectively, have emerged as the most commonly used members of the CD family.[244]

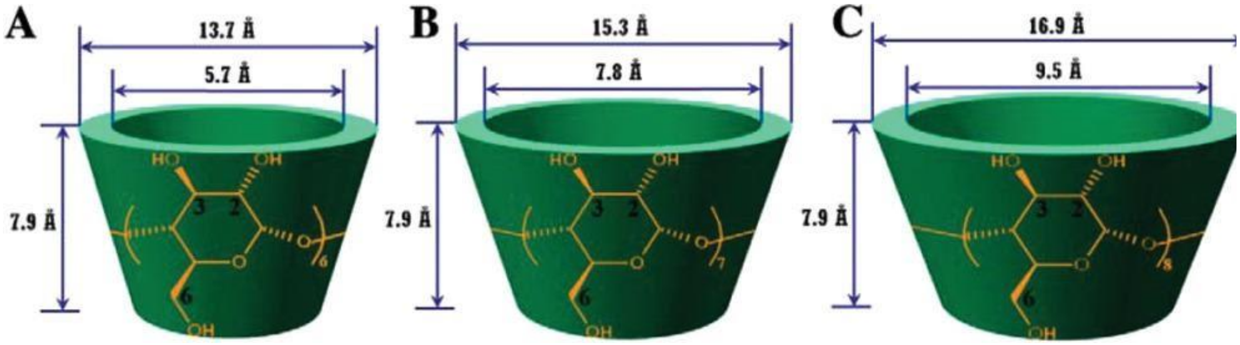

Figure C-4. Molecular structures and dimensions of various cyclodextrins (CDs): A, α-CD; B, β-CD; and C, γ-CD. Adapted with permission.226 Copyright 2013, Elsevier B.V

Members of the CD family have been successfully used as building blocks for self-healing hydrogels capable of stimuli-responsive self-assembly based on host–guest interactions between CDs and polymers.[248] Most often, poly(ethylene oxides) or block copolymers are used to further strengthen the hydrogels with hydrophobic segments that experience intermolecular hydrophobic interactions.[249,250] These supramolecular hydrogels have also been incorporated with covalent bonding to form materials systems with unique chemistry not seen in other supramolecular systems.[251] High molecular weight PEG was first reported to be able to form inclusion complexes with α-CD to assemble into supramolecular hydrogels.[252] Since then, the method of threading CDs onto linear hydrophilic polymers to form a hydrogel has been used to create supramolecular hydrogels (**Figure C-4**).[253–255] The dominant driving force in most host–guest systems are hydrophobic interactions that combat competitive water to drive self-assembly. Aside from inclusion complex formation, supramolecular hydrogels have been formed through co-assembling hydrophobically-modified polymers with polymers containing pendant CDs (**Figure C-5**).[249]

Another promising strategy is the preparation of supramolecular ‘monomers' with host–guest functionality and subsequent polymerization using various techniques. Host- and guest-containing CD monomers were polymerized via radical polymerization to form poly(acrylamide) chains which then formed inclusion complexes with CDs from nearby polymer chains to assemble a self-healing hydrogel network.[256] Although the cross-linking conditions are mild, and it exhibits an unusual ability to retain its mechanical integrity upon complete rejoining, acrylamide monomers are highly cytotoxic, so the utility of the hydrogel may be limited.[257] More recently, a modified β-CD host molecule was developed that forms an inclusion complex to make three-arm host–guest supramolecules.[258] This ‘monomer' unit was subsequently polymerized using UV light, creating a noncytotoxic self-healing hydrogel due to reversible self-integration of the free supramolecular host–guest units.[257] These hydrogels have been tested in soft tissue engineering but have yet to be translated to in vivo studies. In another promising application toward soft tissue engineering, a hyaluronic acid-adamantane and β-CD hydrogel construct were tested with secondary autonomous covalent cross-linking for regeneration of myocardial tissue

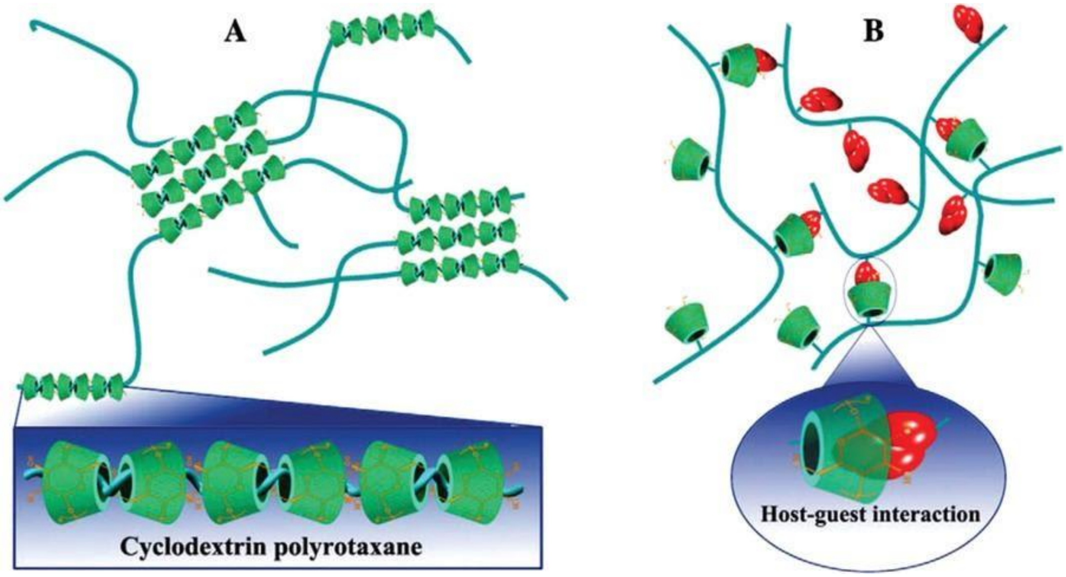

Figure C-5. Two different approaches for utilizing host–guest interactions to form supramolecular hydrogels. A) Fabrication of hydrogels based on inclusion complexes between CDs and various polymers that can thread into CD cavities. B) Supramolecular hydrogels formed by physical cross-linking through host–guest interactions between CD-containing polymers and hydrophobically modified polymers. Adapted with permission.[244] Copyright 2013, Elsevier B.V

post infarct.[259] After injection, this material acted as a support scaffold after injury and significantly decreased the infarct size while increasing cardiac function in an in vivo mouse model.

CD-containing supramolecular hydrogels are promising alternatives to covalently cross-linked hydrogels as injectable materials for drug and gene delivery. Many hydrogels that require covalent cross-linking for gelation are limited in application as they are not injectable, and it is time-consuming and inefficient to incorporate drugs by sorption, limiting the loading.[260] Additionally, it can require delicate bioactive agents such as drugs, proteins, RNAs, and DNAs to be exposed to organic solvents which may alter their chemical integrity.[260] Therefore, the development of a system capable of simultaneous gelation and drug loading in aqueous environment without covalent cross-linking is highly desired. One such system uses supramolecular hydrogel formed by CD-polymer inclusion complexes has been developed as an injectable drug delivery device, but work remains to be done toward its in vivo usage.[261]

Given the biocompatibility, shear-thinning, and self-healing nature of CD-based hydrogels, it is logical to extend their use toward 3D bioprinting. 3D bioprinting combines cells with a shear-thinning and self-recovering hydrogel to mimic native tissue characteristics and has received increased attention in recent years. A host–guest hydrogel using hyaluronate modified with adamantane and β-CD was developed that self-assembles into a shear-thinning hydrogel.[259] To increase its long-term stability and profusion, this hydrogel may be designed to undergo a secondary covalent UV cross-linking while maintaining its injectability. This system is an exciting step toward 3D bioprinting for tissue regeneration, as it was shown to have high (>90%) cell viability and the incorporation of cells did not disrupt or alter the printing process besides necessitating sterility. In the coming years, the use of self-healing supramolecular hydrogels will continue to develop and further bioprinting for tissue engineering.

C.2.3.2 Stimuli-Responsive Cyclodextrin Derivatives

In addition to autonomous assembly via inclusion complex formation, CDs can be utilized in various self-healing stimuli-responsive applications including thermo-responsive, redox, and photo-switching, leading to interesting properties such as shape-memory hydrogels and precise spatiotemporal control over size and stiffness of the hydrogel.[262,263] Stimuli-responsive CDs are useful in the construction of tissue engineering complexes (scaffold, cells, and/or signaling molecules) with various applications including engineering artificial muscle, cardiac tissue regeneration, anticancer drug delivery, and delivery of biologics.[264–267] These functionalities have been used toward development of ‘smart' hydrogels that respond to their environment, enabling better drug delivery and tissue mimicry. Ferrocene (FC) and its derivatives are widely used as redox-responsive molecules in supramolecular chemistry applications, adding stimuli-responsiveness while preserving the bulk properties.[268] For example, a self-healing supramolecular hydrogel where poly(acrylic acid) (PAA) modified with β-CD and a PAA-FC guest polymer undergoes redox-responsive self-healing based on formation of inclusion complexes has been reported.[269] This work is promising for future applications in stimuli-responsive drug delivery to tissues with a low local pH such as tumors, although cell toxicity and drug encapsulation have not been verified.

Separately, a noncytotoxic hydrogel system that is dually electrochemical and redox responsive was synthesized via formation of host–guest interactions between β-CD and FC and exhibits rapid self-healing capabilities.[270] This work is promising, but may be improved by incorporating controlled drug or biologic delivery systems, as is often required for effective tissue regeneration. Inclusion complexes formed by trans-azobenzene and β-CD as a photo-switchable cross-linker have been used to create a dextran-based hydrogel system for light controlled release of DNA and proteins.[267] Azobenzene is a photo-sensitive moiety that enables reversible sol–gel transitions, and although it remains largely unutilized in tissue engineering applications, it was shown in this work to be part of a system that was not harmful to biologics.[271,272] While UV irradiation may be harmful to tissues, the tight spatiotemporal control achieved makes it a promising stimulus for cross-linking in tissue engineering applications.[273] Given their high modularity, CDs are excellent candidates for development of highly stimuli-responsive hydrogels for tissue engineering.

C.2.4 Hydrophobic Interactions

Hydrophobic interactions are one of the most important driving forces in the supramolecular assembly of tissue engineering complexes.[274] They can form physical cross-links between polymer chains, which are highly important in self-assembly of biological materials such as fibrillar proteins, or cause the association and subsequent self-assembly of supramolecular polymer fibers.[275] Hydrophobic interactions are driven by the entropic gain that follows from burying the hydrophobic faces of molecules away from the aqueous environment of the swollen hydrogel bulk and the subsequent release of surface-bound water, a large net entropic gain with a small enthalpy penalty.[276] This type of physical cross-linking can be combined with hydrogen bonding as in UPy and BTA where it acts as a protective pocket for the hydrogen bonds, as well as in host–guest interactions. It is often combined with chemical cross-linking to enhance the mechanical properties of the resulting gels, and unlike other supramolecular motifs, can be utilized to generate tough, self-healing hydrogels.[277,278]

C.2.4.1 Peptides and Peptide Amphiphiles

Due to their inherent bioactivity and biocompatibility, peptides are excellent choices for use in biodegradable supramolecular hydrogel building blocks.[192] Peptide amphiphiles (PA) with hydrophilic peptide segments covalently bonded to long hydrophobic polymer tails have been widely used to construct self-assembling, bioactive supramolecular materials.[279,280] PA, consisting of a peptide(s) covalently bonded to a carefully designed synthetic polymer, have been developed into self-assembling hydrogels.[281] Supramolecular fibers formed from self-assembly of PAs have been shown to allow bioactive cues such as the fibronectin-derived arginylglycylaspartic acid (RGD) peptide to freely move along the backbone of the fiber to attain optimal and dynamic RGD spacing, a benefit over covalent polymers, where the spacing and concentration of RGD must be strictly controlled.[282]

Due to the biodegradability and nontoxic nature of PA hydrogels, they have been extensively studied for 3D cell culture. For example, di-block co-polypeptide amphiphiles that self-assemble into rapidly self-healing, degradable, and functional hydrogels have been synthesized that have potential in biomedical applications.[283] Once injected, these supramolecular hydrogels aid in establishing a preferential environment for therapeutic cells, and can direct them toward the desired lineage. For example, the self-assembly of amyloid fibers was utilized to develop a tunable, self-healing, thermo-responsive hydrogel that promoted cell attachment, spreading, and differentiation toward a neuronal lineage.[284] This gel is nontoxic in various cell lines, an important step toward utilization in vivo. Additionally, both in vitro and in vivo differentiation of mesenchymal stem cells into chondrocytes without the use of exogenous growth factors was reported in hyaluronate and heparin mimicking PA hydrogels.[285]

Work has been done to improve the encapsulation of hydrophobic drugs in PA-based materials for drug delivery purposes. To this end, aliphatic chains have been added to peptide nanofibers to enhance the solubility of hydrophobic drugs in the aqueous environment, allowing their use as efficient drug delivery vehicles, however these self-assembling nanofibers were not able to form hydrogels.[286] Later work developed a smart peptide-based logic-gate hydrogel that can sense various biological disease markers and can be programmed for controlled drug release, answering both the need for hydrophobic drug delivery and stimuli-responsive injectable hydrogel scaffolds.[287] Although these works represent important steps toward clinical application of PA hydrogels, the many advances made with PA nanofibers have yet to be incorporated into hydrogels for tissue engineering.

The bioactive properties of self-healing peptide-based hydrogels have also been used to good effect in the regeneration of hard tissues including bone, cartilage, and dental tissue, which represents a deviation from traditional approaches to engineering of hard tissues.[288–290] Self-assembling PAs have been used for dual delivery of dental stem cells and growth factors to regenerate dentin.[281,290] Upon inclusion of a MMP-cleavable linker within the peptide sequence, enhanced viability, spreading, and migration of human mesenchymal stem cells was observed.[291] This material lacks the ability to completely self-heal, as the MMP-cleavable linkers are permanently cut during cell invasion, however, PAs with repeated self-healing abilities have also been explored for regeneration of nerves and angiogenesis.[290,292,293]

In addition to bone and dental engineering, recent advances have shown the potential for self-healing peptide-based supramolecular hydrogels to improve outcome in cardiovascular disease models by both improving angiogenesis and regenerating or attenuating damage to cardiac tissue following injury. These hydrogels represent a promising low-dose delivery system for growth factors given their many available binding sites and biocompatibility.[193] These materials have also been used for their advantageous mechanical properties and as delivery devices for cells to contribute to modest regeneration of functional cardiovascular tissue.[294,295] While they exhibit many advantageous properties, peptide-based systems also have drawbacks including their high costs, potential difficulty with scale-up, and less-controllable enzymatic degradation.[296]

C.2.4.2 Amphiphilic Block Copolymers

Although PAs are biocompatible and bioactive, due to the expense of large-scale peptide production, it became necessary to develop cost-effective, scalable systems. Amphiphilic block copolymers that self-assemble based on hydrophobic interactions have been utilized for drug delivery, cell-encapsulation, cartilage regeneration, and 3D bioprinting.[297–301] Recently, an injectable star PEG-b-poly (propylene sulfide) scaffold for wound repair was reported.[302] These hydrogel matrices self-assemble in aqueous media and effectively dissolve hydrophobic molecules, enabling local delivery of therapeutic doses of small molecules. Ultimately, these scaffolds improved cellular infiltration, reduced inflammation, and promoted wound closure in vivo, representing one of the few systems whose suitability for clinical translation has been tested.

C.2.5 Electrostatic (Ionic) Interactions

Ionically cross-linked hydrogels are biocompatible and self-healing based on the mild conditions and reversibility of their gelation, which is due to the electrostatic interaction between oppositely charged ions within the constituent materials.[303] Alginate, a naturally occurring, anionic, and hydrophilic polymer forms a cross-link in the presence of cations, most typically Ca^{2+}, and is the most well-studied ionically cross-linked polymer for tissue engineering.[304–306] Initial hurdles to its use, including control of gelation rate, and lack of uniform structure have been addressed.[303,307]

Various groups have introduced ionically cross-linked hydrogels with increased mechanical strength and toughness, addressing a known drawback of these types of hydrogels.[308,309] Recently, hyaluronate-based hydrogels have been explored as scaffolds for injectable cell delivery, an important area of development in tissue engineering.[310] Other materials such as PEG and clay have also been used to prepare ionically cross-linked hydrogels with unique properties and potential applications in tissue engineering, however, it should be noted that most ionically cross-linked hydrogels are not inherently self-healing and often require many modifications to achieve this property.[311,312]

C.2.6 Metal Coordination

Metal–ligand coordination plays a critical role in adhesion, self-assembly, and toughness in many biological materials.[313] Metal–ligand complexation has been widely utilized in the formation of supramolecular self-healing hydrogels owing to their high stability, rapid self-assembly, relatively high bonding energies, and the ease of incorporating biocompatible polymers.[314–316] A supramolecular metal–ligand complex is formed between a transition metal ion and the electron-donating organic ligand to enable a rapidly reversible and spontaneous linkage, the stability of which varies based on metal-ion concentration and pH.[314,317] With careful selection of the metal–ligand pair, supramolecular hydrogels with many advantageous near-covalent mechanical properties may be developed.[184]

Researchers have sought to mimic the viscoelasticity and the partial recovery of the Young's Modulus that leads to the acellular self-healing abilities displayed by mussel byssal threads.[315] The histidine-metal coordination acts as a sacrificial bond to dissipate energy and is reformed upon removal of the applied load. Apart from histidine, the pH-induced Fe^{3+}-catechol cross-linking pair has been used to generate self-healing supramolecular hydrogels that achieve near-covalent elastic moduli.[318] This work establishes a method for decoration of hydrophilic polymers with metal-coordinating ligands but does not offer insight into their suitability for biomedical applications. Subsequent work in the area resulted in histidine-based metal coordination hydrogels made with PEG which establishes a robust self-healing biomaterial with mechanical properties comparable to native soft tissues.[315] These monovalent systems were not designed for tissue engineering, and as such their biocompatibility has not been fully evaluated and their stability in vivo is likely low, making them less useful for longer-term applications.[319] Recently, an injectable hydrogel that uses reversible poly-histidine-Ni coordination bonds has been used to make a multivalent biomaterial stable enough for use in sustained drug delivery systems but it's in vivo suitability is yet to be proven.[320]

Other ligands for metal coordination hydrogels have been developed including terpyridine, a pyridine derivative commonly used to form directed and stable but reversible complexes with a variety of metal ions in biocompatible hydrogels, however, these remain largely unproven in tissue engineering systems.[321] Although not intended for tissue engineering, a conductive, self-healing hybrid hydrogel has been reported which has potential for prostheses given its conductivity, enhanced mechanical properties, and elasticity.[322] Metal–ligand coordination-based hydrogels offer unique materials with potential to achieve high elastic moduli while maintaining their self-healing properties and represent an interesting class of biomaterials for tissue engineering.

C.3 Conclusions and Outlook

Recent innovations in supramolecular chemistry and biology, including a more complete investigation of ECM properties on cell fate and function, scaffold effects, and growth factors, have been incorporated into supramolecular hydrogel design to develop novel biomaterials with self-healing capabilities that are very useful in tissue engineering. These materials have been explored for 3D culture of various cell types as well as regeneration of dental and bone tissue in addition to soft tissue engineering such as dental pulp, cartilage, and cardiovascular tissues.

Looking forward, major advances in self-healing supramolecular hydrogels will come from the continued incorporation of novel chemistries into biocompatible hydrogels that can advantageously recapitulate native tissue architecture and offer controlled delivery of cells and signaling cues. Specifically, supramolecular ‘monomer' units will continue to be developed that direct spatiotemporal control of drugs and biologics. Structural, mechanical, and dynamic behavior are a hallmark of native tissue, and some of the most difficult aspects to mimic given the large range of cell types and tissue systems. One could envision that future ‘smart' materials would be able to not only react to stimuli but respond and adapt to mechanical and biological changes in the scaffold, controlling release of drugs and biologics in advantageous spatiotemporal patterns over a controlled timeframe. In addition to materials chemistry, cell adhesion is critical to cell infiltration and therefore to tissue integration, a goal for many tissue engineering constructs.

The mechanical properties of these soft hydrogels may need to be improved for applications that require stiffer scaffolds, a slower rate of erosion and clearance, repeated self-healing, or a combination thereof. This may be achieved by the advent of biomaterials that repeatedly self-heal under physiological conditions, allowing sustained release of drugs and biologics as well as the retention of bulk properties.

Many currently available supramolecular hydrogels, although they have been extensively characterized, have yet to be tested in vivo, and in some cases, have not yet been evaluated in vitro, meaning their suitability for clinical application is to be determined. The development of future hydrogel biomaterials for tissue engineering purposes should include studies on biocompatibility and host integration, including potential immune response, to enable regeneration or complete replacement of lost or damaged tissues, eventually leading to improved patient outcomes and quality of life.

CCC | Marketplace™

This is a License Agreement between Laura Saunders ("User") and Copyright Clearance Center, Inc. ("CCC") on behalf of the Rightsholder identified in the order details below. The license consists of the order details, the CCC Terms and Conditions below, and any Rightsholder Terms and Conditions which are included below.

All payments must be made in full to CCC in accordance with the CCC Terms and Conditions below.

Order Date	27-Oct-2021	**Type of Use**	Republish in a thesis/dissertation
Order License ID	1157394-1	**Publisher**	WILEY
ISSN	1616-5195	**Portion**	Chapter/article

LICENSED CONTENT

Publication Title	Macromolecular bioscience	**Publication Type**	e-Journal
Article Title	Self-Healing Supramolecular Hydrogels for Tissue Engineering Applications.	**Start Page**	1800313
Date	01/01/2001	**Issue**	1
Language	English	**Volume**	19
Country	Germany	**URL**	http://www3.interscience.wiley.com/cgi-bi...
Rightsholder	John Wiley & Sons - Books		

REQUEST DETAILS

Portion Type	Chapter/article	**Rights Requested**	Main product
Page range(s)	1 - 11	**Distribution**	United States
Total number of pages	11	**Translation**	Original language of publication
Format (select all that apply)	Electronic	**Copies for the disabled?**	No
Who will republish the content?	Academic institution	**Minor editing privileges?**	Yes
Duration of Use	Life of current edition	**Incidental promotional use?**	No
Lifetime Unit Quantity	Up to 499	**Currency**	USD

Figure C- 6. Proof of permission for inclusion in this dissertation.

This work has been approved for inclusion in this dissertation with minor adjustments by the publishers, John Wiley & Sons (Figure 5-6).

Bibliography

1. Naldini, L. Gene therapy returns to centre stage. *Nature* **526**, 351–360 (2015).

2. Dunbar, C. E. *et al.* Gene therapy comes of age. *Science (80-.).* **359**, (2018).

3. Ma, C. C., Wang, Z. L., Xu, T., He, Z. Y. & Wei, Y. Q. The approved gene therapy drugs worldwide: from 1998 to 2019. *Biotechnol. Adv.* **40**, 107502 (2020).

4. Deverman, B. E., Ravina, B. M., Bankiewicz, K. S., Paul, S. M. & Sah, D. W. Y. Gene therapy for neurological disorders: Progress and prospects. *Nat. Rev. Drug Discov.* **17**, 641–659 (2018).

5. Ginn, S. L., Amaya, A. K., Alexander, I. E., Edelstein, M. & Abedi, M. R. Gene therapy clinical trials worldwide to 2017: An update. *J. Gene Med.* **20**, 1–16 (2018).

6. Keles, E., Song, Y., Du, D., Dong, W. J. & Lin, Y. Recent progress in nanomaterials for gene delivery applications. *Biomater. Sci.* **4**, 1291–1309 (2016).

7. Alhakamy, N. A., Curiel, D. T. & Berkland, C. J. The era of gene therapy: From preclinical development to clinical application. *Drug Discov. Today* **26**, 1602–1619 (2021).

8. Yin, H., Kauffman, K. J. & Anderson, D. G. Delivery technologies for genome editing. *Nat. Publ. Gr.* **16**, 387–399 (2017).

9. Mellott, A. J., Forrest, M. L. & Detamore, M. S. Physical non-viral gene delivery methods for tissue engineering. *Ann. Biomed. Eng.* **41**, 446–468 (2013).

10. Young, J. L. & Dean, D. A. *Electroporation-Mediated Gene Delivery*. *Advances in Genetics* **89**, (Elsevier Ltd, 2015).

11. Yin, H. *et al.* Non-viral vectors for gene-based therapy. *Nat. Publ. Gr.* **15**, 541–555 (2014).

12. Nayerossadat, N., Ali, P. & Maedeh, T. Viral and nonviral delivery systems for gene delivery. *Adv. Biomed. Res.* **1**, 27 (2012).

13. Yin, H. *et al.* Non-viral vectors for gene-based therapy. *Nat. Rev. Genet.* **15**, 541–555 (2014).

14. Dahlman, J. E. *et al.* NIH Public Access. **9**, 648–655 (2015).

15. Kauffman, K. J., Webber, M. J. & Anderson, D. G. Materials for non-viral intracellular delivery of messenger RNA therapeutics. *J. Control. Release* **240**, 227–234 (2016).

16. Shirley, J. L., de Jong, Y. P., Terhorst, C. & Herzog, R. W. Immune Responses to Viral Gene Therapy Vectors. *Mol. Ther.* **28**, 709–722 (2020).

17. Li, C. & Samulski, R. J. Engineering adeno-associated virus vectors for gene therapy. *Nat. Rev. Genet.* **21**, 255–272 (2020).

18. Nidetz, N. F. *et al.* Adeno-associated viral vector-mediated immune responses: Understanding barriers to gene delivery. *Pharmacol. Ther.* **207**, 107453 (2020).

19. Merten, O.-W. AAV vector production: state of the art developments and remaining challenges. *Cell Gene Ther. Insights* **2**, 521–551 (2016).

20. Wilson, J. M. Lessons learned from the gene therapy trial for ornithine transcarbamylase deficiency. *Mol. Genet. Metab.* **96**, 151–157 (2009).

21. Pack, D. W., Hoffman, A. S., Pun, S. & Stayton, P. S. Design and development of polymers for gene delivery. *Nature Reviews Drug Discovery* **4**, 581–593 (2005).

22. Mintzer, M. A. & Simanek, E. E. Nonviral vectors for gene delivery. *Chem. Rev.* **109**, 259–302 (2009).

23. Lin, G. *et al.* Non-viral gene therapy using multifunctional nanoparticles: Status, challenges, and opportunities. *Coord. Chem. Rev.* **374**, 133–152 (2018).

24. Monopoli, M. P., Åberg, C., Salvati, A. & Dawson, K. A. Biomolecular coronas provide the biological identity of nanosized materials. *Nat. Nanotechnol.* **7**, 779–786 (2012).

25. Hardee, C. L., Arevalo-Soliz, L. M., Hornstein, B. D. . & Zechiedrich, L. Advances in Non-Viral DNA Vectors for Gene Therapy. *Genes (Basel).* **8**, 1–22 (2017).

26. Quevedo, D. F. *et al.* Multifunctional Synthetic Protein Nanoparticles via Reactive Electrojetting. *Macromol. Rapid Commun.* **41**, (2020).

27. Buck, J., Grossen, P., Cullis, P. R., Huwyler, J. & Witzigmann, D. Lipid-based DNA therapeutics: Hallmarks of non-viral gene delivery. *ACS Nano* **13**, 3754–3782 (2019).

28. Lai, W. F. & Wong, W. T. Design of Polymeric Gene Carriers for Effective Intracellular Delivery. *Trends Biotechnol.* **36**, 713–728 (2018).

29. Loh, X. J., Lee, T. C., Dou, Q. & Deen, G. R. Utilising inorganic nanocarriers for gene delivery. *Biomater. Sci.* **4**, 70–86 (2016).

30. Rahmani, S. *et al.* Engineering of nanoparticle size via electrohydrodynamic jetting. *Bioeng. Transl. Med.* **1**, 82–93 (2016).

31. Rahmani, S. *et al.* Long-circulating Janus nanoparticles made by electrohydrodynamic co-jetting for systemic drug delivery applications Long-circulating Janus nanoparticles made by electrohydrodynamic co-jetting for systemic drug delivery applications. **2330**, (2015).

32. Gregory, J. V. *et al.* Systemic brain tumor delivery of synthetic protein nanoparticles for glioblastoma therapy. *Nat. Commun.* **11**, 1–15 (2020).

33. Kadiyala, P., Gregory, J. V., Lowenstein, P. R., Lahann, J. & Castro, M. G. Targeting gliomas with STAT3-silencing nanoparticles. *Molecular and Cellular Oncology* **8**, (2021).

34. Habibi, N. *et al.* Engineered Ovalbumin Nanoparticles for Cancer Immunotherapy. *Adv. Ther.* **3**, 1–11 (2020).

35. Misra, A. C., Bhaskar, S., Clay, N. & Lahann, J. Multicompartmental Particles for Combined Imaging and siRNA Delivery. 3850–3856 (2012). doi:10.1002/adma.201200372

36. Fanali, G. *et al.* Human serum albumin: From bench to bedside. *Mol. Aspects Med.* **33**, 209–290 (2012).

37. Kouchakzadeh, H., Safavi, M. S. & Shojaosadati, S. A. *Efficient Delivery of Therapeutic Agents by Using Targeted Albumin Nanoparticles*. *Advances in Protein Chemistry and Structural Biology* **98**, (Elsevier Inc., 2015).

38. Kumari, M., Liu, C. H. & Wu, W. C. Efficient gene delivery by oligochitosan conjugated serum albumin: Facile synthesis, polyplex stability, and transfection. *Carbohydr. Polym.* **183**, 37–49 (2018).

39. Nicolì, E., Syga, M. I., Bosetti, M. & Shastri, V. P. Enhanced gene silencing through human serum albumin-mediated delivery of polyethylenimine-siRNA polyplexes. *PLoS One* **10**, 1–16 (2015).

40. Du, J., Li, B., Zhang, P. & Wang, Y. Colloids and Surfaces B : Biointerfaces Cationized bovine serum albumin as gene carrier : Influence of specific secondary structure on DNA complexibility and gene transfection. *Colloids Surfaces B Biointerfaces* **143**, 37–46 (2016).

41. Nel, A. E. *et al.* Understanding biophysicochemical interactions at the nano-bio

interface. *Nat. Mater.* **8**, 543–557 (2009).

42. Champion, J. A. & Mitragotri, S. Shape induced inhibition of phagocytosis of polymer particles. *Pharm. Res.* **26**, 244–249 (2009).

43. Pezzoli, D., Giupponi, E., Mantovani, D. & Candiani, G. Size matters for in vitro gene delivery : investigating the relationships among complexation protocol , transfection medium , size and sedimentation. *Nat. Publ. Gr.* 1–11 (2017). doi:10.1038/srep44134

44. Behzadi, S. *et al.* Cellular uptake of nanoparticles: journey inside the cell. *Chem. Soc. Rev.* **46**, 4218–4244 (2017).

45. Park, J. *et al.* A review of RGD-functionalized nonviral gene delivery vectors for cancer therapy. *Cancer Gene Ther.* **19**, 741–748 (2012).

46. Fernández, M., Javaid, F. & Chudasama, V. Advances in targeting the folate receptor in the treatment/imaging of cancers. *Chem. Sci.* **9**, 790–810 (2018).

47. Springer, A. D. & Dowdy, S. F. GalNAc-siRNA Conjugates: Leading the Way for Delivery of RNAi Therapeutics. *Nucleic Acid Therapeutics* **28**, 109–118 (2018).

48. Hillaireau, H. & Couvreur, P. Nanocarriers' entry into the cell: Relevance to drug delivery. *Cell. Mol. Life Sci.* **66**, 2873–2896 (2009).

49. Sahay, G., Alakhova, D. Y. & Kabanov, A. V. Endocytosis of nanomedicines. *J. Control. Release* **145**, 182–195 (2010).

50. Harush-Frenkel, O., Debotton, N., Benita, S. & Altschuler, Y. Targeting of nanoparticles to the clathrin-mediated endocytic pathway. *Biochem. Biophys. Res. Commun.* **353**, 26–32 (2007).

51. He, C., Hu, Y., Yin, L., Tang, C. & Yin, C. Effects of particle size and surface charge on cellular uptake and biodistribution of polymeric nanoparticles. *Biomaterials* **31**, 3657–3666 (2010).

52. Chatterjee, M. *et al.* Caveolae-mediated endocytosis is critical for albumin cellular uptake and response to albumin-bound chemotherapy. *Cancer Res.* **77**, 5925–5937 (2017).

53. Doherty, G. J. & McMahon, H. T. Mechanisms of endocytosis. *Annu. Rev. Biochem.* **78**, 857–902 (2009).

54. Hoekstra, D., Rejman, J., Wasungu, L., Shi, F. & Zuhorn, I. Gene delivery by cationic lipids: In and out of an endosome. *Biochem. Soc. Trans.* **35**, 68–71 (2007).

55. Karimi, M. *et al. Smart micro/nanoparticles in stimulus-responsive drug/gene delivery systems*. *Chemical Society Reviews* **45**, (Royal Society of Chemistry, 2016).

56. Sahay, G., Kim, J. O., Kabanov, A. V. & Bronich, T. K. The exploitation of differential endocytic pathways in normal and tumor cells in the selective targeting of nanoparticulate chemotherapeutic agents. *Biomaterials* **31**, 923–933 (2010).

57. Akinc, A., Thomas, M., Klibanov, A. M. & Langer, R. Exploring polyethylenimine-mediated DNA transfection and the proton sponge hypothesis. *J. Gene Med.* **7**, 657–663 (2005).

58. Behr, J. The proton sponge: a trick to enter cells the viruses did not exploit. *Int. J. Chem.* **2**, 34–36 (1997).

59. Ryu, N. *et al.* Effective PEI-mediated delivery of CRISPR-Cas9 complex for targeted gene therapy. *Nanomedicine Nanotechnology, Biol. Med.* **14**, 2095–2102 (2018).

60. Varkouhi, A. K., Scholte, M., Storm, G. & Haisma, H. J. Endosomal escape pathways for delivery of biologicals. *J. Control. Release* **151**, 220–228 (2011).

61. Vermeulen, L. M. P. *et al.* Endosomal Size and Membrane Leakiness Influence Proton Sponge-Based Rupture of Endosomal Vesicles. *ACS Nano* **12**, 2332–2345 (2018).

62. Akinc, A., Thomas, M., Klibanov, A. M. & Langer, R. Exploring polyethylenimine-mediated DNA transfection and the proton sponge hypothesis. *J. Gene Med.* **7**, 657–663 (2005).

63. Ahmad, A., Khan, J. M. & Haque, S. Strategies in the design of endosomolytic agents for facilitating endosomal escape in nanoparticles. *Biochimie* **160**, 61–75 (2019).

64. Bai, H., Lester, G. M. S., Petishnok, L. C. & Dean, D. A. Cytoplasmic transport and nuclear import of plasmid. *Biosci. Rep.* **0**, 1–17 (2017).

65. Brandén, L. J., Mohamed, A. J. & Smith, C. I. E. A peptide nucleic acid-nuclear localization signal fusion that mediates nuclear transport of DNA. *Nat. Biotechnol.* **17**, 784–787 (1999).

66. Dean, D. A. Import of Plasmid DNA into the Nucleus Is Sequence Specific. *Exp. Cell Res.* **230**, 293–302 (1997).

67. Xu, Y. *et al.* Incorporation of a Nuclear Localization Signal in pH Responsive LAH4-L1 Peptide Enhances Transfection and Nuclear Uptake of Plasmid DNA. (2016).

doi:10.1021/acs.molpharmaceut.6b00338

68. Zanta, M. A., Belguise-Valladier, P. & Behr, J. P. Gene delivery: A single nuclear localization signal peptide is sufficient to carry DNA to the cell nucleus. *Proc. Natl. Acad. Sci. U. S. A.* **96**, 91–96 (1999).

69. Chen, K. *et al.* A gene delivery system containing nuclear localization signal: Increased nucleus import and transfection efficiency with the assistance of RanGAP1. *Acta Biomater.* **48**, 215–226 (2017).

70. Utvik, J. K., Njå, A. & Gundersen, K. DNA injection into single cells of intact mice. *Hum. Gene Ther.* **10**, 291–300 (1999).

71. Zou, S., Scarfo, K., Nantz, M. H. & Hecker, J. G. Lipid-mediated delivery of RNA is more efficient than delivery of DNA in non-dividing cells. *Int. J. Pharm.* **389**, 232–243 (2010).

72. Adijanto, J. & Naash, M. I. Nanoparticle-based technologies for retinal gene therapy. *Eur. J. Pharm. Biopharm.* **95**, 353–367 (2015).

73. Garrett, Reginald H; Grisham, Charles M.; Andreopoulos, Stavroula; Willmore, William G.; Gallouzi, I. E. *Biochemistry (1st Candadian Edition)*. **1**, (Nelson Education, 2013).

74. Invitrogen. Lipofectamine 2000 Reagent Protocol. *Protocol Pub. No. MAN0007824 Rev.1.0 Lipofectamine®* (2013).

75. Amreddy, N., Babu, A., Muralidharan, R., Munshi, A. & Ramesh, R. *Polymeric Nanoparticle-Mediated Gene Delivery for Lung Cancer Treatment. In: Cheng Y. (eds) Polymeric Gene Delivery Systems. Topics in Current Chemistry Collections*. *Topics in Current Chemistry* **375**, (Springer, Cham, 2017).

76. Holbein, M. E. B. Understanding FDA Regulatory Requirements for Investigational New Drug Applications for Sponsor-Investigators. *J. Investig. Med.* **57**, 688–694 (2009).

77. Jain, A. K. *et al.* Development of a method to quantify the DNA content in cationic peptide-DNA nanoparticles. *J. Pharm. Biomed. Anal.* **100**, 236–242 (2014).

78. Carrillo, C. *et al.* Chitosan nanoparticles as non-viral gene delivery systems: Determination of loading efficiency. *Biomedicine and Pharmacotherapy* **68**, 775–783 (2014).

79. Liu, Y. & Deng, X. Influences of preparation conditions on particle size and DNA-loading efficiency for poly(dl-lactic acid–polyethylene glycol) microspheres entrapping free DNA. *J. Control. Release* **83**, 147–155 (2002).

80. Balbino, T. A. *et al.* Microfluidic Assembly of pDNA/Cationic Liposome Lipoplexes with High pDNA Loading for Gene Delivery. *Langmuir* **32**, 1799–1807 (2016).

81. Tang, J. *et al.* Calcium phosphate embedded PLGA nanoparticles : A promising gene delivery vector with high gene loading and transfection efficiency. *Int. J. Pharm.* **431**, 210–221 (2012).

82. Yin, H., Kauffman, K. J. & Anderson, D. G. Delivery technologies for genome editing. *Nat. Publ. Gr.* **16**, 387–399 (2017).

83. Deweerdt, S. RNA Therapies Explained. *Nature* **574**, 7–8 (2019).

84. Ginn, S. L., Amaya, A. K., Abedi, M. R., Alexander, I. E. & Edelstein, M. Gene therapy clinical trials worldwide to 2017 : An update. 1–16 (2018). doi:10.1002/jgm.3015

85. Damase, T. R. *et al.* The Limitless Future of RNA Therapeutics. *Front. Bioeng. Biotechnol.* **9**, 1–24 (2021).

86. Dagan, N. *et al.* BNT162b2 mRNA Covid-19 Vaccine in a Nationwide Mass Vaccination Setting. *N. Engl. J. Med.* **384**, 1412–1423 (2021).

87. Polack, F. P. *et al.* Safety and Efficacy of the BNT162b2 mRNA Covid-19 Vaccine. *N. Engl. J. Med.* **383**, 2603–2615 (2020).

88. Golob, J. L., Lugogo, N., Lauring, A. S. & Lok, A. S. SARS-CoV-2 vaccines: A triumph of science and collaboration. *JCI Insight* **6**, (2021).

89. Patil, S., Gao, Y., Lin, X., Li, Y. & Dang, K. The Development of Functional Non-Viral Vectors for Gene Delivery. *Int. J. Mol. Sci.* **20**, 1–23 (2019).

90. Banjar, Z. M. & Amiji, M. M. Optimization of the Conditions for Plasmid DNA Delivery and Transfection with Self-Assembled Hyaluronic Acid-Based Nanoparticles. *Mol. Pharm.* **16**, 128–140 (2019).

91. Comisel, R. M., Kara, B., Fiesser, F. H. & Farid, S. S. Lentiviral vector bioprocess economics for cell and gene therapy commercialization. *Biochem. Eng. J.* **167**, 107868 (2021).

92. Liu, C., Zhang, L., Liu, H. & Cheng, K. Delivery strategies of the CRISPR-Cas9 gene-editing system for therapeutic applications. *J. Control. Release* **266**, 17–26 (2017).

93. Xue, W. *et al.* CRISPR-mediated direct mutation of cancer genes in the mouse liver. *Nature* (2014). doi:10.1038/nature13589

94. Wahane, A. *et al.* Role of Lipid-Based and Polymer-Based Non-Viral Vectors in Nucleic Acid Delivery for Next-Generation Gene Therapy. *Molecules* **25**, (2020).

95. Xiong, L. & Qiao, S. Z. A mesoporous organosilica nano-bowl with high DNA loading capacity-a potential gene delivery carrier. *Nanoscale* **8**, 17446–17450 (2016).

96. Kim, M. H. *et al.* Facile synthesis of monodispersed mesoporous silica nanoparticles with ultralarge pores and their application in gene delivery. *ACS Nano* **5**, 3568–3576 (2011).

97. Hurst, S. J., Lytton-jean, A. K. R. & Mirkin, C. A. Maximizing DNA Loading on a Range of Gold Nanoparticle Sizes. *Anal. Chem.* **78**, 8313–8318 (2006).

98. Blum, J. S. & Saltzman, W. M. High loading efficiency and tunable release of plasmid DNA encapsulated in submicron particles fabricated from PLGA conjugated with poly-L-lysine. *J. Control. Release* **129**, 66–72 (2008).

99. Schmid, F. & Beer, L. Biological Macromolecules : Spectrophotometry Concentrations. *Methods* 1–4 (2001).

100. Nakayama, Y., Yamaguchi, H., Einaga, N. & Esumi, M. Pitfalls of DNA quantification using dnabinding fluorescent dyes and suggested solutions. *PLoS One* **11**, 1–12 (2016).

101. de Boer, E. N., van der Wouden, P. E., Johansson, L. F., van Diemen, C. C. & Haisma, H. J. A next-generation sequencing method for gene doping detection that distinguishes low levels of plasmid DNA against a background of genomic DNA. *Gene Ther.* **26**, 338–346 (2019).

102. Chapuis, A. G. *et al.* T cell receptor gene therapy targeting WT1 prevents acute myeloid leukemia relapse post-transplant. *Nat. Med.* **25**, 1064–1072 (2019).

103. Lungwitz, U., Breunig, M., Blunk, T. & Göpferich, A. Polyethylenimine-based non-viral gene delivery systems. *Eur. J. Pharm. Biopharm.* **60**, 247–266 (2005).

104. Giles, K. W. . & Myers, A. An Improved Diphenylamine Method for the Estimation of Deoxyribonucleic Acid. *Nature* **451**, 93–94 (1965).

105. Richards, G. M. Modifications of the diphenylamine reaction giving increased sensitivity and simplicity in the estimation of DNA. *Anal. Biochem.* **57**, 369–376 (1974).

106. Soto, E. R. & Ostroff, G. R. Characterization of Multilayered Nanoparticles Encapsulated in Yeast Cell Wall Particles for DNA Delivery. *Bioconjug. Chem.* **19**, 840–848 (2008).

107. Thomsen, T., Ayoub, A. B., Psaltis, D. & Klok, H. A. Fluorescence-Based and Fluorescent Label-Free Characterization of Polymer Nanoparticle Decorated T Cells. *Biomacromolecules* **22**, 190–200 (2021).

108. McErlean, E. M. *et al.* Rational design and characterisation of a linear cell penetrating peptide for non-viral gene delivery. *J. Control. Release* **330**, 1288–1299 (2021).

109. Danaei, M. *et al.* Impact of Particle Size and Polydispersity Index onthe Clinical Applications of Lipidic Nanocarrier Systems. *Pharmaceutics* **388**, (2018).

110. FISCHER, H., POLIKARPOV, I. & Craievich, A. F. Average protein density is a molecular-weight-dependent function _ Enhanced Reader.pdf. *Protein Sci.* **13**, 2825–2828 (2004).

111. Myerson, J. W. *et al.* Supramolecular Organization Predicts Protein Nanoparticle Delivery to Neutrophils for Acute Lung Inflammation Diagnosis and Treatment. *bioRxiv* 1–44 (2020).

112. von Roemeling, C., Jiang, W., Chan, C. K., Weissman, I. L. & Kim, B. Y. S. Breaking Down the Barriers to Precision Cancer Nanomedicine. *Trends Biotechnol.* **35**, 159–171 (2017).

113. Xiang, S. *et al.* Uptake mechanisms of non-viral gene delivery. *J. Control. Release* **158**, 371–378 (2012).

114. Chen, K. *et al.* A gene delivery system containing nuclear localization signal: Increased nucleus import and transfection efficiency with the assistance of RanGAP1. *Acta Biomater.* **48**, 215–226 (2017).

115. Lokugamage, M. P. *et al.* Optimization of lipid nanoparticles for the delivery of nebulized therapeutic mRNA to the lungs. *Nat. Biomed. Eng.* **5**, (2021).

116. Li, X. *et al.* A mesoporous silica nanoparticle - PEI - Fusogenic peptide system for siRNA delivery in cancer therapy. *Biomaterials* **34**, 1391–1401 (2013).

117. Argyo, C., Weiss, V., Bra, C. & Bein, T. Multifunctional Mesoporous Silica Nanoparticles as a Universal Platform for Drug Delivery. (2013). doi:10.1021/cm402592t

118. Niu, J. *et al.* Transdermal Gene Delivery by Functional Peptide-Conjugated Cationic Gold Nanoparticle Reverses the Progression and Metastasis of Cutaneous Melanoma. *ACS Appl. Mater. Interfaces* **9**, 9388–9401 (2017).

119. Sandhu, K. K., Mcintosh, C. M., Simard, J. M., Smith, S. W. & Rotello, V. M. Gold Nanoparticle-Mediated Transfection of Mammalian Cells. *Bioconjug. Chem.* **13**, 3–

6 (2002).

120. Kumar, R. *et al.* Efficient Polymer-Mediated Delivery of Gene- Editing Ribonucleoprotein Payloads through Combinatorial Design, Parallelized Experimentation, and Machine Learning. *ACS Nano* **14**, 17626–17639 (2020).

121. Habibi, N., Quevedo, D. F., Gregory, J. V. & Lahann, J. Emerging methods in therapeutics using multifunctional nanoparticles. *Wiley Interdiscip. Rev. Nanomedicine Nanobiotechnology* **12**, (2020).

122. Rahmani, S., Park, T., Frances, A. & Lahann, J. Multimodal delivery of irinotecan from microparticles with two distinct compartments. *J. Control. Release* **172**, 239–245 (2013).

123. Rahmani, S. *et al.* Long-circulating Janus nanoparticles made by electrohydrodynamic co-jetting for systemic drug delivery applications Long-circulating Janus nanoparticles made by electrohydrodynamic co-jetting for systemic drug delivery applications. **2330**, (2015).

124. Brown, T. D., Habibi, N., Wu, D., Lahann, J. & Mitragotri, S. Effect of Nanoparticle Composition, Size, Shape, and Sti ff ness on Penetration Across the Blood − Brain Barrier. *ACS Biomater. Sci. Eng.* **6**, 4916–4928 (2020).

125. Elzoghby, A. O., Samy, W. M. & Elgindy, N. A. Albumin-based nanoparticles as potential controlled release drug delivery systems. *J. Control. Release* **157**, 168–182 (2012).

126. Zhang, T., Song, X., Kang, D., Zhang, L. & Zhang, C. Modified bovine serum albumin as an effective charge-reversal platform for simultaneously improving the transfection efficiency and biocompatibility. 4698–4706 (2015). doi:10.1039/c5tb00548e

127. Rhaese, S., Briesen, H. Von, Rubsamen-waigmann, H. & Langer, K. Human serum albumin – polyethylenimine nanoparticles for gene delivery. **92**, 199–208 (2003).

128. Godbey, W. T., Wu, K. K. & Mikos, A. G. Poly(ethylenimine) and its role in gene delivery. *Journal of Controlled Release* **60**, 149–160 (1999).

129. Mady, M. M., Mohammed, W. A., El-guendy, N. M. & Elsayed, A. A. EFFECT OF POLYMER MOLECULAR WEIGHT ON THE DNA / PEI POLYPLEXES PROPERTIES. **21**, 151–165

130. Tanimoto, M., Kamiya, H., Minakawa, N., Matsuda, A. & Harashima, H. No Enhancement of Nuclear Entry by Direct Conjugation of a Nuclear Localization Signal Peptide to Linearized DNA. *Bioconjug. Chem.* **14**, 1197–1202 (2003).

131. Von Schwedler, U., Kornbluth, R. S. & Trono, D. The nuclear localization signal of

the matrix protein of human immunodeficiency virus type 1 allows the establishment of infection in macrophages and quiescent T lymphocytes. *Proc. Natl. Acad. Sci. U. S. A.* **91**, 6992–6996 (1994).

132. Bogacheva, M. *et al.* Arginine-rich cross-linking peptides with different SV40 nuclear localization signal content as vectors for intranuclear DNA delivery. *Bioorganic Med. Chem. Lett.* **27**, 4781–4785 (2017).

133. Jones, B., Nachtsheim, C. J. & Jones, B. A Class of Three-Level Designs for Definitive Screening in the Presence of Second-Order Effects A Class of Three-Level Designs for Definitive Screening in the Presence of Second-Order Effects. *J. Qual. Technol.* **43**, (2017).

134. Kau, K. J. *et al.* Optimization of Lipid Nanoparticle Formulations for mRNA Delivery in Vivo with Fractional Factorial and Defi nitive Screening Designs. *Nano Lett.* **15**, 7300–7306 (2015).

135. Khan, O. F. *et al.* Endothelial siRNA delivery in nonhuman primates using ionizable low – molecular weight polymeric nanoparticles. *Sci. Adv.* **4**, 1–11 (2018).

136. Saunders, L. & Ma, P. X. Self-Healing Supramolecular Hydrogels for Tissue Engineering Applications. *Macromol. Biosci.* **19**, (2019).

137. Dang, M., Saunders, L., Niu, X., Fan, Y. & Ma, P. X. Biomimetic delivery of signals for bone tissue engineering. *Bone Res.* **6**, (2018).

138. Liu, Z. *et al.* Nanofibrous Spongy Microspheres to Distinctly Release miRNA and Growth Factors to Enrich Regulatory T Cells and Rescue Periodontal Bone Loss. *ACS Nano* **12**, (2018).

139. Stathopulos, P. B. *et al.* Sonication of proteins causes formation of aggregates that resemble amyloid. *Protein Science* **13**, 3017–3027 (2008).

140. Wei, T. *et al.* Delivery of Tissue-Targeted Scalpels: Opportunities and Challenges for in Vivo CRISPR/Cas-Based Genome Editing. *ACS Nano* **14**, 9243–9262 (2020).
141. Zhang, Y., Satterlee, A. & Huang, L. In vivo gene delivery by nonviral vectors: Overcoming hurdles. *Mol. Ther.* **20**, 1298–1304 (2012).

142. Mout, R., Ray, M., Lee, Y. W., Scaletti, F. & Rotello, V. M. In Vivo Delivery of CRISPR/Cas9 for Therapeutic Gene Editing: Progress and Challenges. *Bioconjug. Chem.* **28**, 880–884 (2017).

143. Rahmani, S. *et al.* Dual Release Carriers for Cochlear Delivery. 94–100 (2016). doi:10.1002/adhm.201500141

144. Wei, Y., Quan, L., Zhou, C. & Zhan, Q. Factors relating to the biodistribution &

clearance of nanoparticles & their effects on in vivo application. *Nanomedicine* **13**, 1495–1512 (2018).

145. Haubner, R. *et al.* Glycosylated RGD-Containing Peptides : Tracer for Tumor Targeting and Angiogenesis Imaging with Improved Biokinetics. *J. Nucl. Med.* **42**, 326–336 (2001).

146. Wilson, R. C. & Gilbert, L. A. The Promise and Challenge of in Vivo Delivery for Genome Therapeutics. *ACS Chemical Biology* **13**, 376–382 (2018).

147. Kattenhorn, L. M. *et al.* Adeno-Associated Virus Gene Therapy for Liver Disease. *Hum. Gene Ther.* **27**, 947–961 (2016).

148. Myerson, J. W. *et al.* Supramolecular arrangement of protein in nanoparticle structures predicts nanoparticle tropism for neutrophils in acute lung inflammation. *Nat. Nanotechnol.* (2021). doi:10.1038/s41565-021-00997-y

149. Pearce, A. K. & O'Reilly, R. K. Insights into Active Targeting of Nanoparticles in Drug Delivery: Advances in Clinical Studies and Design Considerations for Cancer Nanomedicine. *Bioconjug. Chem.* **30**, 2300–2311 (2019).

150. Zimmermann, T. S. *et al.* Clinical Proof of Concept for a Novel Hepatocyte-Targeting GalNAc-siRNA Conjugate. *Molecular Therapy* **25**, 71–78 (2017).

151. Marcos-Contreras, O. A. *et al.* Combining vascular targeting and the local first pass provides 100-fold higher uptake of ICAM-1-targeted vs untargeted nanocarriers in the inflamed brain. *J. Control. Release* **301**, 54–61 (2019).

152. Brenner, J. S. *et al.* Red blood cell-hitchhiking boosts delivery of nanocarriers to chosen organs by orders of magnitude. *Nature Communications* **9**, (2018).

153. Sanders, J. W. & Ponzio, T. A. Vectored immunoprophylaxis: An emerging adjunct to traditional vaccination. *Trop. Dis. Travel Med. Vaccines* **3**, 4–9 (2017).

154. Balazs, A. B. *et al.* Antibody-based protection against HIV infection by vectored immunoprophylaxis. *Nature* **481**, 81–86 (2012).

155. Goldenthal, K. L., Midthun, K. & Zoon, K. C. Control of Viral Infections and Diseases. *Med. Microbiol.* 1–8 (1996).

156. Ljungman, P. Vaccination of immunocompromised patients. *Clin. Microbiol. Infect.* **18**, 93–99 (2012).

157. Priddy, F. H. *et al.* Adeno-associated virus vectored immunoprophylaxis to prevent HIV in healthy adults: a phase 1 randomised controlled trial. *Lancet HIV* **6**, e230–e239 (2019).

158. Deal, C. E. & Balazs, A. B. Engineering humoral immunity as prophylaxis or therapy. *Current Opinion in Immunology* **35**, 113–122 (2015).

159. Lara, A. R. & Ramirez, O. T. Plasmid DNA Production for Therapeutic Applications. in *Methods of Molecular Biology* 271–303 (Springer, 2012). doi:10.1007/978-1-61779-433-9_14

160. McCarty, D. M. Self-complementary AAV vectors; advances and applications. *Mol. Ther.* **16**, 1648–1656 (2008).

161. Tetteh, R. A. *et al.* Pre-Exposure Prophylaxis for HIV Prevention: Safety Concerns. *Drug Saf.* **40**, 273–283 (2017).

162. Long, C. *et al.* Postnatal genome editing partially restores dystrophin expression in a mouse model of muscular dystrophy. *Science* **351**, 400–403 (2016).

163. Huggett, B. Innovative Academic Startups 2016. *Nat. Biotechnol.* **35**, 16–17 (2017).
164. Givens, B. E., Naguib, Y. W., Geary, S. M., Devor, E. J. & Salem, A. K. Nanoparticle-Based Delivery of CRISPR/Cas9 Genome-Editing Therapeutics. *AAPS J.* **20**, (2018).

165. Vacan, J. P. & Langer, R. Tissue engineering : the design and fabrication of living replacement devices for surgical reconstruction and transplantation. 1–3 (1999).

166. Peppas, N. A., Hilt, J. Z., Khademhosseini, A. & Langer, R. Hydrogels in biology and medicine: From molecular principles to bionanotechnology. *Adv. Mater.* **18**, 1345–1360 (2006).

167. Caló, E. & Khutoryanskiy, V. V. Biomedical applications of hydrogels: A review of patents and commercial products. *Eur. Polym. J.* **65**, 252–267 (2015).

168. Wichterle, O. & Lím, D. Hydrophilic Gels for Biological Use. *Nature* **185**, 117–118 (1960).

169. Lee, K. Y. & Mooney, D. J. Hydrogels for Tissue Engineering. **101**, (2001).

170. Telemeco, T. A. *et al.* Regulation of cellular infiltration into tissue engineering scaffolds composed of submicron diameter fibrils produced by electrospinning. *Acta Biomater.* **1**, 377–385 (2005).

171. Wojtecki, R. J., Meador, M. A. & Rowan, S. J. Using the dynamic bond to access macroscopically responsive structurally dynamic polymers. *Nat. Mater.* **10**, 14–27 (2011).

172. Wang, H. & Heilshorn, S. C. Adaptable Hydrogel Networks with Reversible Linkages for Tissue Engineering. *Adv. Mater.* **27**, 3717–3736 (2015).

173. Rosales, A. M. & Anseth, K. S. The design of reversible hydrogels to capture extracellular matrix dynamics. *Nat. Rev. Mater.* **1**, 1–15 (2016).

174. Adzima, B. J., Kloxin, C. J. & Bowman, C. N. Externally triggered healing of a thermoreversible covalent network via self-limited hysteresis heating. *Adv. Mater.* **22**, 2784–2787 (2010).

175. Chen, X. A Thermally Re-mendable Cross-Linked Polymeric Material. *Science (80-.).* **295**, 1698–1702 (2002).

176. Wu, J., Su, Z. G. & Ma, G. H. A thermo- and pH-sensitive hydrogel composed of quaternized chitosan/glycerophosphate. *Int. J. Pharm.* **315**, 1–11 (2006).

177. Zhang, R., Tang, M., Bowyer, A., Eisenthal, R. & Hubble, J. A novel pH- and ionic-strength-sensitive carboxy methyl dextran hydrogel. *Biomaterials* **26**, 4677–4683 (2005).

178. Kloxin, A. M., Tibbitt, M. W. & Anseth, K. S. Synthesis of photodegradable hydrogels as dynamically tunable cell culture platforms. *Nat. Protoc.* **5**, 1867–1887 (2010).

179. Fairbanks, B. D., Singh, S. P., Bowman, C. N. & Anseth, K. S. Photodegradable, photoadaptable hydrogels via radical-mediated disulfide fragmentation reaction. *Macromolecules* **44**, 2444–2450 (2011).

180. Angeles, L. & Boulder, C. Photodegradable Hydrogels for Dynamic Tuning of Physical and Chemical Properties. **324**, 59–64 (2009).

181. Scott, T. F., Schneider, A. D., Cook, W. D. & Bowman, C. N. Chemistry: Photoinduced plasticity in cross-linked polymers. *Science (80-.).* **308**, 1615–1617 (2005).

182. Rowan, S. J., Cantrill, S. J., Cousins, G. R. L., Sanders, J. K. M. & Stoddart, J. F. Dynamic Covalent Chemistry. *Angew. Chem. Int. Ed.* **41**, 898–952 (2002).

183. Qu, J., Zhao, X., Ma, P. X. & Guo, B. pH-responsive self-healing injectable hydrogel based on N-carboxyethyl chitosan for hepatocellular carcinoma therapy. *Acta Biomater.* **58**, 168–180 (2017).

184. Appel, E. a., del Barrio, J., Loh, X. J. & Scherman, O. a. Supramolecular polymeric hydrogels. *Chem. Soc. Rev.* **41**, 6195 (2012).

185. Lutolf, M. P. Spotlight on hydrogels. *Nat. Publ. Gr.* **8**, 451–453 (2009).

186. Jin, Y., Yu, C., Denman, R. J. & Zhang, W. Recent advances in dynamic covalent chemistry. *Chem. Soc. Rev.* **42**, 6634–6654 (2013).

187. Boehnke, N., Cam, C., Bat, E., Segura, T. & Maynard, H. D. Imine hydrogels with tunable degradability for tissue engineering. *Biomacromolecules* **16**, 2101–2108 (2015).

188. McKinnon, D. D., Domaille, D. W., Cha, J. N. & Anseth, K. S. Biophysically defined and cytocompatible covalently adaptable networks as viscoelastic 3d cell culture systems. *Adv. Mater.* **26**, 865–872 (2014).

189. Hozumi, T., Kageyama, T., Ohta, S., Fukuda, J. & Ito, T. Injectable Hydrogel with Slow Degradability Composed of Gelatin and Hyaluronic Acid Cross-Linked by Schiff's Base Formation. *Biomacromolecules* **19**, 288–297 (2018).

190. Shi, L. *et al.* Dynamic Coordination Chemistry Enables Free Directional Printing of Biopolymer Hydrogel. *Chem. Mater.* **29**, 5816–5823 (2017).

191. Wang, L. L. *et al.* Three-dimensional extrusion bioprinting of single- and double-network hydrogels containing dynamic covalent crosslinks. *J. Biomed. Mater. Res. - Part A* **106**, 865–875 (2018).

192. Dong, R., Pang, Y., Su, Y. & Zhu, X. Supramolecular hydrogels: synthesis, properties and their biomedical applications. *Biomater. Sci.* **3**, 937–954 (2015).
193. Webber, M. J., Appel, E. A., Meijer, E. W. & Langer, R. Supramolecular biomaterials. *Nat. Publ. Gr.* **15**, (2016).

194. Seiffert, S. & Sprakel, J. Physical chemistry of supramolecular polymer networks. *Chem. Soc. Rev.* **41**, 909–930 (2012).

195. Sijbesma, R. P., Beijer, F. H., Brunsveld, L., Folmer, B. J. B. & Hirschberg, J. H. K. K. Reversible Polymers Formed from Self-Complementary Monomers Using Quadruple Hydrogen Bonding. **278**, (1997).

196. Lehn, J. -M. Supramolecular Chemistry—Scope and Perspectives Molecules, Supermolecules, and Molecular Devices (Nobel Lecture). *Angew. Chemie Int. Ed. English* **27**, 89–112 (1988).

197. Aida, T., Meijer, E. W. & Stupp, S. I. Functional supramolecular polymers. *Science (80-.).* **335**, 813–817 (2012).

198. Dong, R. *et al.* Functional supramolecular polymers for biomedical applications. *Adv. Mater.* **27**, 498–526 (2015).

199. Hou, S., Wang, X., Park, S., Jin, X. & Ma, P. X. Rapid Self-Integrating, Injectable Hydrogel for Tissue Complex Regeneration. *Adv. Healthc. Mater.* **4**, 1491–1495 (2015).

200. Langer, R. & Tirrell, D. A. Designing materials for biology and medicine. *Nature*

428, 487–492 (2004).

201. Caliari, S. R. & Burdick, J. A. A practical guide to hydrogels for cell culture. *Nat. Methods* **13**, 405–414 (2016).

202. Chan, G. & Mooney, D. J. New materials for tissue engineering : towards greater control over the biological response. (2008). doi:10.1016/j.tibtech.2008.03.011

203. Hoffman, B. D., Grashoff, C. & Schwartz, M. A. Dynamic molecular processes mediate cellular mechanotransduction. (2011). doi:10.1038/nature10316

204. Engler, A. J., Sen, S., Sweeney, H. L. & Discher, D. E. Matrix Elasticity Directs Stem Cell Lineage Specification. *Cell* **126**, 677–689 (2006).

205. Ma, P. X. Biomimetic materials for tissue engineering. *Adv. Drug Deliv. Rev.* **60**, 184–198 (2008).

206. Ma, P. X. Scaffolds for tissue fabrication. *Mater. Today* **7**, 30–40 (2004).

207. Lutolf, M. P. *et al.* Synthetic matrix metalloproteinase-sensitive hydrogels for the conduction of tissue regeneration: Engineering cell-invasion characteristics. *Proc. Natl. Acad. Sci.* **100**, 5413–5418 (2003).

208. Zisch, A. H., Lutolf, M. P. & Hubbell, J. A. Biopolymeric delivery matrices for angiogenic growth factors. *Cardiovasc. Pathol.* **12**, 295–310 (2003).

209. Chung, C., Beecham, M., Mauck, R. L. & Burdick, J. A. The influence of degradation characteristics of hyaluronic acid hydrogels on in vitro neocartilage formation by mesenchymal stem cells. *Biomaterials* **30**, 4287–4296 (2009).

210. Phadke, A. *et al.* Rapid self-healing hydrogels. *Proc. Natl. Acad. Sci.* **109**, 4383–4388 (2012).

211. Dong, R., Zhao, X., Guo, B. & Ma, P. X. Self-Healing Conductive Injectable Hydrogels with Antibacterial Activity as Cell Delivery Carrier for Cardiac Cell Therapy. *ACS Appl. Mater. Interfaces* **8**, 17138–17150 (2016).

212. White, S. R. *et al.* Self-healing polymers and composites. *Am. Sci.* **99**, 392–399 (2011).

213. Hou, S. & Ma, P. X. Stimuli-Responsive Supramolecular Hydrogels with High Extensibility and Fast Self-Healing via Precoordinated Mussel-Inspired Chemistry. *Chem. Mater.* **27**, 7627–7635 (2015).

214. Burdick, J. A. & Anseth, K. S. Photoencapsulation of osteoblasts in injectable RGD-modified PEG hydrogels for bone tissue engineering. **23**, 4315–4323 (2002).

215. Wang, Y., Adokoh, C. K. & Narain, R. Recent development and biomedical applications of self-healing hydrogels. *Expert Opin. Drug Deliv.* **15**, 77–91 (2018).

216. Roh, Y. H., Ruiz, R. C. H., Peng, S., Lee, J. B. & Luo, D. Engineering DNA-based functional materials. *Chem. Soc. Rev.* **40**, 5730–5744 (2011).

217. Hirschberg, J. H. K. K. *et al.* Helical self-assembled polymers from cooperative stacking of hydrogen-bonded pairs. *Nature* **407**, 167–170 (2000).

218. Keten, S., Xu, Z., Ihle, B. & Buehler, M. J. Nanoconfinement controls stiffness, strength and mechanical toughness of Β-sheet crystals in silk. *Nat. Mater.* **9**, 359–367 (2010).

219. Dobb, M. G., Johnson, D. J. & Saville, B. P. Supramolecular Structure of a High-Modulus Polyaromatic Fiber (Kevlar 49). *J Polym Sci Polym Phys Ed* **15**, 2201–2211 (1977).

220. Beijer, F. H., Kooijman, H., Spek, A. L., Sijbesma, R. P. & Meijer, E. W. Self-Complementarity Achieved through Quadruple Hydrogen Bonding. *Angew. Chemie Int. Ed.* **37**, 75–78 (1998).

221. Beijer, F. H., Sijbesma, R. P., Kooijman, H., Spek, A. L. & Meijer, E. W. Strong dimerization of ureidopyrimidones via quadruple hydrogen bonding. *J. Am. Chem. Soc.* **120**, 6761–6769 (1998).

222. Goor, O. J. G. M., Hendrikse, S. I. S., Dankers, P. Y. W. & Meijer, E. W. From supramolecular polymers to multi-component biomaterials. *Chem. Soc. Rev.* **46**, 6621–6637 (2017).

223. Muylaert, D. E. P. *et al.* Early in-situ cellularization of a supramolecular vascular graft is modified by synthetic stromal cell-derived factor-1α derived peptides. *Biomaterials* **76**, 187–195 (2016).

224. Wong, C. T. S. *et al.* hydrogels for cell encapsulation. **106**, 22067–22072 (2009).

225. Dankers, P. Y. W. *et al.* Hierarchical formation of supramolecular transient networks in water: A modular injectable delivery system. *Adv. Mater.* **24**, 2703–2709 (2012).

226. Lange, R. F. M., van Gurp, M. & Meijer, E. W. Hydrogen-bonded supramolecular polymer networks. *J. Polym. Sci. Part A-Polymer Chem.* **37**, 3657–3670 (1999).

227. Ligthart, G. B. W. L., Ohkawa, H., Sijbesma, R. P. & Meijer, E. W. Complementary quadruple hydrogen bonding in supramolecular copolymers. *J. Am. Chem. Soc.* **127**, 810–811 (2005).

228. Dankers, P. Y. W. *et al.* Convenient formulation and application of a supramolecular

ureido-pyrimidinone modified poly(ethylene glycol) carrier for intrarenal growth factor delivery. *Eur. Polym. J.* **72**, 484–493 (2015).

229. Bastings, M. M. C. *et al.* A fast pH-switchable and self-healing supramolecular hydrogel carrier for guided, local catheter injection in the infarcted myocardium. *Adv. Healthc. Mater.* **3**, 70–78 (2014).

230. Koudstaal, S. *et al.* Sustained delivery of insulin-like growth factor-1/hepatocyte growth factor stimulates endogenous cardiac repair in the chronic infarcted pig heart. *J. Cardiovasc. Transl. Res.* **7**, 232–241 (2014).

231. Chirila, T. V. *et al.* Hydrogen-bonded supramolecular polymers as self-healing hydrogels: Effect of a bulky adamantyl substituent in the ureido-pyrimidinone monomer. *J. Appl. Polym. Sci.* **131**, 1–12 (2014).

232. Bakker, M. H. & Dankers, P. Y. W. *Supramolecular biomaterials based on ureidopyrimidinone and benzene-1,3,5-tricarboxamide moieties*. *Self-Assembling Biomaterials* (Elsevier Ltd., 2018). doi:10.1016/B978-0-08-102015-9.00009-5
233. Leenders, C. M. A. *et al.* From supramolecular polymers to hydrogel materials. *Mater. Horizons* **1**, 116–120 (2014).

234. Leenders, C. M. A. *et al.* Supramolecular polymerization in water harnessing both hydrophobic effects and hydrogen bond formation. *Chem. Commun.* **49**, 1963–1965 (2013).

235. Stals, P. J. M., Haveman, J. F., Palmans, A. R. A. & Schenning, A. P. H. J. The Self-Assembly Properties of a Benzene-1,3,5-tricarboxamide Derivative. *J. Chem. Educ.* **86**, 230 (2009).

236. Lou, X. *et al.* Dynamic diversity of synthetic supramolecular polymers in water as revealed by hydrogen/deuterium exchange. *Nat. Commun.* **8**, 1–8 (2017).

237. Wijnands, S. P. W., Engelen, W., Lafleur, R. P. M., Meijer, E. W. & Merkx, M. Controlling protein activity by dynamic recruitment on a supramolecular polymer platform. *Nat. Commun.* **9**, (2018).

238. Albertazzi, L., Hofstad, R. W. Van Der & Meijer, E. W. Probing Exchange Pathways in Super-Resolution Microscopy. *Science* **491**, 10–15 (2014).

239. Baker, M. B. *et al.* Exposing Differences in Monomer Exchange Rates of Multicomponent Supramolecular Polymers in Water. *ChemBioChem* **17**, 207–213 (2016).

240. Bakker, M. H., Lee, C. C., Meijer, E. W., Dankers, P. Y. W. & Albertazzi, L. Multicomponent Supramolecular Polymers as a Modular Platform for Intracellular Delivery. *ACS Nano* **10**, 1845–1852 (2016).

241. Wei, Z. *et al.* Self-healing gels based on constitutional dynamic chemistry and their potential applications. *Chem. Soc. Rev.* **43**, 8114–8131 (2014).

242. Chang, G. *et al.* Self-healable hydrogel on tumor cell as drug delivery system for localized and effective therapy. *Carbohydr. Polym.* **122**, 336–342 (2015).

243. Ma, X. & Zhao, Y. Biomedical Applications of Supramolecular Systems Based on Host-Guest Interactions. *Chem. Rev.* **115**, 7794–7839 (2015).

244. Zhang, J. & Ma, P. X. Cyclodextrin-based supramolecular systems for drug delivery: Recent progress and future perspective. *Adv. Drug Deliv. Rev.* **65**, 1215–1233 (2013).

245. Davis, M. E. & Brewster, M. E. Cyclodextrin-based pharmaceutics: Past, present and future. *Nat. Rev. Drug Discov.* **3**, 1023–1035 (2004).

246. Villiers, A. *Sur la fermentation de la fécule par l'action du ferment butyrique*. *Comptes rendus de l'Académie des Sciences* (1891). doi:10.1016/S0360-0564(08)60302-8

247. Schardinger, F. Uber thermophile Bakterien aus verschiedenen Speisen und Milch. *Zeitschrift fur Untersuchung der Nahrungs- und Genusm.* **6**, 865–880 (1903).

248. Challa, R., Ahuja, A., Ali, J. & Khar, R. K. Cyclodextrins in drug delivery: An updated review. *AAPS PharmSciTech* **6**, E329–E357 (2005).

249. Yuen, F. & Tam, K. C. Cyclodextrin-assisted assembly of stimuli-responsive polymers in aqueous media. *Soft Matter* **6**, 4613–4630 (2010).

250. Deng, W., Yamaguchi, H., Takashima, Y. & Harada, A. A chemical-responsive supramolecular hydrogel from modified cyclodextrins. *Angew. Chemie - Int. Ed.* **46**, 5144–5147 (2007).

251. Rodell, C. B., Dusaj, N. N., Highley, C. B. & Burdick, J. A. Injectable and Cytocompatible Tough Double-Network Hydrogels through Tandem Supramolecular and Covalent Crosslinking. *Adv. Mater.* 8419–8424 (2016). doi:10.1002/adma.201602268

252. Li, J., Harada, A. & Kamachi, M. Sol–Gel Transition during Inclusion Complex Formation between α-Cyclodextrin and High Molecular Weight Poly(ethylene glycol)s in Aqueous Solution. *Polymer Journal* **26**, 1019–1026 (1994).

253. Wenz, G. & Keller, B. Threading Cyclodextrin Rings on Polymer Chains. *Angew. Chemie Int. Ed. English* **31**, 197–199 (1992).

254. Miyauchi, M., Kawaguchi, Y. & Harada, A. Formation of Supramolecular Polymers

Constructed by Cyclodextrins with Cinnamamide. *J. Incl. Phenom.* **50**, 57–62 (2004).

255. Li, J. Self-assembled supramolecular hydrogels based on polymer-cyclodextrin inclusion complexes for drug delivery. *NPG Asia Mater.* **2**, 112–118 (2010).

256. Kakuta, T. *et al.* Preorganized hydrogel: Self-healing properties of supramolecular hydrogels formed by polymerization of host-guest-monomers that contain cyclodextrins and hydrophobic guest groups. *Adv. Mater.* **25**, 2849–2853 (2013).

257. Kandow, C. E., Georges, P. C., Janmey, P. A. & Beningo, K. A. Polyacrylamide Hydrogels for Cell Mechanics: Steps Toward Optimization and Alternative Uses. *Methods Cell Biol.* **83**, 29–46 (2007).

258. Wang, Z. *et al.* A Novel Rapidly Self-healing Host-guest Supramolecular Hydrogel with High Mechanical Strength and Excellent Biocompatibility. *Angew. Chemie Int. Ed.* 1–6 (2018). doi:10.1002/anie.201804400

259. Highley, C. B., Rodell, C. B. & Burdick, J. A. Direct 3D Printing of Shear-Thinning Hydrogels into Self-Healing Hydrogels. *Adv. Mater.* **27**, 5075–5079 (2015).

260. Song, X. & Li, J. *Functional Hydrogels as Biomaterials*. (Springer-Verlag GmbH Germany, 2018). doi:10.1007/978-3-662-57511-6

261. Khodaverdi, E. *et al.* Self-assembled supramolecular hydrogel based on PCL-PEG-PCL triblock copolymer and γ-cyclodextrin inclusion complex for sustained delivery of dexamethasone. *Int. J. Pharm. Investig.* **6**, 78 (2016).

262. Miyamae, K., Nakahata, M., Takashima, Y. & Harada, A. Self-Healing, Expansion-Contraction, and Shape-Memory Properties of a Preorganized Supramolecular Hydrogel through Host-Guest Interactions. *Angew. Chemie - Int. Ed.* **54**, 8984–8987 (2015).

263. Zheng, Z. *et al.* Dynamic Softening or Stiffening a Supramolecular Hydrogel by Ultraviolet or Near-Infrared Light. *ACS Appl. Mater. Interfaces* **9**, 24511–24517 (2017).

264. Rodell, C. B. *et al.* Shear-Thinning Supramolecular Hydrogels with Secondary Autonomous Covalent Crosslinking to Modulate Viscoelastic Properties In Vivo. 636–644 (2015). doi:10.1002/adfm.201403550

265. Song, X. *et al.* Thermoresponsive Delivery of Paclitaxel by β-Cyclodextrin-Based Poly(N-isopropylacrylamide) Star Polymer via Inclusion Complexation. *Biomacromolecules* **17**, 3957–3963 (2016).

266. Mealy, J. E., Rodell, C. B. & Burdick, J. A. Sustained small molecule delivery from

injectable hyaluronic acid hydrogels through host-guest mediated retention. *J. Mater. Chem. B* **3**, 8010–8019 (2015).

267. Peng, K., Tomatsu, I. & Kros, A. Light controlled protein release from a supramolecular hydrogel. *Chem. Commun.* **46**, 4094–4096 (2010).

268. Harada, A., Takashima, Y. & Nakahata, M. Supramolecular polymeric materials via cyclodextrin-guest interactions. *Acc. Chem. Res.* **47**, 2128–2140 (2014).

269. Nakahata, M., Takashima, Y., Yamaguchi, H. & Harada, A. Redox-responsive self-healing materials formed from host-guest polymers. *Nat. Commun.* **2**, 511–516 (2011).

270. Peng, L. *et al.* Electrochemical redox responsive supramolecular self-healing hydrogels based on host-guest interaction. *Polym. Chem.* **6**, 3652–3659 (2015).

271. Chen, H., Ma, X., Wu, S. & Tian, H. A Rapidly Self-Healing Supramolecular Polymer Hydrogel with Photostimulated Room-Temperature Phosphorescence Responsiveness. *Angew. Chemie* **126**, 14373–14376 (2014).

272. Dong, R., Liu, Y., Zhou, Y., Yan, D. & Zhu, X. Photo-reversible supramolecular hyperbranched polymer based on host-guest interactions. *Polym. Chem.* **2**, 2771–2774 (2011).

273. Yagai, S. & Kitamura, A. Recent advances in photoresponsive supramolecular self-assemblies. *Chem. Soc. Rev.* **37**, 1520–1529 (2008).

274. Whitesides, G. M. & Grzybowski, B. Self-assembly at all scales. *Science* **295**, 2418–21 (2002).

275. Lupas, A. [30] Prediction and analysis of coiled-coil structures. *Methods Enzymol.* **266**, 513–525 (1996).

276. Smith, G. F. *Medicinal chemistry by the numbers: the physicochemistry, thermodynamics and kinetics of modern drug design. Progress in medicinal chemistry* **48**, (Elsevier Masson SAS, 2009).

277. Mihajlovic, M. *et al.* Tough Supramolecular Hydrogel Based on Strong Hydrophobic Interactions in a Multiblock Segmented Copolymer. *Macromolecules* **50**, 3333–3346 (2017).

278. Tuncaboylu, D. C., Sari, M., Oppermann, W. & Okay, O. Tough and self-healing hydrogels formed via hydrophobic interactions. *Macromolecules* **44**, 4997–5005 (2011).

279. Petka, W. A., Harden, J. L., McGrath, K. P., Wirtz, D. & Tirrell, D. A. Reversible

hydrogels from self-assembling artificial proteins. *Science (80-.).* **281**, 389–392 (1998).

280. Fichman, G. & Gazit, E. Self-assembly of short peptides to form hydrogels: Design of building blocks, physical properties and technological applications. *Acta Biomater.* **10**, 1671–1682 (2014).

281. Galler, K. M. *et al.* Self-Assembling Peptide Amphiphile Nanofibers as a Scaffold for Dental Stem Cells. *Tissue Eng. Part A* **14**, 2051–2058 (2008).

282. Huang, J. *et al.* Impact of order and disorder in RGD nanopatterns on cell adhesion. *Nano Lett.* **9**, 1111–1116 (2009).

283. Nowak, A. P. *et al.* Rapidly recovering hydrogel scaffolds from self-assembling diblock copolypeptide amphiphiles. *Nature* **417**, 424–428 (2002).

284. Jacob, R. S. *et al.* Self healing hydrogels composed of amyloid nano fibrils for cell culture and stem cell differentiation. *Biomaterials* **54**, 97–105 (2015).

285. Ustun Yaylaci, S. *et al.* Supramolecular GAG-like Self-Assembled Glycopeptide Nanofibers Induce Chondrogenesis and Cartilage Regeneration. *Biomacromolecules* **17**, 679–689 (2016).

286. Zhang, P., Cheetham, A. G., Lin, Y. A. & Cui, H. Self-assembled tat nanofibers as effective drug carrier and transporter. *ACS Nano* **7**, 5965–5977 (2013).

287. Ikeda, M. *et al.* Installing logic-gate responses to a variety of biological substances in supramolecular hydrogel-enzyme hybrids. *Nat. Chem.* **6**, 511–518 (2014).

288. Lee, S. S. *et al.* Gel Scaffolds of BMP-2-Binding Peptide Amphiphile Nanofibers for Spinal Arthrodesis. *Adv. Healthc. Mater.* **4**, 131–141 (2015).

289. Fernández-Colino, A., Arias, F. J., Alonso, M. & Carlos Rodríguez-Cabello, J. Self-organized ECM-mimetic model based on an amphiphilic multiblock silk-elastin-like corecombinamer with a concomitant dual physical gelation process. *Biomacromolecules* **15**, 3781–3793 (2014).

290. Galler, K. M., Hartgerink, J. D., Cavender, A. C., Schmalz, G. & D’Souza, R. N. A Customized Self-Assembling Peptide Hydrogel for Dental Pulp Tissue Engineering. *Tissue Eng. Part A* **18**, 176–184 (2012).

291. Galler, K. M., Aulisa, L., Regan, K. R., D’Souza, R. N. & Hartgerink, J. D. Self-assembling multidomain peptide hydrogels: Designed susceptibility to enzymatic cleavage allows enhanced cell migration and spreading. *J. Am. Chem. Soc.* **132**, 3217–3223 (2010).

292. Black, K. A. *et al.* Biocompatibility and Characterization of a Peptide Amphiphile Hydrogel for Applications in Peripheral Nerve Regeneration. *Tissue Eng. Part A* **21**, 1333–1342 (2015).

293. Sepantafar, M. *et al.* Stem cells and injectable hydrogels: Synergistic therapeutics in myocardial repair. *Biotechnol. Adv.* **34**, 362–379 (2015).

294. Hendriks, J., Riesle, J. & Blitterswijk, C. A. van. Capturing the stem cell paracrine effect using heparin-presenting nanofibres to treat cardiovascular diseases. *J. Tissue Eng. Regen. Med.* **4**, 524–531 (2010).

295. Padin-Iruegas, M. E. *et al.* Cardiac Progenitor Cells and Biotinylated IGF-1 Nanofibers Improve Endogenous and Exogenous Myocardial Regeneration after Infarction. **120**, 876–887 (2010).

296. Kisiday, J. *et al.* Self-assembling peptide hydrogel fosters chondrocyte extracellular matrix production and cell division: Implications for cartilage tissue repair. *Proc. Natl. Acad. Sci.* **99**, 9996–10001 (2002).

297. Deming, T. J. Polypeptide hydrogels via a unique assembly mechanism. *Soft Matter* **1**, 28–35 (2005).

298. Li, J. *et al.* Self-assembled supramolecular hydrogels formed by biodegradable PEO-PHB-PEO triblock copolymers and α-cyclodextrin for controlled drug delivery. *Biomaterials* **27**, 4132–4140 (2006).

299. Jeong, B., Bae, Y. H., Lee, D. S. & Kim, S. W. Biodegradable block copolymers as injectable drug-delivery systems. *Nature* **388**, 860–862 (1997).

300. Zhang, J. *et al.* Physically associated synthetic hydrogels with long-term covalent stabilization for cell culture and stem cell transplantation. *Adv. Mater.* **23**, 5098–5103 (2011).

301. Murphy, R. *et al.* Degradable 3D-Printed Hydrogels Based on Star-Shaped Copolypeptides. *Biomacromolecules* **19**, 2691–2699 (2018).

302. Zhu, S. *et al.* Accelerated wound healing by injectable star poly(ethylene glycol)-b-poly(propylene sulfide) scaffolds loaded with poorly water-soluble drugs. *J. Control. Release* **282**, 156–165 (2018).

303. Kuo, C. K. & Ma, P. X. Ionically crosslinked alginate hydrogels as scaffolds for tissue engineering: Part 1. Structure, gelation rate and mechanical properties. *Biomaterials* **22**, 511–521 (2001).

304. Park, H., Kang, S. W., Kim, B. S., Mooney, D. J. & Lee, K. Y. Shear-reversibly crosslinked alginate hydrogels for tissue engineering. *Macromol. Biosci.* **9**, 895–

901 (2009).

305. Hori, Y., Winans, A. M., Huang, C. C., Horrigan, E. M. & Irvine, D. J. Injectable dendritic cell-carrying alginate gels for immunization and immunotherapy. *Biomaterials* **29**, 3671–3682 (2008).

306. Zhao, L., Weir, M. D. & Xu, H. H. K. An injectable calcium phosphate-alginate hydrogel-umbilical cord mesenchymal stem cell paste for bone tissue engineering. *Biomaterials* **31**, 6502–6510 (2010).

307. Kuo, C. K. & Ma, P. X. Maintaining dimensions and mechanical properties of ionically crosslinked alginate hydrogel scaffolds in vitro. *J. Biomed. Mater. Res. - Part A* **84**, 899–907 (2008).

308. Ren, Z., Zhang, Y., Li, Y., Xu, B. & Liu, W. Hydrogen bonded and ionically crosslinked high strength hydrogels exhibiting Ca^{2+}-triggered shape memory properties and volume shrinkage for cell detachment. *J. Mater. Chem. B* **3**, 6347–6354 (2015).

309. Sun, J. Y. *et al.* Highly stretchable and tough hydrogels. *Nature* **489**, 133–136 (2012).

310. Park, H., Woo, E. K. & Lee, K. Y. Ionically cross-linkable hyaluronate-based hydrogels for injectable cell delivery. *J. Control. Release* **196**, 146–153 (2014).

311. Han, Y. L. *et al.* Directed self-assembly of microscale hydrogels by electrostatic interaction. *Biofabrication* **5**, (2013).

312. Wang, Q. *et al.* High-water-content mouldable hydrogels by mixing clay and a dendritic molecular binder. *Nature* **463**, 339–343 (2010).

313. Haas, K. L. & Franz, K. J. Application of Metal Coordination Chemistry To Explore and Manipulate Cell Biology. *Chem. Rev.* **109**, 4921–4960 (2009).

314. Atwood, J. L. & Steed, J. W. Supramolecular Chemistry. (2000).

315. Fullenkamp, D. E., He, L., Barrett, D. G., Burghardt, W. R. & Messersmith, P. B. Mussel-inspired histidine-based transient network metal coordination hydrogels. *Macromolecules* **46**, 1167–1174 (2013).

316. Varghese, S., Lele, A. & Mashelkar, R. Metal-ion-mediated healing of gels. *J. Polym. Sci. Part A Polym. Chem.* **44**, 666–670 (2006).

317. Hogg, R. & Wilkins, R. G. Exchange Studies of Certain Chelate Compounds of the Transition Metals. Part VIII. 2,2',2''-Terpyridine Complexes. in *International Conference on Co-ordination Chemistry, Detroit* (1962).

318. Holten-Andersen, N. *et al.* pH-induced metal-ligand cross-links inspired by mussel yield self-healing polymer networks with near-covalent elastic moduli. *Proc. Natl. Acad. Sci.* **108**, 2651–2655 (2011).

319. Wang, C., Stewart, R. J. & Kopeček, J. Hybrid hydrogels assembled from synthetic polymers and coiled-coil protein domains. *Nature* **397**, 417–420 (1999).

320. Tang, Q. *et al.* Polyhistidine-Based Metal Coordination Hydrogels with Physiologically Relevant pH Responsiveness and Enhanced Stability through a Novel Synthesis. *Macromol. Rapid Commun.* **39**, 1800109 (2018).

321. Hofmeier, H., Hoogenboom, R., Wouters, M. E. L. & Schubert, U. S. High molecular weight supramolecular polymers containing both terpyridine metal complexes and ureidopyrimidinone quadruple hydrogen-bonding units in the main chain. *J. Am. Chem. Soc.* **127**, 2913–2921 (2005).

322. Shi, Y. *et al.* A Conductive Self-Healing Hybrid Gel Enabled by Metal-Ligand Supramolecule and Nanostructured Conductive Polymer. *Nano Lett.* **15**, 6276–6281 (2015).